# ANALYSIS OF SIX-PHASE INDUCTION MACHINE FOR RENEWABLE AND SUSTAINABLE ENERGY APPLICATIONS

**Ph. D. Thesis**

*by*

**CHINMAYA. K. A**


**DEPARTMENT OF ELECTRICAL ENGINEERING**
**INDIAN INSTITUTE OF TECHNOLOGY ROORKEE**
**ROORKEE – 247667 (INDIA)**
**AUGUST, 2019**

# ANALYSIS OF SIX-PHASE INDUCTION MACHINE FOR RENEWABLE AND SUSTAINABLE ENERGY APPLICATIONS

**A THESIS**

***Submitted in partial fulfilment of the requirements for the award of the degree***

*of*

**DOCTOR OF PHILOSOPHY**

*in*

**ELECTRICAL ENGINEERING**

*by*

**CHINMAYA. K. A**


**DEPARTMENT OF ELECTRICAL ENGINEERING**
**INDIAN INSTITUTE OF TECHNOLOGY ROORKEE**
**ROORKEE – 247667 (INDIA)**
**AUGUST, 2019**

# INDIAN INSTITUTE OF TECHNOLOGY ROORKEE

## CANDIDATE'S DECLARATION

I hereby certify that the work which is being presented in the thesis entitled "**ANALYSIS OF SIX-PHASE INDUCTION MACHINE FOR RENEWABLE AND SUSTAINABLE ENERGY APPLICATIONS"** in partial fulfilment of the requirements for the award of the Degree of Doctor of Philosophy and submitted in the Department of Electrical Engineering of the Indian Institute of Technology Roorkee, Roorkee, is an authentic record of my own work carried out during a period from December, 2014 to March, 2019 under the supervision of Dr. G. K. Singh, Professor, Department of Electrical Engineering, Indian Institute of Technology Roorkee, Roorkee.

The matter presented in this thesis has not been submitted by me for the award of any other degree of this or any other Institution.

**(CHINMAYA. K. A)**

This is to certify that the above statement made by the candidate is correct to the best of my knowledge.

**(G. K. Singh)**
**Supervisor**

The Ph. D. Viva-Voce Examination of **CHINMAYA. K. A,** Research Scholar, has been held on August 5th 2019.

**Chairperson, SRC** **External Examiner**

This is to certify that the student has made all the corrections in the thesis.

**Supervisor** **Head of the Department**
**Dated: August 5, 2019**

# ABSTRACT

The main focus of this research work lies in developing a reliable and efficient multiphase drive for variable speed wind energy conversion system (WECS) and power electronic interface (PEI) for plug-in electric vehicles (PEVs). Multiphase machine considered in this work consists of two three-phase sets spatially phase shifted by thirty electrical degrees, i.e., a six-phase machine. As the angular difference between two consecutive phases is not symmetrical, this machine is referred as asymmetrical six-phase induction machine (ASIM). When compared to a symmetrical six-phase machine, this asymmetrical configuration eliminates the sixth harmonic torque pulsation when supplied from a voltage source converter. The neutrals of both three-phase sets are kept isolated to avoid physical fault propagation between the two winding sets.

In first part of the thesis, a detailed mathematical modeling of ASIM and six-phase voltage source converter is developed for simulation purposes. In the later part, three different existing space vector pulse width modulation (SVPWM) techniques are analyzed for ASIM supplied from two three-phase voltage source converters (VSCs). A modified SVPWM method is also proposed for the ASIM drive. Harmonic components in the phase currents and phase voltages are analyzed for all the four different SVPWM schemes.

A simple indirect rotor field oriented control (IRFOC) methodology for the ASIM is developed, and the satisfactory SVPWM emerged from the previous analysis is utilized. The main objective of this control is to eliminate the unbalanced currents between two three-phase sets and asymmetries associated with switching harmonics. Proposed IRFOC also consists of an additional loop for the resilient speed control under input load disturbances without any additional PI controllers.

Thereupon the ASIM drive with indirect rotor field oriented control is operated as grid-connected variable speed generator for wind energy conversion systems. Back to back connected voltage source converters (VSCs) are utilized for interfacing asymmetrical six-phase induction generator (ASIG) with the grid. Machine side consists of two parallel converters for IRFOC. Maximum power is extracted at different wind speeds by operating the generator at a certain optimum speed. IRFOC operates the machine at this optimum speed and maximum power point tracking (MPPT) with power speed curve of the wind turbine is utilized to

estimate the optimum speed. At grid side, a three-level converter is controlled grid vector-oriented control (GVOC) for maintaining DC link voltage, and to regulate the flow of reactive power between grid and generator. A comparative analysis of ASIG with conventional three-phase induction generator in the same machine frame is performed.

Detailed performance analysis of ASIG in conjunction with other types of wind energy conversion systems is performed. It targets to emphasize the advantages of considering the ASIG in stand-alone and grid-connected fixed speed mode. Various aspects such as efficiency, reliability, and productivity are considered while performing the analysis. In stand-alone mode, reliability and efficiency of self-excited ASIG are ascertained by disconnecting one of the two three-phase sets connected to a resistive load. In grid-connected fixed speed mode, two different scenarios are implemented to pursue the applicability of ASIG. In the first scenario, only one three-phase winding set is connected to the grid and another set is connected to a local resistive load. In the second scenario, both three-phase windings are connected to the grid via $\Delta/Y - Y$ three-winding transformer.

Lastly, a power electronic interface is developed for plug-in electric vehicles. It consists of ASIM drive with IRFOC as propulsion drive and a CuK converter based integrated on-board battery charger. The proposed bidirectional DC/DC converter is capable of performing the buck/boost function during all modes of operation. It operates as a power factor correction (PFC) converter during plug-in charging mode, and a single switch inverting buck/boost converter in propulsion and regenerative braking modes. Selection of a wide range of battery voltages and adequate control over regenerative braking can be achieved with the proposed multi-functional converter. In addition, size, weight and cost of the charger are also reduced, as it involves the minimum number of components compared to existing buck/boost converters used in chargers. By utilizing a six-phase induction machine drive in propulsion system, efficiency and power density of PEI is improved. This drive even allows for further modifications to the proposed topology.

Space vector PWM techniques, indirect rotor field oriented control and two different applications of ASIM drive are verified through simulation and experiments undertaken using laboratory prototype. The waveforms obtained from the simulation and experiment are presented in this thesis.

# ACKNOWLEDGMENTS

It is my desire and a great pleasure to offer my sincere thanks to all those who have contributed, in whatever way, to the completion of my work.

First, I take this opportunity to express my sincere gratitude to toward my supervisor Dr. G. K Singh, Professor, Department of Electrical Engineering, Indian Institute of Technology Roorkee, Roorkee, India for his constant support, guidance, encouragement and motivation throughout the duration of this research work.

I am also thankful to my research committee members, Prof. S. P. Singh, Dr. Vinay Pant and Prof. R P Saini, for their constructive suggestions during several meetings held for this research work. I would also like to thank the Head of the Department and other faculty members of Electrical Engineering Department, IITR for their moral support and providing the excellent laboratory facilities during this research work at Indian Institute of Technology Roorkee, Roorkee. I would thank the Ministry of Human Resources Development (MHRD), Government of India for providing the fellowship for carrying out this research work. I wish also to mention the memorable conversation I have with Prof M. K. Vasantha, Prof. M. K. Pathak and Dr. Anubrata Dey. I also thank the technical and office staff of the department, especially Mr. Mohan Singh, Mr. Rishabh Verma, Mr. Bhopal Rawat, Mr. Amir Ahmad, Mr. Rajkumar and Mr.Sanjay for their cooperation and help in official work related to this research. Also, retired superintendent in PG Laboratory, Mr. Shaadiram deserve my highest appreciation.

I extend my sincere acknowledgement to Dr. S. N. Singh, Retired Scientist Alternate Hydro Energy Center, Indian Institute of Technology Roorkee for providing the Six-phase machine to perform my experimental work. I would like to thank the anonymous reviewers of my research work, who gave me the suggestions to improve the quality of the research work and the direction for the additional work.

My journey in IIT Roorkee is blessed with many friends who played a major role in maintaining a constantly high level of motivation, and thus in the progress of my work. I would give special acknowledgement to my fellow researchers, Dr. Ankit Kumar Singh, Dr. Zameer Ahmad, Dr. Arif Iqbal, Mr. Jose Thankanchan, Mr. B. Krishna Chaitanya, Mr. Gururaj M V, Mr. Saran Satasangi, Mr. Gaurav, Mr. Narendra Babu and many more.

I would also like to acknowledge my friend Mr. Rohit Chandan for his inputs during the course of my PhD work.

I wish to express my hearty gratitude to my parents, friends back home and all my family members, for their endless moral support and encouragement. Finally, I am very thankful to all-merciful God who gave me blessing and wisdom to carry out this PhD research work.

(Chinmaya K A)

# CONTENTS

# LIST OF FIGURES

# LIST OF TABLES

# LIST OF ACRONYMS

| | |
|---|---|
| **WECS** | Wind Energy Conversion System |
| **PEI** | Power Electronic Interface |
| **PEVs** | Plug-in Electric Vehicles |
| **ASIM** | Asymmetrical Six-phase Induction Machine |
| **VSC** | Voltage Source Converter |
| **PWM** | Pulse Width Modulation |
| **SPWM** | Sinusoidal Pulse Width Modulation |
| **SVPWM** | Space Vector Pulse Width Modulation |
| **IRFOC** | Indirect Rotor Field-Oriented Control |
| **VSC** | Voltage Source Converter |
| **ASIG** | Asymmetrical Six-phase Induction Generator |
| **MPPT** | Maximum Power Point Tracking |
| **GVOC** | Grid Vector-Oriented Control |
| **PFC** | Power Factor Correction |
| **EU** | European Union |
| **WRIG** | Wound Rotor Induction Generator |
| **SG** | Synchronous Generator |
| **ICE** | Internal Combustion Engine |
| **IM** | Induction Motor |
| **SCIM** | Squirrel Cage Induction Machine |
| **TPIG** | Three-Phase Induction Machine |
| **SCIG** | Squirrel Cage Induction Generator |
| **DFIG** | Doubly Fed Induction Generator |
| **PMSG** | Permanent Magnet Synchronous Generator |
| **DSPMG** | Doubly Salient Permanent-Magnet Generators |
| **DTC** | Direct Torque Control |
| **OBC** | Onboard Battery Charger |
| **UPF** | Unity Power Factor |

| | |
|---|---|
| **FEC** | Front End Converter |
| **VSD** | Vector Space Decomposition |
| **FPGA** | Field Programmable Gate Array |
| **EMI** | Electromagnetic Interference |
| **BSC** | Battery Side Converter |
| **DSC** | Drive Side Converter |
| **CCM** | Continuous Conduction Mode |

# LIST OF SYMBOLS

| | |
|---|---|
| $n$ | Number of phases |
| $v$ | Voltage |
| $v_g$ | Grid voltage |
| $v_b$ | Battery voltage |
| $i$ | Current |
| $\lambda$ | Flux linkage |
| **$\Delta$/Y-Y** | Delta/Star-Star |
| $r$ | Resistance |
| $L$ | Inductance |
| $f$ | Variables |
| $\omega_a$ | Rotational speed of the d-axis of the arbitrary common reference frame |
| $\omega_r$ | Rotational speed of the rotor flux space vector with respect to the stator |
| $\omega_e$ | Rotational speed of the d-axis of the synchronous reference frame |
| $\omega_b$ | Base speed |
| $\omega_{sl}$ | Slip speed |
| $L_{l1}$ | Leakage inductance per phase of stator winding set I |
| $L_{l2}$ | Leakage inductance per phase of stator winding set II |
| $L_{lm}$ | Common mutual leakage inductance between the two sets of stator windings |
| $L_m$ | Mutual inductance between stator and rotor |
| $L_{ldq}$ | Cross-saturation coupling between d- and q-axis of the stator |
| $\theta$ | Angle of rotational transformation for the stator |
| $\alpha$ | Angular displacement between two three-phase sets |
| $\delta$ | $\theta - \pi/6$ |
| $P$ | Number of poles |
| $T_{sh}$ | Shaft torque |
| $T_{em}$ | Electromagnetic torque |
| $J$ | Moment of inertia |

| | |
|---|---|
| $B$ | Friction co-efficient of machine |
| $p$ | Differential operator |
| $V_{DC}$ | DC-link voltage |
| $v_{A1}, v_{B1}, v_{C1}.....,$ | Inverter leg voltages |
| $v_{a1}, v_{b1}, v_{c1}.....,$ | Phase to neutral voltages |
| $S_{a1}, S_{b1}, S_{c1}.....,$ | Switching functions of DC-AC inverter |
| $S_1, S_2, S_3$ | Switching functions of DC-DC converter |
| $v^*$ | Reference space vector |
| $\|V_l\|$ | Length of largest vector |
| $T_s$ | Switching period |
| $T_{eff}$ | Effective time period |
| $T_{CM}$ | Common mode period |
| $T_1, T_2, T_3.....,$ | Time of application of active space vectors |
| $T_0$ | Time of application of zero space vectors |
| $m_a$ | Modulation index |
| $\tau_s$ | Stator time constant |
| $\tau_r$ | Rotor time constant |
| $M$ | Voltage conversion ratio |
| $d$ | Duty ratio |

**Subscripts**

| | |
|---|---|
| $s$ | Associated with stator |
| $s1$ | Associated with stator winding set I |
| $s2$ | Associated with stator winding set II |
| $r$ | Associated with rotor |
| $q1 - d1/1qd0$ | Related to stator winding set I after application of the decoupling and rotational transformation |
| $q2 - d2/2qd0$ | Related to stator winding set II after application of the decoupling and rotational transformation |

# CHAPTER 1

# INTRODUCTION

## 1.1 Background and Motivation

Development of modern civilization depends on the electrical energy generated and consumed. Over the past few years, growing responsibility in the research community towards developing a sustainable environment has led to a quest for clean and pure energy. Alternative energy sources such as solar, wind, tidal wave, geothermal etc., are attracting greater attention for fulfilling the societies power demand. More concern is directed towards the renewable and small scale power generation. The European Union (EU) is estimated to produce 14% of its energy consumption from renewable sources. EUs' renewable energy directive sets a goal of producing 27% of energy from renewable sources by 2030 [1].

Wind energy is the most aspiring source of renewable energy, because of its economic viability, matured technology and non-polluting nature. It can be combined with other sources to operate as a hybrid system [2]. Megawatts of electrical energy is already being extracted from the wind and small hydro turbines all over the world. Wind power generation has accomplished exponential progress in the last few years. EU has 131 GW onshore and 11 GW offshore wind power plants, and it is expected to thrive in the further coming years. When compared to onshore wind generating stations, offshore wind turbines are being preferred, because strong and consistent winds are found over oceans and mountain tops [3]. Availability of cheaper land even reduces the installation cost. However, reliability is an important challenge here, as regular maintenance is laborious.

Traditionally, synchronous machines have been utilized for power generation, but squirrel cage induction machines are gradually being used these days, since these are inexpensive with robust and sturdy construction compared to synchronous generator (SG), and it requires minimal maintenance compared to wound rotor induction generator (WRIG) [4]. Other than these traditional generators, a few novel types of generators, such as brushless DFIGs, multiphase generators, doubly salient permanent-magnet generators (DSPMG), the stator PM generators, and the superconducting generators, have been proposed by the researchers [5–7].

Even though the AC power grid consists of three-phase, multiphase induction generators are also considered for offshore and on-shore grid-connected power generating stations. The failure of one or two phases does not affect the generation drastically compared to that of three-phase induction generators.

A sustainable environment also requires sustainability in transportation. Transport systems have significant impacts on the environment, accounting for between 20% and 25% of world energy consumption and carbon dioxide emissions. This increased environmental concern has led to greater attention and interest towards the electrification of transportation sector. Automotive companies are still concentrating on developing reliable and efficient internal combustion engines (ICEs) for private transportation. On the other hand, Electrification of public transport has been successfully adapted in many developed and developing nations. Moreover, in recent years, even in private sectors; electric vehicles (EVs), plug-in electric vehicles (PEVs) and hybrid electric vehicles (HEVs) are being considered as future means of mainstream transportation [8, 9]. They are also a promising solution to curb air pollution as battery power is used to produce the clean energy for these vehicles [10].

Multiphase machines are usually used in high power /high current applications. Increased power density and reliability are the key points to consider multiphase induction machines for WECS and EVs. Higher degrees of freedom offered by the multiphase machine can be beneficial in controlling and maintenance perspective. The concept of multiphase is not new, multiphase drive system was first proposed in 1969 [11]. However, with the increased scope towards the applications of multiphase machines and drives, researchers' attention towards it increased consistently in the last two decades.

## 1.2 Literature Review

From the last few decades, the requirement of high-performance electric drives is increasing in various industrial applications. Because of its rugged construction and low maintenance requirement, induction motor (IM) drive is the most preferred apparatus for various industrial applications [12]. High power, high performance IM drive requires converters consisting of high-voltage and high switching frequency semiconductor devices, which are either expensive or not available due to power rating limitations [13]. This drawback can be overcome by

dividing power between the semiconductor devices used in converter supplying induction motor in order to achieve higher output power. It can be accomplished by employing multiphase drives in high power applications. Multiphase induction motors have several other advantages over their three-phase counterparts such as; reduced amplitude and increased frequency of torque pulsations, reduced rotor harmonic currents, lower DC-link current harmonics, increased power in the same frame (increased torque/ampere), and higher reliability [13, 14]. Recently many research works are being targeted on exploiting the fault tolerance offered by multiphase machines in various applications [7, 15–17]. Moreover, as an existing three-phase induction machine is reconfigured /converted to operate as a six-phase induction machine, weight and volume of the machine will remain the same.

### 1.2.1 Multiphase generators for WECS

A few works of literature can be found on multiphase generators, including six-phase [18–21], nine-phase [22], twelve-phase [23, 24] and eighteen-phase [25] in standalone and grid-connected WECS. Extensive research is going on multiphase induction motor drives and their applications, whereas research on multiphase induction generators is still in its early stages. It remains to be an appealing topic, especially for wind power applications.

Reliability and fault tolerance offered by the multiphase induction generator makes it the best suitable machine for both grid-connected and standalone wind energy conversion systems. In stand-alone mode, multiphase generators' extra winding can be used to improve the voltage regulation, and to maintain the constant frequency operation. A single multiphase generator in standalone mode can deliver more independent loads. Detailed dynamic, steady-state modeling and experimental analysis of a self-excited six-phase induction generator for stand-alone applications have been discussed in [18, 26]. The capacitor value required for maintaining the excitation of self-excited six-phase generator has been detailed in [27]. The six-phase output of this configuration can be supplied to two individual three-phase loads or for a single three-phase load via six-phase to three-phase $\Delta/Y-Y$ three winding transformer. Among all the multiphase machines, asymmetrical six-phase machine is of greatest practical interest for very large generators since it permits re-combination of three-phase power in the step-up transformer bank without the need for increased transformer kVA for phase

shifting. In the study it was found that transformer cost increments (relative to a three-phase application of same kVA and voltage rating) could be limited to 5% or less [28].

Resistance and leakage reactance of induction generator is the main source for its poor voltage regulation. Different methods can be employed for improving the voltage regulation among which prominent ones are by connecting the additional passive elements, reactive power compensator, etc. Improving the voltage regulation by connecting series capacitors in long, short, simple shunt configuration has been proved to be less complex. Series compensation is evaluated in [19]. Voltage and frequency control of self-excited six-phase induction generator by connecting PWM converters in series or shunt configuration with the load is discussed in [20, 29–31]. Detailed temperature and loss assessment of belt driven multiphase induction generator for automotive applications have been performed in [32].

Based on the operation, grid-connected induction generators can be classified into fixed speed and variable speed generators. In fixed speed operation, the generator is directly connected to the grid through a transformer. A dual winding induction generator with a fixed and an adjustable stator is discussed by Levy in [33]. It manually adjusts the second stator winding to match torque and speed of the mechanical and electrical parts while keeping the first winding constant. It eliminates the disadvantages of a three-phase machine, which is unable to regulate the power flow. The system is capable of supplying power to utility grid without an interfacing network; however, the output of this configuration is three-phase.

Squirrel cage induction generators (SCIG), doubly fed induction generators (DFIG) and permanent magnet synchronous generators (PMSG) with back to back voltage source converters are the most preferred topologies in variable speed operation. VSCs with decoupled DC-link eliminate a limitation to employ only three-phase induction generators. On the other hand, utilizing multiphase machines can be beneficial in WECS applications.

In a grid interfaced variable speed multiphase generator, machine side converters control the machine currents to drive it at a certain optimum speed using vector control, direct torque control (DTC) techniques. By doing so, maximum power can be captured from the current wind speed. DTC drive is more robust; however, it gets affected when current-model-based flux estimation is implemented [34]. Vector control techniques are mainly classified into two groups, based on the measurement or estimation of rotor-, stator, or magnetizing flux-linkage

vector amplitude and position [35]. As the requirement of sensors is minimum in indirect vector-control, it is generally preferred over the direct vector control. Reference speed for the vector control is generated by maximum power point tracking (MPPT) technique. A simple MPPT involves a look-up table with optimum turbine operating points calculated at different wind speeds [36]. DC bus voltage will be kept constant by the grid side converter. Grid side converter also controls the active and reactive power flow between the grid and generator. Inherent redundancy and additional degree of freedom offered by ASIG improve the system efficiency. Grid vector-oriented control (GVOC) is applied for grid side PWM converters to maintain the DC-link voltage, and to regulate active and reactive power transition between the grid and generator.

Variable speed operation of a multiphase generator requires the use of multiple three-phase converters either connected in series or in parallel. The series connection of the converter boosts the DC-link voltage level and allows for interfacing with the voltage grid directly. However, this topology requires control to balance the dc-link voltages from drifting apart, thus complicating the entire system. This configuration of multiphase machine side converter has been explored in [37–39]. Parallel connection improves the fault tolerance and reliability of variable speed WECS [40–42]. When multiphase machines are operated with parallel connected converters, unbalanced current can occur between the two three-phase sets. The viability of parallel connected multi-phase converters is analyzed in [43] with indirect field oriented control, which sets the x-y reference voltages and currents to zero. When there is no current flowing in one three-phase set, currents related to switching harmonics increases and machine tends to be operated with asymmetries [44]. It can be overcome by treating two windings as separate three-phase windings, and utilizing two sets of $d-q$ current controllers [45].

### 1.2.2 Integrated Chargers for EVs and PEVs

Battery chargers for PEVs can be classified into two; (a) off-board chargers and (b) on-board chargers. Off-board chargers are designed with large capacity (more than 50 kW) and mounted outside the PEVs, that charges the battery within 30 minutes [46]. The onboard battery charger (OBC) is more desired, because they are placed in the vehicle premises; thus

PEVs can be charged anywhere [47]. Typically, OBC has to be in small size, lightweight, and low cost. In addition, OBC should have the capability to charge the battery with a wide variation of voltages, i.e., from 100-450 [48, 49].

Most PEVs use two individual converters for their onboard battery charger [46, 50]. The first converter is used to convert ac/dc with unity power factor (UPF) operation, i.e. in plug-in charging mode. The second converter is used for boosting the battery voltage as well to control the power during propulsion and regenerative braking modes. In this system, a large number of components are utilized, which has a negative effect on size and weight of the charger.

The number of components and size can be reduced by utilizing the integrated onboard chargers. These integrated chargers can be designed by either utilizing inverter and motor windings in the charging process, or by combining DC/DC front end converter (FEC) with power factor correction converter. The concept of utilizing motor and inverter parts in the charging process is not new. Connecting an inverter between the three-phase induction motor and a rechargeable battery was proposed in [51]. A three-phase open-end winding induction machine along with converter has been integrated for charging process in [52]. In this configuration, during the charging process, the converter is connected to one end of the machine terminals and grid to another. During this, mechanical locking is necessary in order to avoid the machine rotation. To avoid the mechanical locking, a multiphase with H-bridge converter is proposed in [53], however, midpoint needs to be accessed in this topology.

A few integrated charging topologies involving different configurations of multiphase machines have been proposed in [54–56]. Torque development in a multiphase machine during the charging process can be avoided through phase transposition [57]. These topologies can achieve fast charging by connecting to the three-phase grid, and in order to do so inverter and motor are involved in the charging process. The battery is charged only when the vehicle is parked. Motor inductance needs to be considered while developing the control strategies. However, with the use of machine windings in plug-in charging mode, these topologies can perform only boost operation, thus using universal power station having voltage range 90-260 V is not possible.

Instead of integrating DC/AC inverter used in propulsion drive for battery charging, the

bidirectional DC/DC converter connected between the battery and AC/DC PFC converter can be combined to have a converter for all modes. Even these types of integrated converters reduce the total number of components compared to conventional onboard chargers. As battery charging does not involve any machine windings, the converter can be designed as per the requirement of PEV. Authors in [58–60] have proposed the integrated front-end converters focusing especially on battery charging in all modes of operation. Converters proposed in [58] and [59] do not have buck/boost operation in all modes, thus aforementioned benefits cannot be obtained. While integrated converter in [60] uses a large number of semiconductor devices; therefore, it may not be an efficient and cost-effective solution. Both [59] and [60] utilize a large passive filter for power factor correction (PFC). Input currents in these two converters are discontinuous in nature which increases the overall weight and cost of the charger. In [61] and [62], SEPIC based converters have been proposed for the battery charging using three inductors, and at least one extra inductor is also required for propulsion and regenerative braking modes. Thus, the increase of magnetic components has a negative effect on weight, cost and volume of the charger.

### 1.2.3 Space Vector pulse Width Modulation for Multiphase Drives

The stator resistance and leakage reactance of ASIM are less when compared to that of the three-phase machine, which in order reduces the capacity to restrain the stator harmonic currents. Therefore, when the machine is supplied from a VSC, large harmonic currents flow through the stator increases the motor losses. A few solutions are proposed to overcome this situation like adding a harmonic filter, introducing additional mutual inductance, applying special pulse width modulation (PWM) techniques, etc. Solutions like adding a harmonic filter or additional mutual inductance increases the size and cost of the system, whereas PWM techniques can be implemented very easily to the converter supplying induction motor.

PWM techniques can control the harmonic spectrum of output voltage, thereby improving the output efficiency of an inverter [63]. It can also reduce the lower frequency torque pulsation. The most popular switching technique is sinusoidal pulse width modulation (SPWM) as it is very simple to implement, but this technique is unable to utilize the available DC bus voltage to full potential. To improve the DC bus utilization, this technique can also be

implemented with an injection of appropriate harmonics into the reference signal similar to third harmonic injection PWM in the three-phase inverter. However, the effect was found weakened as the number of phases increases [64].

Space vector pulse width modulation is a popular control scheme for the voltage source inverters. In SVPWM, a certain number of space vectors are selected to synthesize the output voltage vector, which has an average value equal to the reference signal. A few space vector pulse width modulation schemes are found advantageous for multiphase drives with reduced stator harmonic currents and lower torque pulsation. SVPWM techniques for multiphase induction machines have been reported in a few literature. SVPWM techniques are utilized to reduce the common-mode voltage of a five-phase drive. In [65], it is achieved by using predictive control, and in [66], by developing an admittance transfer function to balance the DC-bus voltage. A comparative analysis of SVPWM strategies for a five-phase two level VSI drive has been presented [67], and five-phase three-level VSI has been presented in [68]. These studies suggest that output phase voltage from a five-phase VSI can be improved by utilizing both medium and large vectors.

For the six-phase machine, a conventional SVPWM, similar to that of the three-phase SVPWM is reported by Gopakumar et al., in [69]. In this method, two adjacent active vectors of the outer most 12-sided polygon along with two zero sequence vectors are used for synthesizing the space vector. This method utilizes only two active vectors leading to the generation of an output voltage with lower order harmonics. Zhao et al. proposed an SVPWM technique by using vector space decomposition (VSD) method in [70]. In this technique, the voltage space vector is synthesized by using four active vectors of outer most decagon along with a null vector. Vector classification technique was proposed by Baksshai et al., in [71] which is much simpler than vector space decomposition SVPWM. In this particular approach, two identical space vectors of three-phase are phase shifted by 30 electrical degrees are used as the reference. Space vector modulation techniques for multi-level six-phase drive have been discussed in [72, 73], and a generalized multi-level multiphase SVPWM technique is presented in [74]. A few SVPWM methods also focus on reducing the common mode voltage of a dual stator machine using SVPM techniques [75, 76]. In [77], generalized common mode elimination SVPWM for a multiphase drive is presented.

## 1.3 Authors' Contribution

In view of the scope of the work revealed by the literature survey made on multiphase induction machines in general and its application for WECS and EV propulsion in particular, an attempt has been made to make the following contributions during the course of present research work.

- Development of a detailed mathematical model of asymmetrical six-phase induction motor drive with the consideration of mutual leakage coupling and cross saturation coupling between the two three-phase sets. Systematic analysis of different space vector PWM techniques for ASIM drive in terms of torque pulsation and harmonic content: three of them are found in literature, the other one is proposed in the present dissertation.

- Development of indirect rotor field oriented control for ASIM drive without any unbalanced currents or asymmetries associated with switching harmonics. The SVPWM technique, selected based on the comparative analysis, is utilized in the IRFOC developed. Speed protuberance during load variation is minimized by introducing an additional feed-forward loop.

- Development of a variable speed WECS with asymmetrical six-phase induction generator. Dynamic modeling of wind turbine, grid, and grid side converter. Implementation of control strategies for smooth grid and generator side operation. Generator side converters are operated for maximum power point tracking and grid side converters for unity power factor control.

- Performance analysis of asymmetrical six-phase induction generator in self-excited and grid-connected fixed speed operation. Single hardware setup is transformed into different configurations based on the requirement. Analysis of various aspects during steady-state and transient conditions. Examined practical feasibility of ASIG in wind/small hydropower plants.

- Development of a power electronic interface for plug-in electric vehicles involving asymmetrical six-phase induction motor as propulsion drive, a CuK based integrated

converter for battery charging. CuK based bidirectional DC/DC converter, is capable of performing the buck/boost function during all modes of operation.

- Development of a laboratory prototype with a field programmable gate array (FPGA) based controller. Simulation results are validated through experimental results obtained from the laboratory prototype.

## 1.4 Thesis Organization

Apart from this Chapter, the thesis is organized into five more chapters and an Appendix. The works included in each chapter and Appendix are briefly structured as follows:

**Chapter 2** presents the prototype consisting of asymmetrical six-phase induction machine used for the experimental tests. The goal of this chapter is to show the system development required for the research work. All the main units of the setup are detailed: the machine, the power converter, the interface boards and the development control board.

**Chapter 3** deals with the development of an advanced indirect rotor field-oriented control (IRFOC) for ASIM drive with reduced speed disturbances during load variation, and complete removal of unbalanced currents between two three-phase sets. It also focuses on developing a dynamic model of asymmetrical six-phase induction for simulation purposes. A comprehensive comparative study, based on simulation and experimental results of four different space vector pulse-width modulation techniques for voltage source inverter fed asymmetrical six-phase induction machine drive, is also performed.

**Chapter 4** presents the grid interfacing of asymmetrical six-phase induction generator in variable speed WECS using the developed IRFOC. Back to back PWM converters decoupled with DC-link are utilized for grid interfacing of ASIG. Maximum available power in the wind is extracted by using MPPT control, and supplied to the grid with unity power-factor operation. Additionally, performance of asymmetrical six-phase induction machine in self-excited and grid-connected fixed speed wind energy conversion system is analyzed. Various aspects such as efficiency, reliability, and productivity are considered while performing the analysis.

**Chapter 5** proposes a novel power electronic interface with CuK based integrated DC/DC converter, and IRFOC controlled ASIM drive for PEVs. Integrated onboard charger de-

signed is capable of performing buck/boost function during all modes of vehicle operation. It also contains minimum number of components compared to other onboard integrated battery chargers. ASIM drive is utilized in propulsion system of the PEV.

**Chapter 6** summarizes the conclusions drawn from the exhaustive simulation and experimentation carried out in the present research work. This chapter also presents the scope of future work in this field.

Based on this research work, four SCI indexed papers have been published in reputed International Journals. In addition, seven papers are presented and published in International Conferences. The papers are listed as follows:

**Papers Published in Peer-Reviewed Journals**

i. **K. A. Chinmaya**, and G. K. Singh., "Performance Evaluation of Multiphase Induction Generator in Stand-Alone and Grid-Connected Wind Energy Conversion System", **IET Renewable Power Generation**, Vol. 12, No. 7, May 2018, pp. 823-831.

ii. **K. A. Chinmaya**, and G. K. Singh., "Experimental analysis of various space vector pulse width modulation (SVPWM) techniques for dual three-phase induction motor drive, **International Transactions on Electrical Energy Systems**, vol. 29, No. 1, 2018 p. e2678.

iii. **K. A. Chinmaya**, and G. K. Singh., "Integrated onboard single-stage battery charger for PEVs incorporating asymmetrical six-phase induction machine", **IET Electrical Systems in Transportation**, 2018, DOI: 10.1049/iet-est.2018.5015.

iv. **K. A. Chinmaya**, and G. K. Singh., "Modeling and Experimental Analysis of Grid-Connected Six-Phase Induction Generator for Variable Speed Wind Energy Conversion System", **Electric Power Systems Research**, Vol. 166, January 2019, pp.151-162.

**Papers Presented and Published in International Conferences**

i. **K. A. Chinmaya**, and G. K. Singh., "A Plug-in Electric Vehicle (PEV) with Compact Bidirectional CuK Converter and Sturdier Induction motor drive", in Proc. IEEE IES IECON18, October 21-23, 2018, Washington D.C., USA.

ii. **K. A. Chinmaya**, and G. K. Singh., "Modeling and Comparison of Space Vector PWM schemes for a Five-Phase Induction Motor Drive", in Proc. IEEE IES IECON18, October 21-23, 2018, Washington D.C., USA.

iii. **K. A. Chinmaya**, and G. K. Singh., "A Single-Stage Integrated Charger for Electric Vehicles (EVs) and Plug-in Electric Vehicles (PEVs) Incorporating Induction Motor Drive", in Proc. IEEE IES IECON18, October 21-23, 2018, Washington D.C., USA.

iv. **K. A. Chinmaya**, and G. K. Singh., "A Multifunctional Integrated On Board Battery Charger for Plug-in Electric Vehicles (PEVs)", in Proc. Power Electronics and Motion Control (PEMC-2018), August 26-30, 2018, Budapest, Hungary.

v. **K. A. Chinmaya**, and G. K. Singh., "A Compact Integrated Charger with Disturbance Reduced Induction Motor Drive for Plug-in Electric Vehicles (PEVs)", in Proc. of the Ninth Int. Conf. on Future Energy Systems, 2018, Karlsruhe, Germany, pp. 405-407.

vi. **K. A. Chinmaya**, and G. K. Singh., "An Advanced Disturbance Reduction Field-Oriented Control for Six-phase Induction Machine", in Proc. IEEE Int. Conf. Engineer Infinite, March 13 - 14, 2018, Greater Noida, NCR, India.

vii. **K. A. Chinmaya**, and G. K. Singh., "Analysis of Space Vector PWM Technique for Dual Three-Phase Induction Machine", in Proc. IEEE Innovations in Power and Advanced Computing Technologies (i-PACT) 2017, pp. 1-5.

# CHAPTER 2

# SYSTEM DEVELOPMENT

## 2.1 Introduction

The laboratory setup used for experimental tests is described in this chapter. A single asymmetrical six-phase machine is utilized for two different applications;

i. Grid interfacing of asymmetrical six-phase induction generator for variable speed wind energy conversion systems.

ii. Asymmetrical six-phase induction machine with an integrated onboard single-stage battery charger for plug-in electric vehicles PEVs.

This chapter explains the structure and development of both systems.

## 2.2 Schematic

In both systems, the asymmetrical six-phase induction machine is operated with indirect rotor field-oriented control. ASIM is coupled with a 2.5-hp variable speed drive (VSD) functioning as a prime mover in torque mode. DR-2112, a rotary torque encoder and ROD-436, a speed encoder are coupled with ASIM for sensing the torque and speed.

In the first configuration, three IGBT SEMIKRON converters are utilized for grid interfacing of ASIG. Two three-phase IGBT converters are connected to two sets of ASIG windings. A grid side IGBT converter is connected in parallel to two generator side converters sharing a common DC-link.

The general block schematic of ASIG for variable speed wind energy conversion system is depicted in 2.1.

For the second set of configuration, ASIM is utilized as a power electronic interface for PEVs. In this setup, the six-phase induction machine is integrated with the CuK converter. SEMIKRON IGBT switches are utilized in developing the bidirectional DC/DC converter, and two SEMIKRON converter modules connected in parallel are utilized for driving ASIM.

The general block schematic of ASIM integrated with bidirectional DC/DC converter for PEVs is depicted in 2.2.

In both the configurations, grid voltage, battery voltage, DC-link voltage, output battery current and machine currents are measured using voltage and current sensors. All the waveforms are recorded in Agilent Technology DSO1014 oscilloscope. The grid current and power quality are measured through FLUKE power quality analyzer. Control algorithms are implemented and tested with a FPGA based dSPACE DS1104 system plugged into a personal computer.

## 2.3 Experimental Setup

To evaluate the performance of ASIM for two different applications, an experimental setup is developed in the laboratory. Actual picture of the developed prototype is shown in Fig. 2.3. Prototype mainly consists of five major components with other supplementary equipment.

i. Asymmetrical six-phase induction machine, ii. The power electronic converters, iii. Prime mover, iv. Signal conditioners, v. The dSPACE DS1104 controller board.

### 2.3.1 Asymmetrical six-phase induction machine

Asymmetrical six-phase induction machine is developed by splitting the phase belt of a three-phase, six-pole, 36-slots induction machine. All the 72 stator terminals are taken out on a connection plate outside of the machine casing so that several winding schemes can be realized with varying number phase and pole configurations. The stator of ASIG is composed of two star connected three-phase sets (abc and xyz) with a phase displacement of 30 electrical degrees. Neutral point of two three-phase sets (star connection) are kept isolated in order to prevent physical fault propagation and to prevent the flow of triplen harmonic current. All the 72 terminals can be identified in the ASIM prototype shown in Fig. 2.4.

During the performance analysis, the three-phase machine is realized by reconnecting the stator terminals of test machine used as ASIM. Connection diagram of six-phase and three-phase induction machines are shown in Figs. 2.5 and 2.6 respectively.

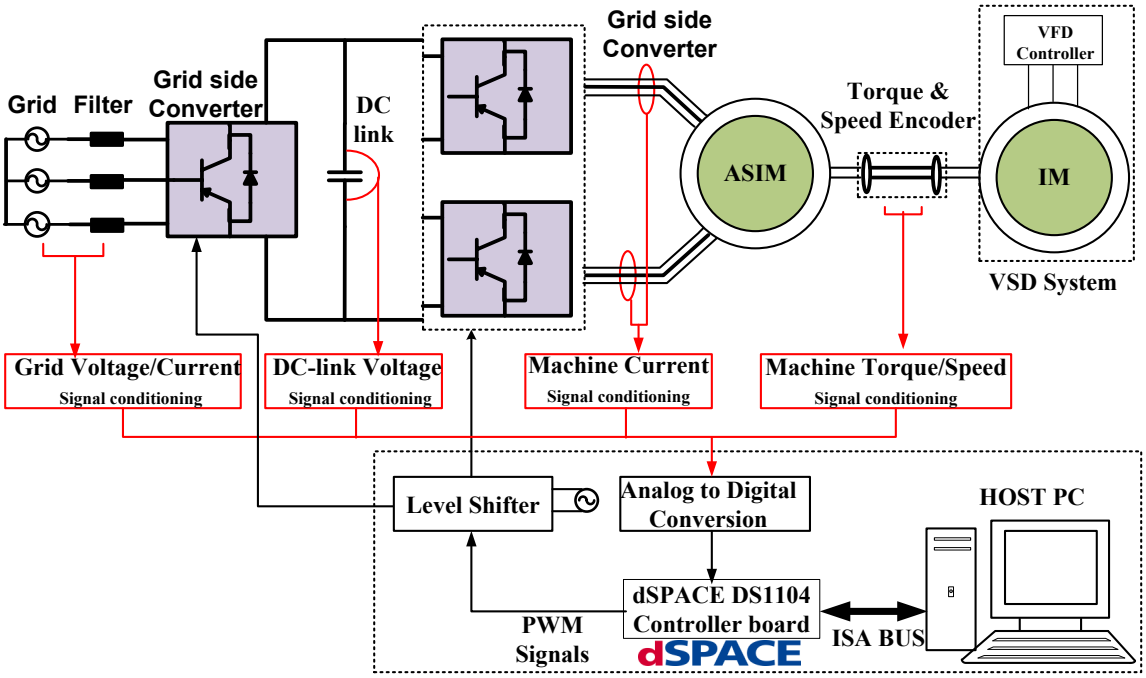


Fig. 2.1: General block schematic of ASIG for variable speed wind energy conversion systems.

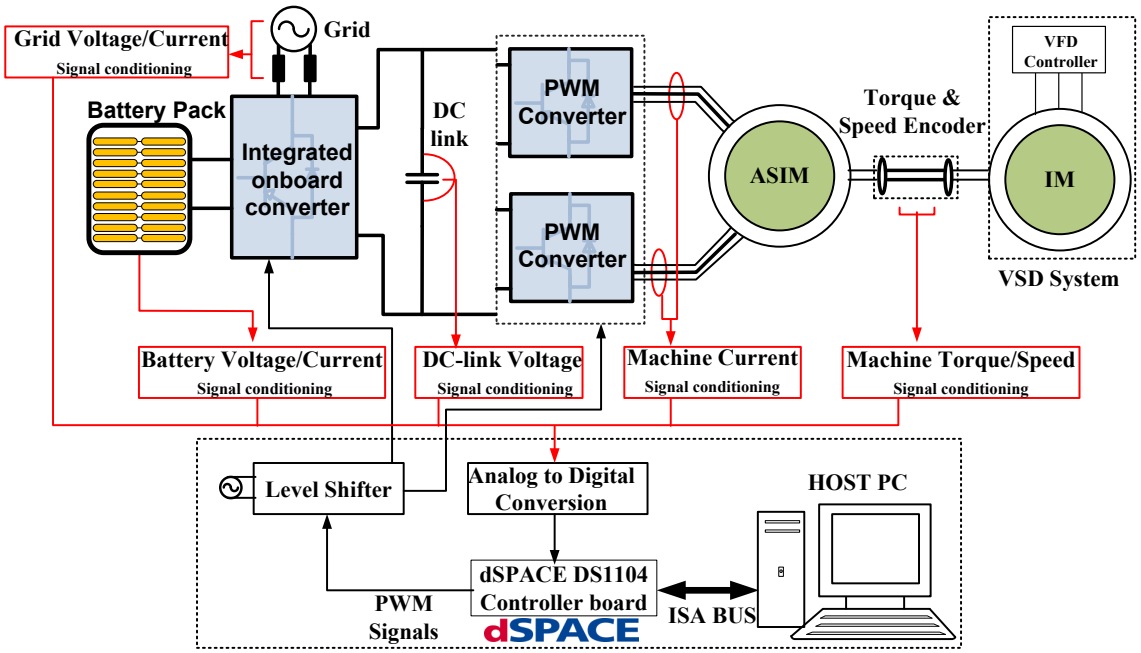


Fig. 2.2: General block schematic of ASIM with bidirectional DC/DC converter for PEVs.

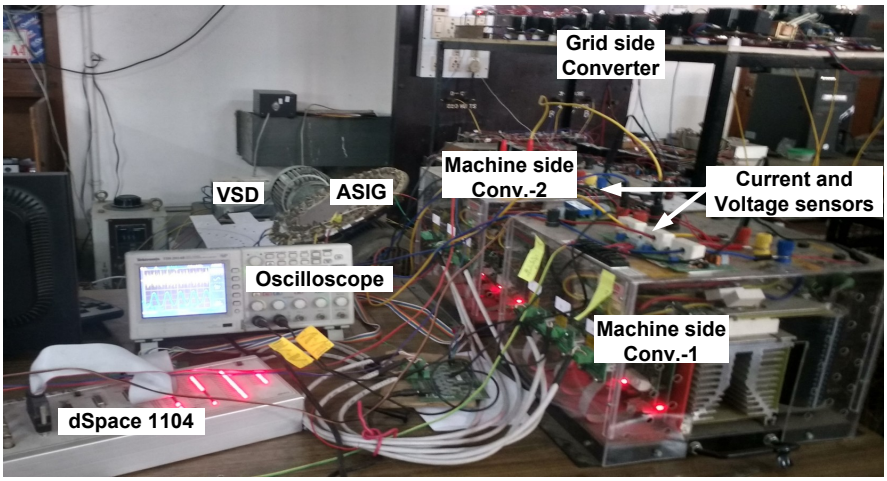


Fig. 2.3: Experimental prototype developed at the laboratory.

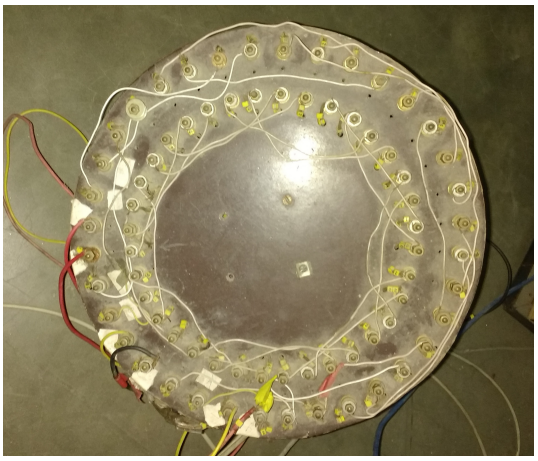

Fig. 2.4: The prototype of Asymmetrical six-phase induction machine.

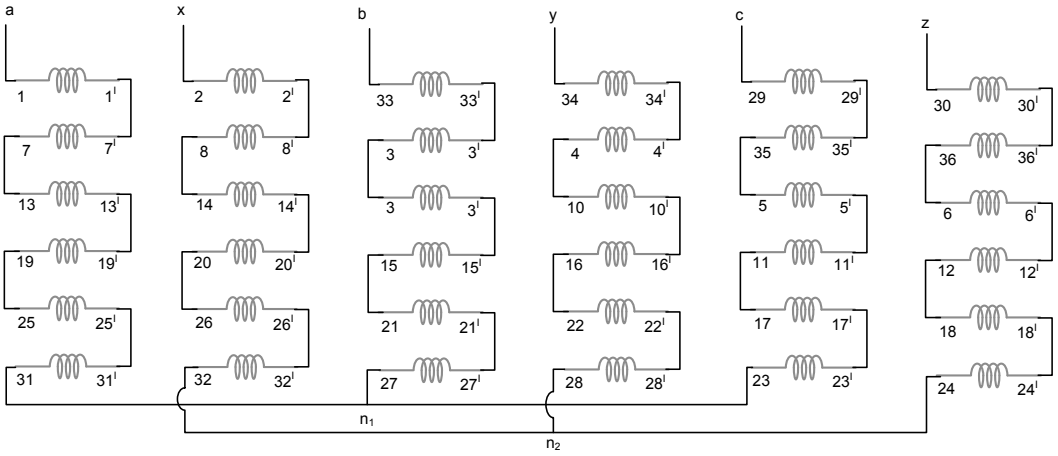


Fig. 2.5: Winding diagram for asymmetrical six-phase induction machine.

### 2.3.2 Prime mover

The test machine is coupled with a 2.5-hp induction motor. The motor is supplied by a TOSHIBA VF-A7 high-performance inverter, thus operating as a variable speed drive (VSD). The prime mover system is shown in Fig. 2.7 It can be operated in speed control mode, and also torque control mode. When VSD is operated in speed control mode, the motors rotating speed is controlled with higher accuracy, even in low-speed ranges. The motor torque can be controlled in the torque control mode. The motor speed is determined by the relationship between the load torque and motor torque. In this work, VSD is operated in torque control mode.

### 2.3.3 Power Electronic Converters

During grid integration of ASIG, three SEMIKRON converter modules are utilized. Each module consists of three legs and each leg has two IGBT switches. DC capacitor bank is connected to the inverter by laminated bus-bars. Each module has three drivers, a driver is an interface unit between the power module and controller. Each driver drives two switches of the respective module. Three-phase inverter module utilized for the experiment is presented in Fig. 2.8a.

For implementing PEI for PEVs, two SEMIKRON converter modules are interfaced with a CuK converter developed by utilizing SEMIKRON IGBT switches with SKYPER 32 R Pro driver circuit. A single set constitutes of an adapter board, a driver board and an IGBT half bridge with two switches. Adapter board can be customized by allowing adaptation and optimization to the used IGBT module. The SKYPER 32PRO driver core constitutes an interface between the IGBT modules and controller. Functions for driving, potential separation and protection are integrated into the driver. A half-bridge IGBT set with adapter and driver board is shown in Fig. 2.8b.

### 2.3.4 Signal conditioners

Signal conditioners are sensors and encoders utilized to detect, process and redirect the information to controller board. In this setup, four types of signal conditioners are utilized:

i. Voltage Sensor, ii. Current Sensor, iii. Speed Encoder, iv. Torque Encoder.

#### *2.3.4.1 Voltage Sensor*

The AC and DC voltages are measured with AD202JN isolation amplifier. It is supplied from a +15V DC supply. Small size, high accuracy and minimal power consumption make AD202JN a preferred candidate in the experimental setups. Fig 2.9a shows circuit diagram of the voltage sensor. It also consists of two potentiometers and two resistances. The scaled output from the sensor is at terminal 19, and it is fed to ADC board in dSPACE for further processing. The PCB layout and actual sensor are shown in Figs. 2.9b and c.

#### *2.3.4.2 Current Sensor*

Currents are measured with hall effect TELCON HTP25 sensor. The current sensors provide the galvanic isolation between the high voltage power circuit and a low voltage control circuit. It requires a nominal supply voltage of the range $pm12$ to $pm15V$. A dual supply base LF353 operational amplifiers are used to convert the current measured into scaled-down voltage signal level required by ADC channel. Circuit diagram of the current sensor is depicted in 2.10a. A PCB layout and actual picture of the current sensor are depicted in Figs. 2.10b and c.

#### *2.3.4.3 Speed Encoder*

ROD- 436 is an incremental rotary encoder with integrated bearings and a solid shaft. The encoder shaft is connected with the measured shaft through a separate rotor coupling. The coupling compensates the axial motion and misalignment between the encoder shaft and measured shaft. This relieves the encoder bearing of additional external loads that would otherwise shorten its service life. Diaphragm and metal bellow couplings are designed to connect the rotor of the ROD encoder. ROD 436 requires a 10-30V power supply.

Incremental measuring methods consist of a periodic grating structure. The position information is obtained by counting the individual increments (measuring steps) from some point of origin. The output of the encoder is provided to a separate incremental encoder channel present in the controller board.

ROD rotary encoder with a line count up to 5000 signal periods per revolution has a system accuracy of 15 angular seconds. The rotary encoder utilized in the experimental setup is depicted in Fig. 2.11a.

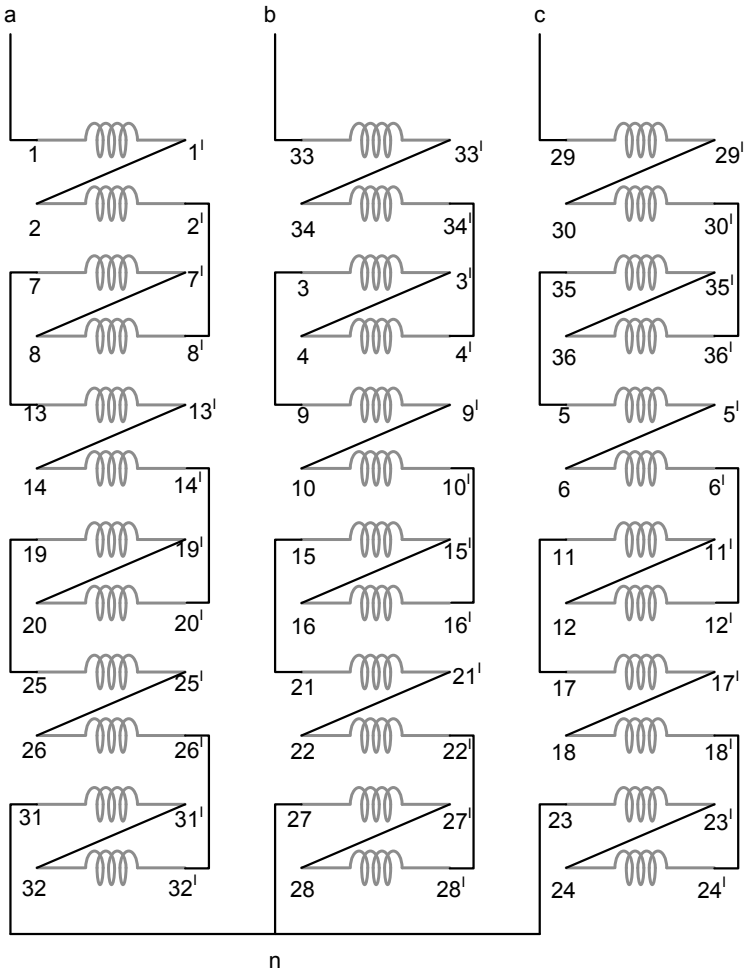


Fig. 2.6: Winding diagram for conventional three-phase induction machine.

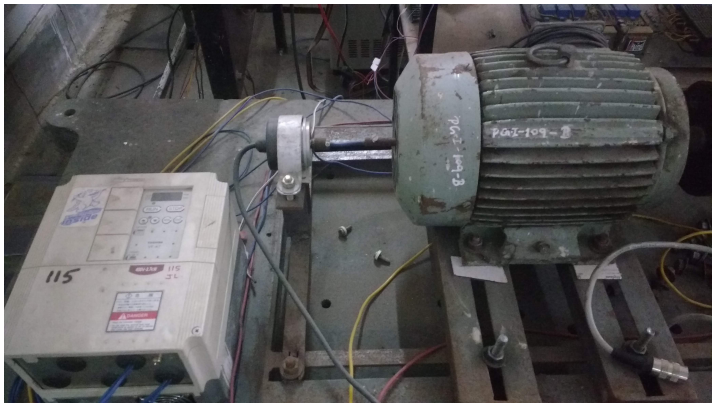

Fig. 2.7: Induction motor with high-performance inverter operating as a prime mover.

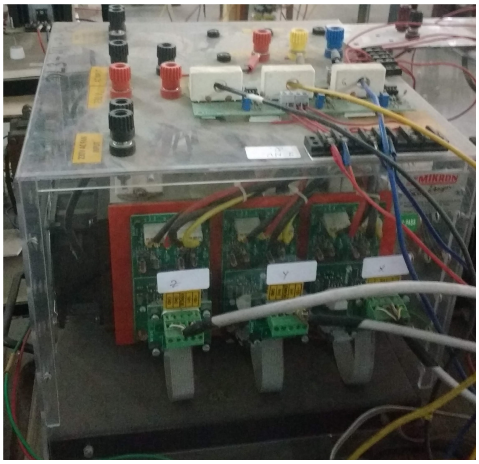

(a)

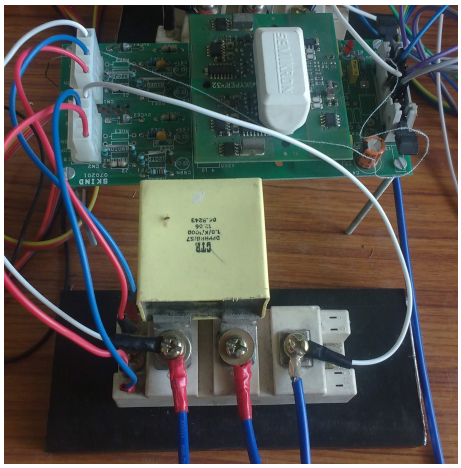

(b)

Fig. 2.8: (a) Three-phase IGBT inverter utilized for experiment, (b) Half bridge IGBT set with adapter and driver board.

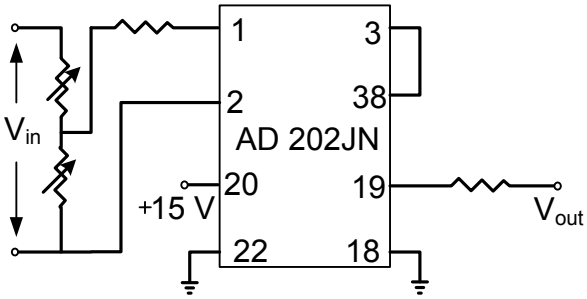


(a)

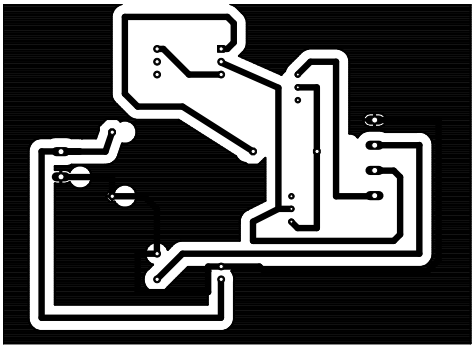

(b)

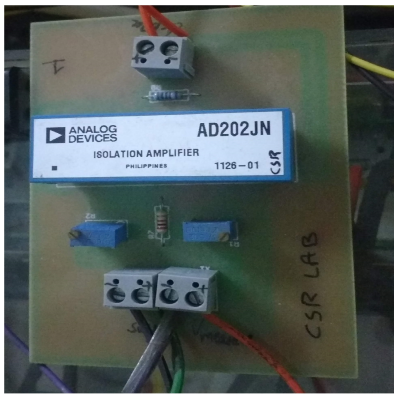


(c)

Fig. 2.9: (a) Circuit diagram of voltage sensor using AD202JN, (b) PCB layout of voltage sensor, (c) actual voltage sensor utilized in the experimental setup.

*2.3.4.4 Torque Encoder*

The DR-2112 torque sensor shown in Fig. 2.11b, consists of a torsion shaft. Depending on the design, the mechanical connection possibilities are executable with round shafts or feather key connections etc. The torsion shaft, applied with two strain gauge full bridges, is bedded in the housing through ball bearings. For signal transmission and/or supply of the strain gauge full bridges, a rotating transformer, according to the principle of a transformer, is arranged in the sensor. For supply and measuring signal conditioning, electronics are integrated into the stator and rotor.

The torque sensor is digitally interfaced with the controller board using RS485 for the signal output and automatic sensor identification.

### 2.3.5 The dSPACE DS1104 controller board

The dSPACE DS1104 is an FPGA based controller board interfaced with a personal computer. The I/O resources of the DS1104 are split between two processors on the board, the Master PPC (Power PC) and the Slave DSP F240. Master PPC consists of 8 A/D converter channels which are used for processing of the signal received from the voltage and current sensors. It has two incremental encoder channels provided specially for signal receiving from speed sensors. A serial interface compatible with RS485 is digitally interfaced with the torque encoder.

20 digital I/O channels are utilized for PWM generation inverter's IGBT's with a dead time of 3.3$\mu$S. 8 D/A converter ports are used to display the calibrated signals under noteworthy conditions during the experimentation. The dSPACE DS1104 utilized for the experimental purposes is shown in Fig. 2.12.

### 2.3.6 Supplementary equipments

The PWM signals generated by the controller board are boosted as per IGBT gate requirement by using a level shifter card as shown in Fig. 2.13a. Coupling inductors shown in Fig. 2.13b are connected between the grid and converter. It filters the high-frequency ripples generated from converter switching. An auto-transformer shown in Fig. 2.13c is also used while grid interfacing; and by doing so, fault transmission between the grid and WECS can be avoided. During grid interfacing of six-phase induction generator in fixed speed mode, a $\Delta$**/Y-Y** six-

phase to three-phase transformer as shown in Fig. 2.13d is utilized for combining the outputs of two three-phase winding sets.

The voltage and current sensors are supplied from DC supply as shown in Fig. 2.14a. Experimental waveforms are recorded using Agilent Technology, DSO1014A oscilloscope shown in Fig. 2.14b. The grid voltage, current and power factor are recorded through FLUKE power quality analyzer shown in Fig. 2.14c. While operating as PEI, four battery stack units each of 12 V 26 Ah are utilized, these are depicted in Fig. 2.14d.

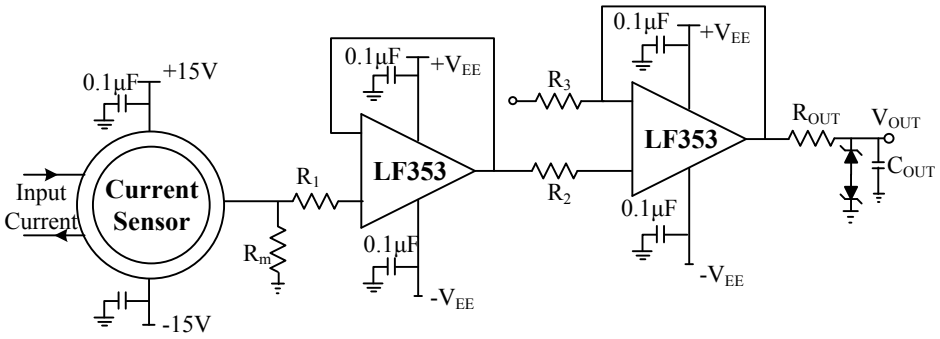


(a)

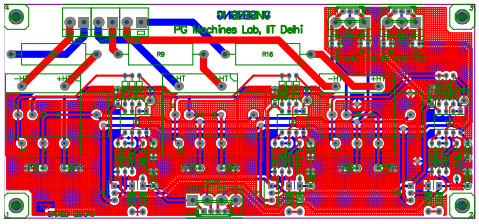

(b)

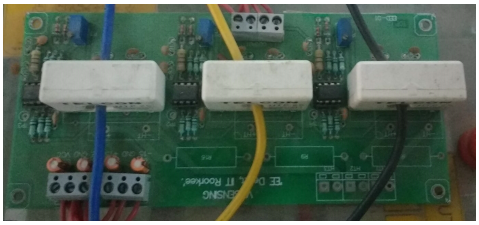

(c)

Fig. 2.10: (a) Circuit diagram of current sensor using TELCON HTP25, (b) PCB layout of current sensor, (c) actual current sensor utilized in the experimental setup.

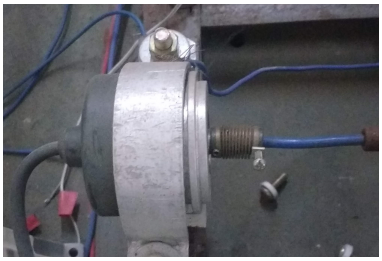

(a)

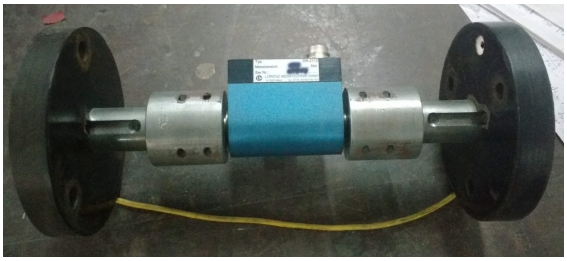

(b)

Fig. 2.11: (a) The speed encoder, and (b) torque encoder utilized in the experimental setup.

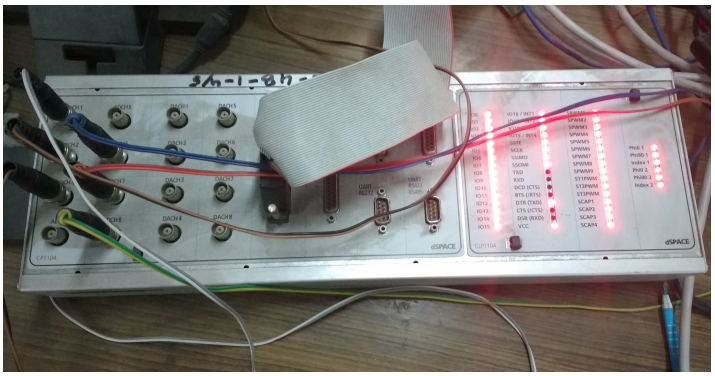

Fig. 2.12: The dSPACE DS1104 controller board.

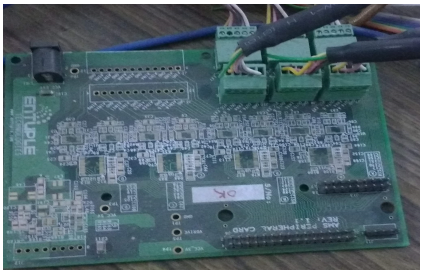

(a)

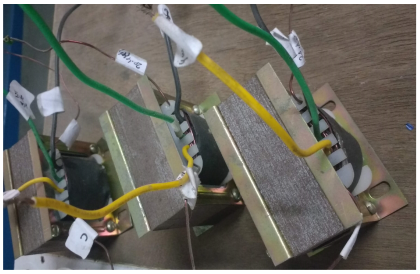

(b)

(c)

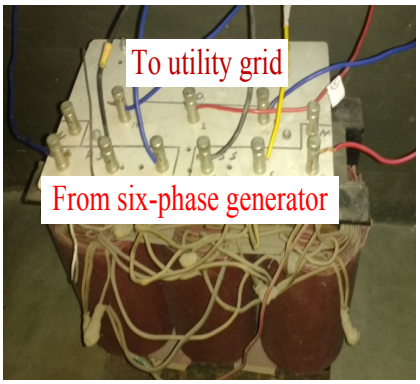


(d)

Fig. 2.13: Supplementary equipments utilized during experiment:(a) Level shifter card, (b) Filter inductors, (c) auto transformer, (d) six-phase to three-phase $\Delta/Y - Y$ transformer.

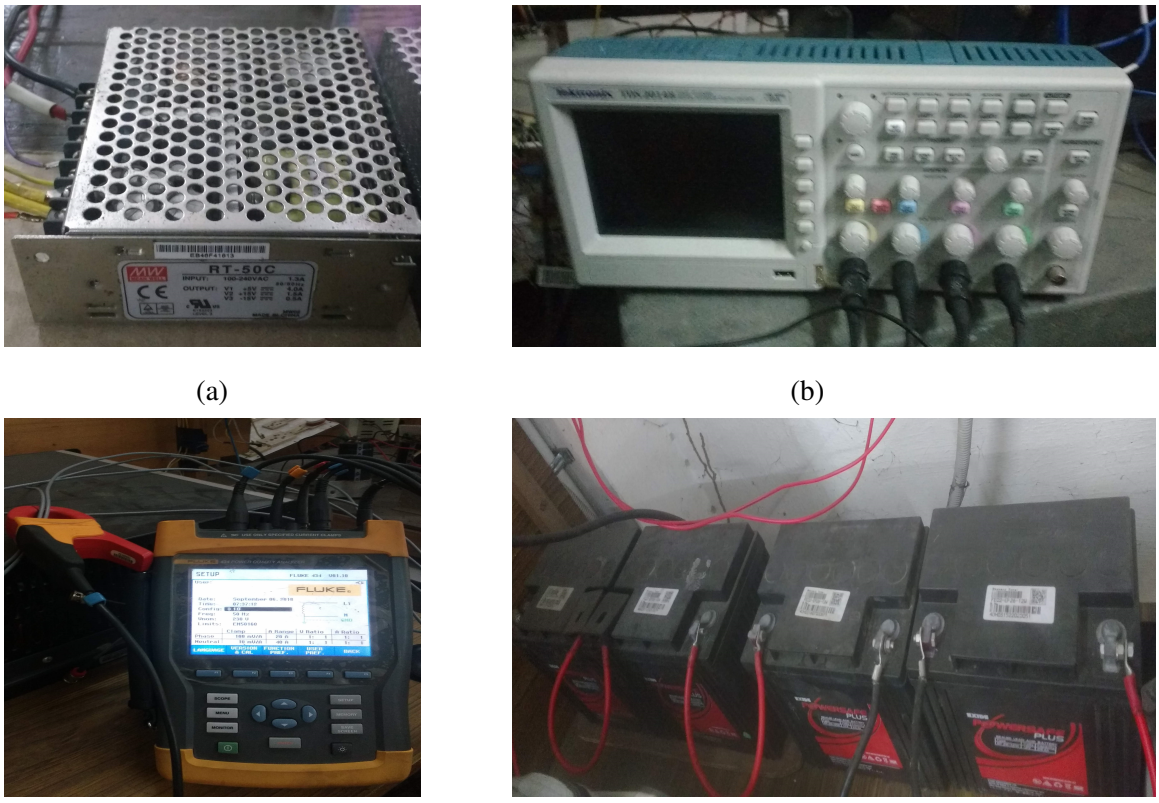


(a) (b)

(c) (d)

Fig. 2.14: (Supplementary components utilized during experiment:a) DC supply for voltage and current sensors, (b) Digital storage oscilloscope (DSO), (c) Fluke power quality analyzer, (d) Battery stack for power storage.

# CHAPTER 3

# MODELING AND ANALYSIS OF SIX-PHASE INDUCTION MACHINE DRIVE

## 3.1 Introduction

Multiphase induction machines can be constructed with any number of windings more than three, such as five, six, seven, nine, twelve etc. The number of stator phases of any existing three-phase machine (induction or synchronous) will be equal to the number of coils per pole pair, which is always greater than three. Hence, the available three-phase machine can be easily converted to operate on higher phases by reconnecting their coils terminals without any additional expenses.

In general, the required angular spacing between multiple winding sets for best performance is $\pi/n$ for an even number of three-phase sets and $2\pi/n$ for an odd number of three-phase sets, where $n$ is the total number of stator phase [13]. According to this, for best performance in case of a six-phase configuration, two sets of three-phase stator windings must be spatially phase shifted by 30 electrical degrees. This configuration is generally referred to as asymmetrical six-phase induction machine (ASIM) as the machine phase windings are not identically displaced. It is also called as dual-three phase, split-phase and dual stator winding induction machine. This machine can be constructed from an existing three-phase machine, by splitting the sixty-degree phase belt of the three-phase machine into two portions each spanning thirty degrees, thus reducing the initial cost.

The neutral of stator winding can be configured to a single point or kept isolated. Fault transmission from one set of winding to the other set can be avoided in case of separate neutral points. ASIM has an edge over other multiphase machines, i.e., when stator sets of this machine are supplied from individual six-step inverters, the pulsating sixth harmonic torque component produced from individual stators will be cancelled due to the opposition [78]. It also requires less coil insulation when compared to conventional six-phase induction machine [79]

This chapter discusses the detailed modeling and analysis of the asymmetrical six-phase

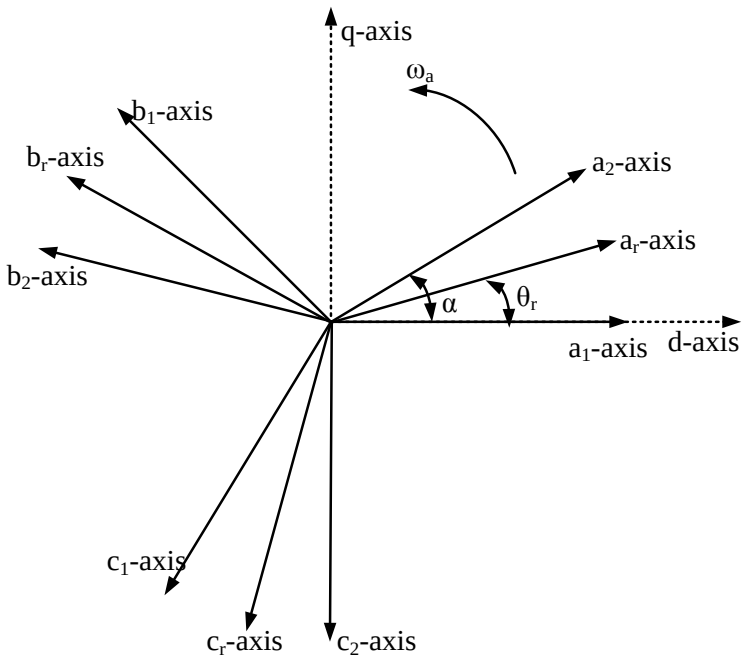


Fig. 3.1: Phasor representation of an asymmetrical six-phase induction machine.

induction machine drive. Three different well-known space vector pulse width modulation (SVPWM) techniques are presented. Then, a three-phase SVPWM is modified for six-phase application and refereed as common mode voltage injection SVPWM. All four SVPWM techniques are evaluated in terms of torque pulsation and harmonic content. Thereafter, a simple indirect-field oriented control with two sets of PI controller is developed for variable speed operation of ASIM, and the best suitable SVPWM resulted from the comparative analysis is utilized in it.

## 3.2 Modeling of asymmetrical six-phase induction machine

All the electrical machines can be modeled as motor and generator with the same set of equations. Similarly, multiphase induction machines can be effectively modeled by either transforming the individual pair of three-phase windings into '$n$' number of phases as presented in [78] or by using vector space decomposition transformation equations suggested in [80].

In this work, machine model is formulated in arbitrary frame of reference by transforming the individual three-phases into two orthogonal subspaces, which are denoted by $d_1$-$q_1$, $d_2$-$q_2$

and a set of zero sequence component.

Asymmetrical six-phase induction machine with phase displaced three-phase winding sets is modeled by considering the following assumptions [81]: i. The generator air gap flux is uniform, ii. eddy currents, friction and windage losses, and saturation are neglected, ii. machine stator and rotor windings are sinusoidally distributed, vi. in order to avoid fault transmission between two stator winding sets, the neutral point of both three-phase sets are isolated.

Phasor representation of stator and rotor windings of a six-phase induction machine is given in Fig. 3.1. Two three-phase stator windings labeled $a_1, b_1, c_1$ and $a_2, b_2, c_2$ are displaced by an angle $\alpha$, in this case, it is thirty electrical degrees. Neutral of both sets are kept isolated to prevent the fault transmission from one set of winding to another. Two stator windings of each three-phases are distributed uniformly and are displaced by 120°apart. The rotor windings $a_r, b_r, c_r$ are also distributed sinusoidally with their axis displaced by 120°.

The voltage equations of asymmetrical six-phase induction machine in stationary frame may be expressed as,

$$v_{s1} = i_{s1} r_s + p\lambda_{s1} \tag{3.1a}$$

$$v_{s2} = i_{s2} r_s + p\lambda_{s2} \tag{3.1b}$$

$$v_r = i_r r_r + p\lambda_r \tag{3.1c}$$

Stator and rotor flux linkages may be expressed as

$$\lambda_{s1} = L_{l1} i_{s1} + L'_{lm}(i_{s1} + i_{s2}) - L'_{ldq} i_{s2} + L_m(i_{s1} + i_{s2} + i_r) \tag{3.2a}$$

$$\lambda_{s2} = L_{l2} i_{s2} + L'_{lm}(i_{s2} + i_{s2}) - L'_{ldq} i_{s1} + L_m(i_{s1} + i_{s2} + i_r) \tag{3.2b}$$

$$\lambda_r = L_{lr} i_r + L'_m(i_{s1} + i_{s2} + i_r) \tag{3.2c}$$

$$L'_{lm} = \frac{N_1}{N_2} L_{lm}, L'_{ldq} = \frac{N_1}{N_2} L_{ldq} \tag{3.2d}$$

In the above equations, $s1$ and $s2$ subscripts represent the variables and parameters associated with stator set 1 and 2 respectively. Similarly, the $r$ subscript represents the variables and parameters associated with rotor circuits.

$N_1$ and $N_2$ are the number of turns of $a_1b_1c_1$ and $a_2b_2c_2$ windings respectively, and are equal in the present case. $L_{lm}$ is the common mutual leakage inductance between the two sets of stator windings, $L_m$is the mutual inductance between stator and rotor, and $L_{ldq}$ is the cross-saturation coupling between d- and q-axis of the stator. Common mutual leakage inductance $L'_{lm}$ represents the fact that the two sets of stator windings occupy the same slots, and are therefore, mutually coupled by a component of leakage flux.

## 3.3 Transformation of machine variables

Transformation of machine variables is performed to eliminate the time-varying inductances. Transformation of stationary circuit variables in arbitrary reference frame can be obtained as

$$\begin{aligned} f_{1qd0} &= \overline{T_1} f_{s1} \\ f_{2qd0} &= \overline{T_2} f_{s2} \end{aligned} \tag{3.3}$$

$$\begin{aligned} f_{1qd0} &= [f_{q1}, f_{d1}, f_{01}]^T \\ f_{2qd0} &= [f_{q2}, f_{d2}, f_{02}]^T \\ f_{s1} &= [f_{a1}, f_{b1}, f_{c1}]^T \\ f_{s2} &= [f_{a2}, f_{b2}, f_{c2}]^T \end{aligned} \tag{3.4}$$

$$[\overline{T_1}] = \frac{2}{3}\begin{bmatrix} cos\theta & cos\left(\theta - \frac{2\pi}{3}\right) & cos\left(\theta + \frac{2\pi}{3}\right) \\ sin\theta & sin\left(\theta - \frac{2\pi}{3}\right) & sin\left(\theta + \frac{2\pi}{3}\right) \\ \frac{1}{2} & \frac{1}{2} & \frac{1}{2} \end{bmatrix}$$

$$[\overline{T_2}] = \frac{2}{3}\begin{bmatrix} cos\delta & cos\left(\delta - \frac{2\pi}{3}\right) & cos\left(\delta + \frac{2\pi}{3}\right) \\ sin\delta & sin\left(\delta - \frac{2\pi}{3}\right) & sin\left(\delta + \frac{2\pi}{3}\right) \\ \frac{1}{2} & \frac{1}{2} & \frac{1}{2} \end{bmatrix}$$

where, $\theta$ is the angle of rotational transformation for the stator, and $\delta = \theta - \pi/6$. The above transformation can be applied to an *n*-phase machine with *n*=3*k*, *k*=2,3,4..etc. For the rotor circuit $\theta$ is replaced by $\theta$-$\theta_r$.

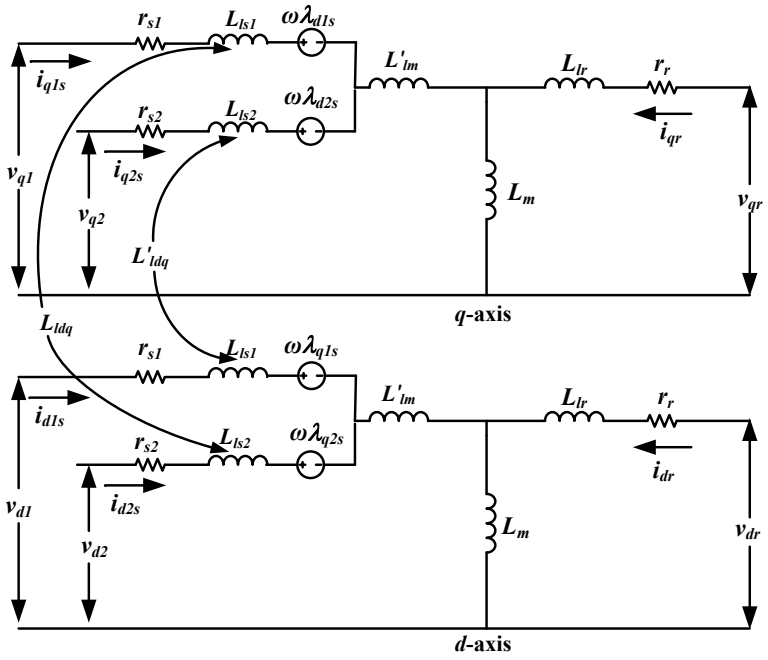


Fig. 3.2: $d-q$ axis equivalent circuit of asymmetrical six-phase induction machine.

The $d-q$ axis equivalent circuit of the six-phase induction machine is shown in Fig. 3.2. The voltage equations for ASIM in an arbitrary frame of reference can be written as, [82].

$$\begin{aligned} v_{1qd0} &= r_s i_{1qd0} + \omega_a \lambda_{1dq0} + p\lambda_{1qd0} \\ v_{2qd0} &= r_s i_{2qd0} + \omega_a \lambda_{2dq0} + p\lambda_{2qd0} \\ v_{rqdo} &= r_r i_{rqd0} + (\omega_a - \omega_r)\lambda_{rdq0} + p\lambda_{rqd0} \end{aligned} \tag{3.5}$$

where, $\omega_a$ is the arbitrary reference speed and $p$ denotes differentiation.

The equations 3.5 is often written its expanded form i.e.,

$$v_{q1} = r_{s1} i_{q1} + \omega_a \lambda_{d1} + p\lambda_{q1} \tag{3.6a}$$

$$v_{d1} = r_{s1} i_{d1} - \omega_a \lambda_{q1} + p\lambda_{d1} \tag{3.6b}$$

$$v_{q2} = r_{s2} i_{q2} + \omega_a \lambda_{d2} + p\lambda_{q2} \tag{3.6c}$$

$$v_{d2} = r_{s2} i_{d2} - \omega_a \lambda_{q2} + p\lambda_{d2} \tag{3.6d}$$

$$0 = r_r i_{qr} + (\omega_a - \omega_r)\lambda_{dr} + p\lambda_{qr} \tag{3.6e}$$

$$0 = r_r i_{dr} - (\omega_a - \omega_r)\lambda_{qr} + p\lambda_{dr} \tag{3.6f}$$

Stator and rotor flux linkages can be expressed as,

$$\lambda_{q1} = L_{l1} i_{q1} + L'_{lm}(i_{q1} + i_{q2}) - L'_{ldq} i_{d2} + L_m(i_{q1} + i_{q2} + i_{qr}) \tag{3.7a}$$

$$\lambda_{d1} = L_{l1} i_{d1} + L'_{lm}(i_{d1} + i_{d2}) - L'_{ldq} i_{q2} + L_m(i_{d1} + i_{d2} + i_{dr}) \tag{3.7b}$$

$$\lambda_{q1} = L_{l2} i_{q2} + L'_{lm}(i_{q1} + i_{q2}) - L'_{ldq} i_{d1} + L_m(i_{q1} + i_{q2} + i_{qr}) \tag{3.7c}$$

$$\lambda_{d1} = L_{l2} i_{d2} + L'_{lm}(i_{d1} + i_{d2}) - L'_{ldq} i_{d2} + L_m(i_{d1} + i_{d2} + i_{dr}) \tag{3.7d}$$

$$\lambda_{qr} = L_{lr} i_{qr} + L'_m(i_{q1} + i_{q2} + i_{qr}) \tag{3.7e}$$

$$\lambda_{dr} = L_{lr} i_{dr} + L'_m(i_{d1} + i_{d2} + i_{dr}) \tag{3.7f}$$

The torque and rotor speed equations of the ASIM can be expressed as

$$T_{em} = \frac{3}{2}\frac{P}{2} L_m[i_{dr}(i_{q1} + i_{q2}) - i_{qr}(i_{d1} + i_{d2})] \tag{3.8}$$

$$T_{em} = \frac{3}{2}\frac{P}{2}\frac{L_m}{L_r}[(i_{q1} + i_{q2})\lambda_{dr} - (i_{d1} + i_{d2})\lambda_{qr}] \tag{3.9}$$

$$\frac{\omega_r}{\omega_b} = \frac{1}{p}\left[\left(\frac{1}{\omega_b}\right)\left(\frac{P}{2}\right)\left(\frac{1}{J}\right)(T_{em} - T_{sh})\right] \tag{3.10}$$

where, $T_{sh}$ is the prime mover shaft torque, $P$ is the number of poles, $J$ is the moment of inertia, $\omega_b$ is the base speed and $p$ is $\frac{d}{dt}$

It is worthwhile to mention here as machine is reconfigured by phase belt splitting, stator resistance and stator reactance will be same for both the three-phase sets i.e.,

$$\begin{aligned} r_{s1} &= r_{s2} = r_s \\ L_{ls1} &= L_{ls2} = L_{ls} \end{aligned} \tag{3.11}$$

## 3.4 Modeling of six-phase VSI

Power circuit topology of a six-phase two-level VSI supplying ASIM is as shown in Fig. 3.3. It can also be realized as two three-phase inverters sharing a common DC bus voltage ($V_{DC}$). The output phases of machine windings are denoted as $a1, b1, c1$ and $a2, b2, c2$ and inverter

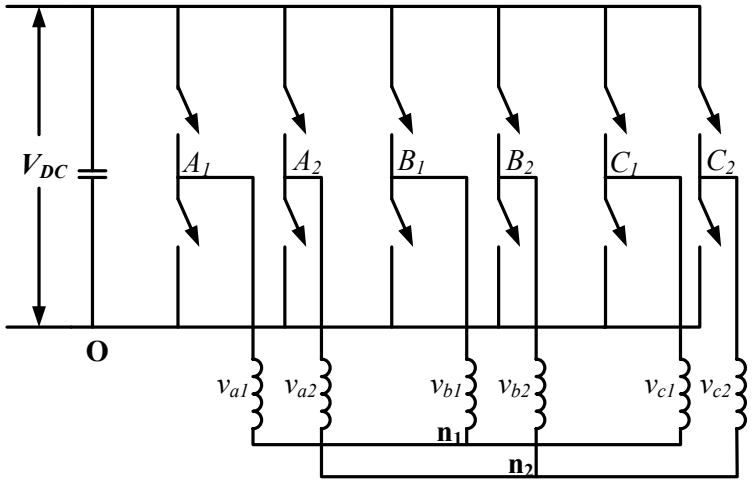


Fig. 3.3: Six-phase voltage source inverter connected to six-phase induction motor.

leg pole points as $A_1$,$A_2$,$B_1$,$B_2$,$C_1$,$C_2$. Phase voltages can be realized in terms of inverter leg voltages as,

$$v_{a1} = \left(\frac{2}{3}\right) v_{A_1} - \left(\frac{1}{3}\right) (v_{B_1} + v_{C_1}) \tag{3.12a}$$

$$v_{b1} = \left(\frac{2}{3}\right) v_{B_1} - \left(\frac{1}{3}\right) (v_{C_1} + v_{A_1}) \tag{3.12b}$$

$$v_{c1} = \left(\frac{2}{3}\right) v_{C_1} - \left(\frac{1}{3}\right) (v_{A_1} + v_{B_1}) \tag{3.12c}$$

$$v_{a2} = \left(\frac{2}{3}\right) v_{A_2} - \left(\frac{1}{3}\right) (v_{B_2} + v_{C_2}) \tag{3.12d}$$

$$v_{b2} = \left(\frac{2}{3}\right) v_{B_2} - \left(\frac{1}{3}\right) (v_{C_2} + v_{A_2}) \tag{3.12e}$$

$$v_{c2} = \left(\frac{2}{3}\right) v_{C_2} - \left(\frac{1}{3}\right) (v_{A_2} + v_{B_2}) \tag{3.12f}$$

In a six-phase VSI, voltages are projected into six-dimensional space having two orthogonal two-dimensional planes called as $d_1$-$q_1$ and $d_2$-$q_2$ and a zero sequence plane $0_1$-$0_2$. In a true six-phase machine having a single neutral $0_1$-$0_2$ plane lies on a straight line; therefore, in reality, it's a five-dimensional transformation. However, in ASIM, all the vectors of $0_1$-$0_2$ are mapped to origin resulting in a four dimensional system, furthermore simplifying the control. Space vectors for ASIM in the stationary frame, using magnitude invariant transformation can

be defined as,

$$v_{d_1q_1} = v_{d_1} + jv_{q_1} = (2/6)(v_{a1} + a^4 v_{b1} + a^8 v_{c1} + a v_{a2} + a^5 v_{b2} + a^9 v_{c2}) \tag{3.13}$$

$$v_{d_2q_2} = v_{q_2} + jv_{q_2} = (2/6)(v_{a1} + a^8 v_{b1} + a^{16} v_{c1} + a^5 v_{a2} + a v_{b2} + a^9 v_{c2}) \tag{3.14}$$

where, a=exp(j$\pi$/6)

## 3.5 Space vector pulse width modulation for ASIM drive

The 64 switching state vectors of a six-phase inverter can be represented as vectors two two-dimensional vector spaces. Space vectors in $d_1$-$q_1$ plane and $d_2$-$q_2$ plane of a six-phase VSI are shown in the Fig. 3.4a and Fig. 3.4b respectively. An m-level n-phase inverter has $m^n$ space vectors, therefore a six-phase two-level VSI has $2^6$ i.e., 64 space vectors corresponding to the switching states. There are 60 active vectors and 4 null vectors. These 64 vectors form four 12-sided concentric polygons. Active vectors can be classified as largest, second largest, third largest and shortest vectors. Among 60 active vectors, 12 are the redundant vectors, which lie along the third largest vectors; therefore, third largest vectors can be synthesized by either of the two switching state combinations. Zero vectors are mapped to the origin. The fundamental component along with the harmonic of order k=6n$\pm$1 (n=1, 2, 3..) are mapped into the $d_1$-$q_1$ plane. These variables of $d_1$-$q_1$ plane are responsible for the revolving MMF and production of electromechanical energy. Harmonics of order k=12n$\pm$1 (n=1, 2, 3..) are mapped into the $d_2$-$q_2$ plane, the vectors triggered in this subspace only generates the harmonic currents, which contributes to the stator loss. Largest vectors of the $d_1$-$q_1$ plane are mapped as the shortest vectors in $d_2$-$q_2$ plane and vice-versa. Therefore, in order to minimize stator losses, SVPWM strategies utilize only the large vectors in $d_1$-$q_1$ plane. Classification of vectors in $d_1$-$q_1$ and $d_2$-$q_2$ planes can be observed in Figs. 3.4a and 3.4b respectively.

A space vector modulation scheme should satisfy some criteria such as switching frequency should be kept constant and unnecessary switching of converter should be avoided to restrain the switching losses. Complete utilization of the available DC bus voltage must be provided. Lower order harmonics in the output voltage must be minimized in order to obtain

the sinusoidal voltage to maximum level. Keeping these criteria in perspective, in the next sections, different SVPWM techniques are analyzed on the basis of current THD and torque pulsation.

### 3.5.1 Conventional SVPWM

Convention SVPWM is similar to that of a three-phase SVPWM. In this method, the reference vector is synthesized by utilizing two adjacent active vectors along with the null vector. Largest space vector of a six-phase VSI lies on the outer most 12-sided polygon. A sector is decided based on the presence of reference vector in $d-q$ plane. Space vectors are selected for synthesizing with respect to that sector. The $d-q$ plane is equally divided into 12 sectors each of 30 degrees as shown in Fig. 3.5a. If the reference vector is present on the first sector $v_{48}$ and $v_{49}$ are utilized. The switching time of the space vectors can be calculated as follows,

$$T_1 = 2\frac{|v^*|}{|V_l|}T_s sin\,(30-\theta) \tag{3.15a}$$

$$T_2 = 2\frac{|v^*|}{|V_l|}T_s sin\theta \tag{3.15b}$$

$$T_0 = T_s - T_1 - T_2 \tag{3.15c}$$

where, $|v^*|$ is the modulus of reference space vector, $|V_l|$ is the length of largest vector and $\frac{|v^*|}{|V_l|}$ is generally referred as modulation index $m_a$, a maximum value of modulation index operated in this method is 0.9659, which corresponds to phase voltage of $0.643V_{DC}$. In three-phase SVPWM, this phase voltage will be $0.577V_{DC}$. The rise in the voltage is due to the addition of harmonic components of order 6n$\pm$1, where n=1,3,5 etc.

### 3.5.2 Vector space decomposition SVPWM

Conventional SVPWM for ASIM is just an extension of three-phase SVPWM which under-utilizes the degree of freedom provided by six-phase. Vector space decomposition (VSD) for a six-phase VSI method was proposed by Zhao and Lipo in [70]. In this method, five space vectors are utilized for synthesizing the reference voltage vector, among which four are active vectors and one null vector. Active space vectors considered in this method are of largest magnitudes, which are adjacent to reference vector. $v_{56}$, $v_{48}$,$v_{49}$ and $v_{51}$ are the active space

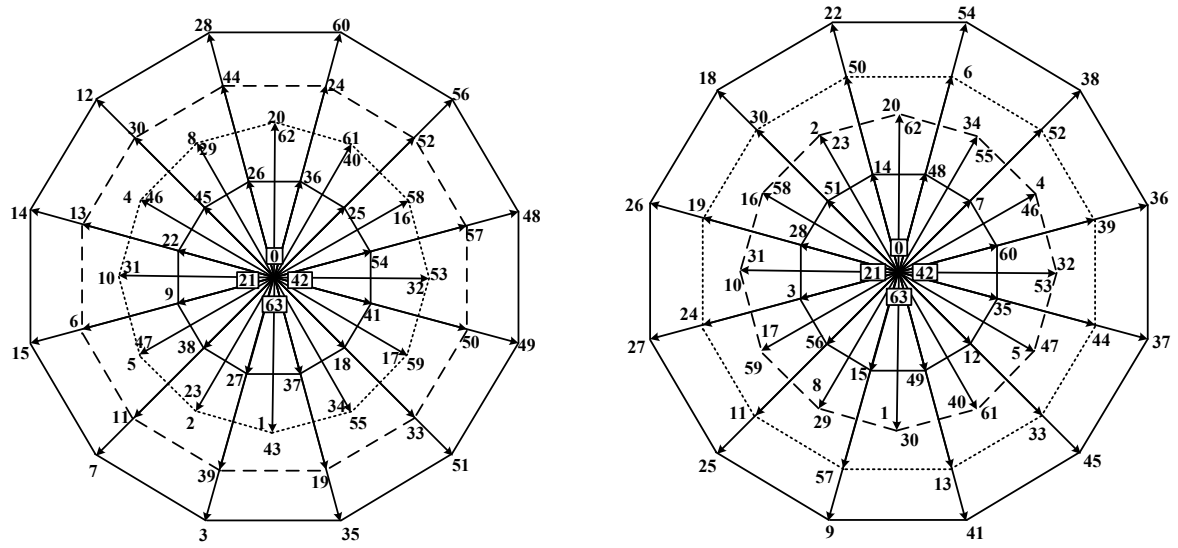

(a) (b)

Fig. 3.4: a) Voltage space vectors projected on $d_1$-$q_1$ plane, b) Voltage space vectors projected on $d_2$-$q_2$ plane.

vectors selected for sector I as shown in Fig. 3.5b. Vector switching times can be calculated by volt-second balance from the following equation.

$$T_1 v_{d_1}^1 + T_2 v_{d_1}^2 + T_3 v_{d_1}^3 + T_4 v_{d_1}^4 + T_0 v_{d_1}^5 = T_s v_{d_1}^* \tag{3.16a}$$

$$T_1 v_{q_1}^1 + T_2 v_{q_1}^2 + T_3 v_{q_1}^3 + T_4 v_{q_1}^4 + T_0 v_{q_1}^5 = T_s v_{q_1}^* \tag{3.16b}$$

$$T_1 v_{d_2}^1 + T_2 v_{d_2}^2 + T_3 v_{d_2}^3 + T_4 v_{d_2}^4 + T_0 v_{d_2}^5 = 0 \tag{3.16c}$$

$$T_1 v_{q_2}^1 + T_2 v_{q_2}^2 + T_3 v_{q_2}^3 + T_4 v_{q_2}^4 + T_0 v_{q_2}^5 = 0 \tag{3.16d}$$

$$T_s = T_1 + T_2 + T_3 + T_4 + T_0 \tag{3.16e}$$

where $d_1 - q_1$ and $d_2 - q_2$ subscripts denote the components of space vectors in particular plane. $v_1$ to $v_4$ indicates the four adjacent active space vectors and $v_5$ is the zero space vector. $T_0$ to $T_4$ are switching times of the corresponding space vectors. This PWM technique provides the maximum output voltage in $d_1 - q_1$ plane by keeping the $d_2 - q_2$ plane harmonics minimum. As lower order harmonics are not created, the maximum value of $m_a$ is 0.866 and the maximum phase voltage, which can be obtained by this method is $0.577V_{DC}$.

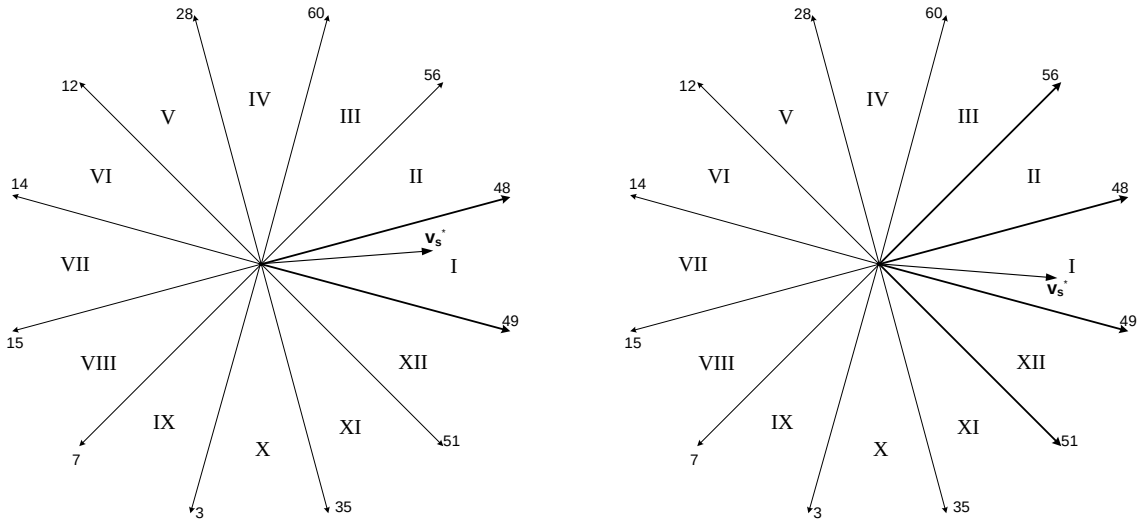


Fig. 3.5: a) Switching modes selected for conventional SVPWM, b)Switching modes selected for vector space decomposition SVPWM.

### 3.5.3 Vector classification SVPWM

Implementation of vector space decomposition method involves complex procedures as switching frames are mapped to the inverter frame rather than machine frame. A simple SVPWM termed as vector classification technique, where a six-phase VSI is considered as two three-phase VSIs for operation purpose was proposed by Bakhshai et al., in [71]. In this method, two identical three-phase SVPWM methods are utilized to generate the pulses for a six-phase VSI. The reference vector for second SVPWM is phase shifted by 30 electrical degrees as shown in Fig. 3.1. As two identical phase shifted SVPWM methods are used, output phase voltages are also phase shifted by 30 electrical degrees. Three-phase SVPWM equations can be applied for switching time calculation:

$$T_1 = \frac{2}{\sqrt{3}} m_a T_s sin\left(60 - \theta\right) \tag{3.17a}$$

$$T_1 = \frac{2}{\sqrt{3}} m_a T_s sin\theta \tag{3.17b}$$

$$T_0 = T_s - T_1 - T_2 \tag{3.17c}$$

where, $m_a = \frac{|v^*|}{|V_l|}$. When the reference space vector is phase shifted by 30 electrical degrees,

individual vectors will be added directly. Because of this, the maximum value of $m_a$, which can be achieved is 0.89655 and an equivalent phase voltage of $0.5977V_{DC}$.

### 3.5.4 Common mode voltage injection SVPWM

To avoid complexities of sector identification and to reduce the execution time, an advanced and efficient SVPWM by utilizing common mode voltage was proposed for a three-phase converter in [83]. Common mode voltage injection (CMVI) SVPWM implementation is independent of the magnitude of reference voltage and its relative angle w.r.t reference axis. This method utilizes the instantaneous values of reference voltages for the calculation of imaginary switching time, which is proportional to the reference signal. In a six-phase converter, that reference signal of two three-phases is phase shifted by thirty electrical degrees. For obtaining the modulation signal, a common mode voltage is to be added to the imaginary sampling time. Modified common mode voltage algorithm for asymmetrical six-phase induction machine can be written as;

$$T_{a1s} = \left[\frac{T_s}{V_{DC}}\right] V^*_{a1s} \tag{3.18a}$$

$$T_{b1s} = \left[\frac{T_s}{V_{DC}}\right] V^*_{b1s} \tag{3.18b}$$

$$T_{c1s} = \left[\frac{T_s}{V_{DC}}\right] V^*_{c1s} \tag{3.18c}$$

$$T_{a2s} = \left[\frac{T_s}{V_{DC}}\right] V^*_{a2s} \tag{3.18d}$$

$$T_{b2s} = \left[\frac{T_s}{V_{DC}}\right] V^*_{b2s} \tag{3.18e}$$

$$T_{c2s} = \left[\frac{T_s}{V_{DC}}\right] V^*_{c2s} \tag{3.18f}$$

where $V^*_{a1s}, V^*_{b1s}, V^*_{c1s}, V^*_{a2s}, V^*_{b2s}$ and $V^*_{c2s}$ are the reference phase voltages and $T_{a1s}, T_{b1s}, T_{c1s}, T_{a2s}, T_{b2s}$ and $T_{c2s}$ are the imaginary switching times proportional to instantaneous values of respective six-phase reference phase voltages.

The effective time periods are calculated as,

$$\begin{aligned} T_{max} &= max\left(T_{a1s}, T_{b1s}, T_{c1s}, T_{a2s}, T_{b2s}, T_{c2s}\right) \\ T_{min} &= min\left(T_{a1s}, T_{b1s}, T_{c1s}, T_{a2s}, T_{b2s}, T_{c2s}\right) \end{aligned} \tag{3.19}$$

$$T_{eff} = T_{max} - T_{min} \tag{3.20}$$

The common mode time period, which is added to convert the imaginary switching times into the actual switching time is given as;

$$T_{CM} = \frac{T_0}{2} - T_{min} \tag{3.21}$$

In which,

$$T_0 = T_S - T_{eff} \tag{3.22}$$

The actual switching times can be written as:

$$T_{ga1} = T_{a1s} + T_{CM} \tag{3.23a}$$

$$T_{gb1} = T_{b1s} + T_{CM} \tag{3.23b}$$

$$T_{gc1} = T_{c1s} + T_{CM} \tag{3.23c}$$

$$T_{ga2} = T_{a2s} + T_{CM} \tag{3.23d}$$

$$T_{gb2} = T_{b2s} + T_{CM} \tag{3.23e}$$

$$T_{gc2} = T_{c2s} + T_{CM} \tag{3.23f}$$

The gating signals generated are for 'OFF' sequence, for 'ON' sequence and can be obtained from,

$$T_{gON} = T_S - T_{gOFF} \tag{3.24}$$

The algorithm can be explained much easily by using the flow chart as shown in Fig 3.6.

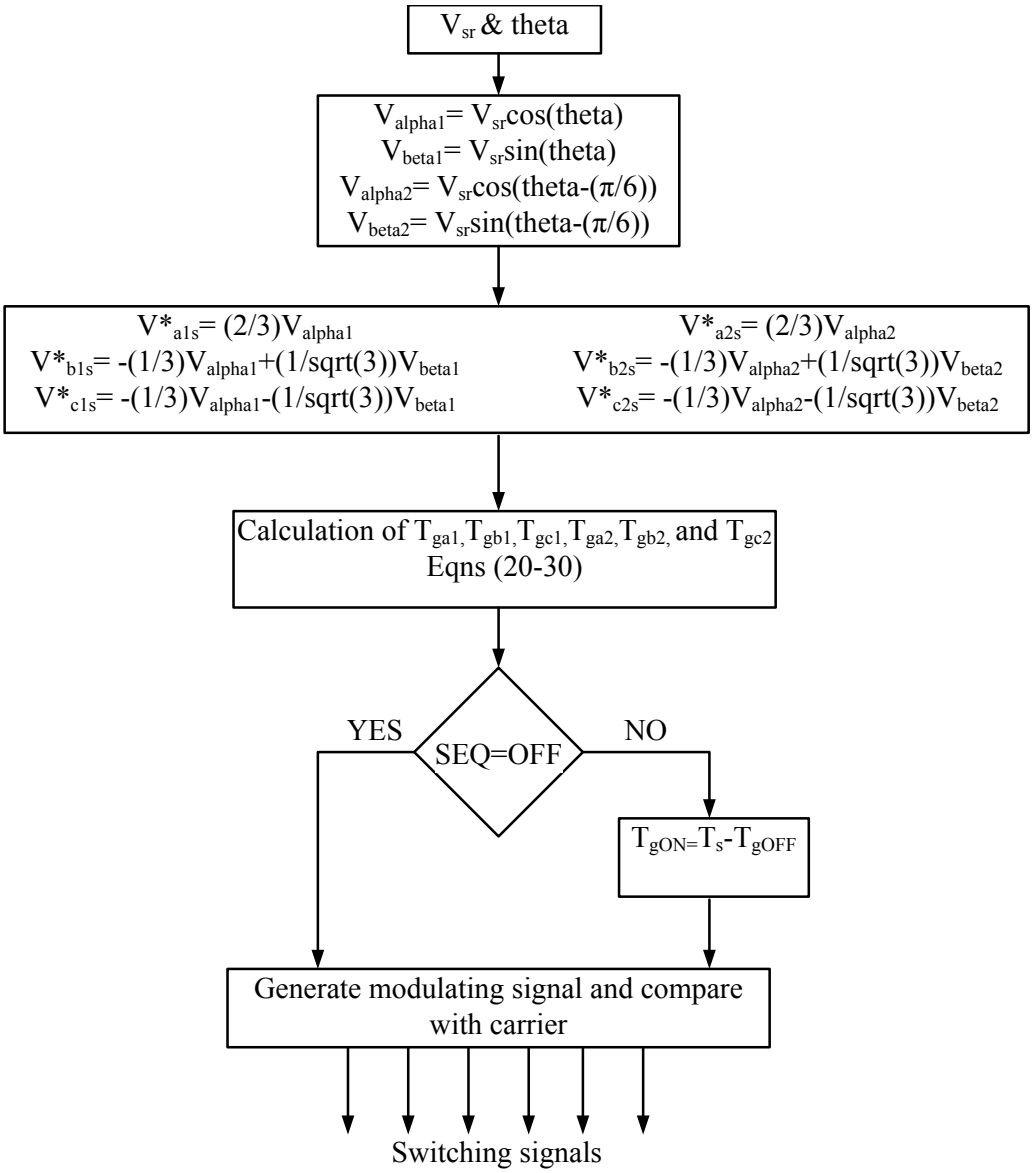


Fig. 3.6: The process flow chart of Common mode voltage injection SVPWM. $V_{alpha1}$, $V_{beta1}$, $V_{alpha2}$, and $V_{beta2}$ are the respective projections on stationary frame.

## 3.6 Indirect Rotor Field-Oriented control

Vector control was proposed by F. Blaschke in 1972 [84]. The main objective of vector control is to extract two decoupled current components from the available machine currents, by controlling which, independent control over torque and speed can be achieved. The same concept has been extended to multiphase drive with some modifications.

In indirect rotor field oriented control, the rotor flux is estimated from stator currents and rotor speed. The *d*-axis flux linkage is assumed to be aligned with the rotor flux-linkage vector $\lambda_r$, and *q*-axis flux-linkages are set to zero. By doing so, machine torque and flux can be controlled independently. While developing any control for a multiphase machine, power-sharing and unbalanced currents between the two three-phase sets should be considered. As this control independently operates both three-phase winding sets with six PI controllers, unbalanced currents are inherently eliminated.

Stator voltage equations from 3.1 in the arbitrary frame may be expressed as

$$\begin{aligned} v_{s1} &= i_{s1} r_s + j\omega_a \lambda_{s1} + p\lambda_{s1} \\ v_{s2} &= i_{s2} r_s + j\omega_a \lambda_{s2} + p\lambda_{s2} \\ v_r &= i_r r_r + j(\omega_a - \omega_r)\lambda_r + p\lambda_r \end{aligned} \tag{3.25}$$

Stator and rotor flux linkages from 3.2 may be expressed as

$$\begin{aligned} \lambda_{s1} &= \sigma L_s i_{s1} + (\sigma Ls - L_{ls}) i_{s2} + \frac{L_m}{L_r}\lambda r \\ \lambda_{s2} &= \sigma L_s i_{s2} + (\sigma Ls - L_{ls}) i_{s1} + \frac{L_m}{L_r}\lambda r \\ \lambda_r &= L_{lr} i_r + L'_m (i_{s1} + i_{s2} + i_r) \end{aligned} \tag{3.26}$$

where

$$\sigma = 1 - \frac{{L_m}^2}{L_s L_r}$$

### 3.6.1 Design of current controller

In vector control, the only variables to be controlled are stator current ($i_s$) and rotor flux ($\lambda_r$). Therefore, while designing a current controller, the stator flux ($\lambda_s$) and rotor current ($i_r$) are not supposed to be present in dynamic equation of the machine.

From equation 3.2 rotor flux linkage is re-written in terms of rotor current as

$$i_r = \frac{\lambda r}{L_r} - \frac{L_m}{L_r} i_{s1} - \frac{L_m}{L_r} i_{s2} \tag{3.27}$$

By introducing 3.26 and 3.27 in 3.25, the stator voltage equations can be rewritten as

$$\begin{aligned} V_{S1} = r_s \left[\frac{1+\tau_s(1-\sigma)}{\tau_r}\right] i_{s1} + \sigma L_s \frac{di_{s1}}{dt} + j\omega_a \sigma L_s i_{s1} + j\omega_a(\sigma L_s - L_{ls}) i_{s2} \\ + j\omega_a \frac{L_m}{L_r}\lambda_r + \frac{L_s(1-\sigma)}{\tau_r} i_{s2} - \frac{L_m}{L_r \tau_r}\lambda_r + (\sigma L_s - L_{ls})\frac{d}{dt} i_{s2} \end{aligned} \tag{3.28}$$

$$\begin{aligned} V_{S2} = r_s \left[\frac{1+\tau_s(1-\sigma)}{\tau_r}\right] i_{s2} + \sigma L_s \frac{di_{s2}}{dt} + j\omega_a \sigma L_s i_{s2} + j\omega_a(\sigma L_s - L_{ls}) i_{s1} \\ + j\omega_a \frac{L_m}{L_r}\lambda_r + \frac{L_s(1-\sigma)}{\tau_r} i_{s1} - \frac{L_m}{L_r \tau_r}\lambda_r + (\sigma L_s - L_{ls})\frac{d}{dt} i_{s1} \end{aligned} \tag{3.29}$$

where

$$\tau_s = \frac{L_s}{r_s}, \tau_r = \frac{L_r}{r_r}$$

Cross saturation coupling ($L_{ldq}$) and common mutual leakage inductance ($L_{lm}$) are disregarded only while designing the current regulator as their value will be negligible when difference between two three-phase sets is thirty degrees.

Independent control over generator torque and flux are achieved by decoupling $d-$ and $q - axis$ variables from each other. Dynamic voltage equations in their expanded form can be written as

$$V_{ds1} = r_s\left[\frac{1+\tau_s(1-\sigma)}{\tau_r}\right] i_{ds1} + \sigma L_s \frac{di_{ds1}}{dt} - \omega_a \sigma L_s i_{qs1} - \omega_a(\sigma L_s - L_{ls}) i_{qs2} + \frac{L_s(1-\sigma)}{\tau_r} i_{ds2} - \frac{L_m}{L_r \tau_r}\lambda_r + (\sigma L_s - L_{ls})\frac{d}{dt} i_{ds2} \tag{3.30a}$$

$$V_{qs1} = r_s\left[\frac{1+\tau_s(1-\sigma)}{\tau_r}\right] i_{qs1} + \sigma L_s \frac{di_{qs1}}{dt} + \omega_a \sigma L_s i_{ds1} + \omega_a(\sigma L_s - L_{ls}) i_{ds2} + \frac{L_s(1-\sigma)}{\tau_r} i_{qs2} + \omega_a \frac{L_m}{L_r}\lambda_r + (\sigma L_s - L_{ls})\frac{d}{dt} i_{qs2} \tag{3.30b}$$

$$V_{ds2} = r_s\left[\frac{1+\tau_s(1-\sigma)}{\tau_r}\right] i_{ds2} + \sigma L_s \frac{di_{ds2}}{dt} - \omega_a \sigma L_s i_{qs2} - \omega_a(\sigma L_s - L_{ls}) i_{qs1} + \frac{L_s(1-\sigma)}{\tau_r} i_{ds1} - \frac{L_m}{L_r \tau_r}\lambda_r + (\sigma L_s - L_{ls})\frac{d}{dt} i_{ds1} \tag{3.30c}$$

$$V_{qs2} = r_s\left[\frac{1+\tau_s(1-\sigma)}{\tau_r}\right] i_{qs2} + \sigma L_s \frac{di_{qs2}}{dt} + \omega_a \sigma L_s i_{ds2} + \omega_a(\sigma L_s - L_{ls}) i_{ds1} + \frac{L_s(1-\sigma)}{\tau_r} i_{qs1} + \omega_a \frac{L_m}{L_r}\lambda_r + (\sigma L_s - L_{ls})\frac{d}{dt} i_{qs1} \tag{3.30d}$$

In order to obtain a linear relation between voltage and current, the back-emf term $-\frac{L_m}{L_r \tau_r}\lambda_r$ needs to be eliminated. Moreover, the cross-coupling components ($d_2, q_1, q_2$ in equation 1 or $d_1, q_1, q_2$ in equation 2 and so on) are also not expected while designing the current controller. Therefore, feed-forward signals are introduced to eliminate the back-emf and cross-coupling terms during the current controller design, and it is expressed as

$$e_{ds1} = -\omega_a \sigma L_s i_{qs1} - \omega_a(\sigma L_s - L_{ls}) i_{qs2} + \frac{L_s(1-\sigma)}{\tau_r} i_{ds2} - \frac{L_m}{L_r \tau_r}\lambda_r + (\sigma L_s - L_{ls})\frac{d}{dt} i_{ds2} \tag{3.31a}$$

$$e_{qs1} = \omega_a \sigma L_s i_{ds1} + \omega_a(\sigma L_s - L_{ls}) i_{ds2} + \frac{L_s(1-\sigma)}{\tau_r} i_{qs2} + \omega_a \frac{L_m}{L_r}\lambda_r + (\sigma L_s - L_{ls})\frac{d}{dt} i_{qs2} \tag{3.31b}$$

$$e_{ds2} = -\omega_a \sigma L_s i_{qs2} - \omega_a(\sigma L_s - L_{ls}) i_{qs1} + \frac{L_s(1-\sigma)}{\tau_r} i_{ds1} - \frac{L_m}{L_r \tau_r}\lambda_r + (\sigma L_s - L_{ls})\frac{d}{dt} i_{ds1} \tag{3.31c}$$

$$e_{qs2} = \omega_a \sigma L_s i_{ds2} + \omega_a(\sigma L_s - L_{ls}) i_{ds1} + \frac{L_s(1-\sigma)}{\tau_r} i_{qs1} + \omega_a \frac{L_m}{L_r}\lambda_r + (\sigma L_s - L_{ls})\frac{d}{dt} i_{qs1} \tag{3.31d}$$

By substituting equations 3.31 in 3.30,

$$V_{ds1} = r'_s + L'_s \frac{di_{ds1}}{dt} + e_{ds1} \tag{3.32a}$$

$$V_{qs1} = r'_s + L'_s \frac{di_{qs1}}{dt} + e_{qs1} \tag{3.32b}$$

$$V_{ds2} = r'_s + L'_s \frac{di_{ds2}}{dt} + e_{ds2} \tag{3.32c}$$

$$V_{qs2} = r'_s + L'_s \frac{di_{qs2}}{dt} + e_{qs2} \tag{3.32d}$$

where

$$r'_s = r_s \left[ \frac{1 + \tau_s(1-\sigma)}{\tau_r} \right], \quad L'_s = \sigma L_s$$

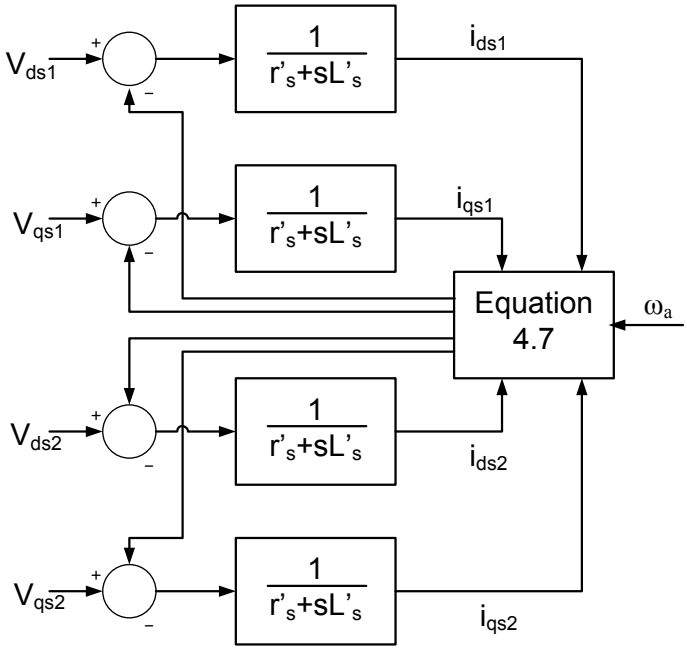


Fig. 3.7: Equivalent circuit of ASIM for designing current controller.

Active damping may also be included while designing the current controller. With active damping and feed-forward, the current control loop becomes a closed loop with unit feedback. The parameters of the PI controller can be calculated by comparing the bandwidth of current control loop with that of the PI regulator.

It is necessary to limit the maximum output voltage of current controller, and to achieve this, a voltage limiter is included while designing the current controller. With the inclusion

of voltage limiter, error between the reference and actual current might let the integrator to reach a very large value. The time required to reduce this error will be high and it may cause a considerable delay in the system. This can be reduced by introducing an anti-windup in the PI regulators.

### 3.6.2 Derivation of Indirect Field-Oriented Control

The phasor diagram shown in Fig. 3.8 can be used to explain the principles involved in indirect vector control. In IRFOC the induction machine will be represented in the synchronously rotating reference frame i.e., $\omega_a = \omega_e$. The rotor flux linkage $\lambda_r$ is assumed to be aligned with $d^e$ axis.

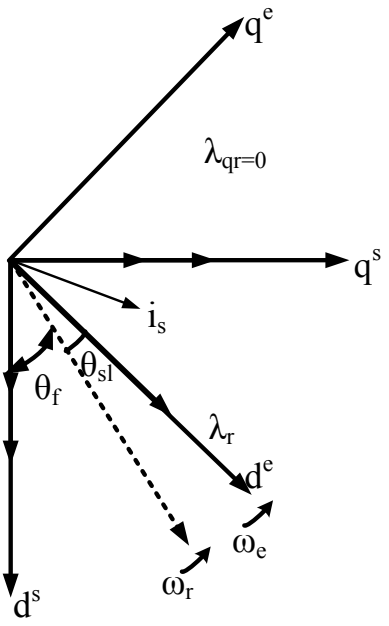


Fig. 3.8: Phasor diagram for indirect vector control.

The rotor voltage equations of ASIM in a synchronous frame of reference from 3.7 is given by

$$0 = r_r i_{qr} + (\omega_{sl})\lambda_{dr} + p\lambda_{qr} \tag{3.33a}$$

$$0 = r_r i_{dr} - (\omega_{sl})\lambda_{qr} + p\lambda_{dr} \tag{3.33b}$$

where

$$\omega_{sl} = \omega_e - \omega_r \tag{3.34a}$$

$$\lambda_{qr} = L_{lr} i_{qr} + L'_m (i_{q1} + i_{q2} + i_{qr}) \tag{3.34b}$$

$$\lambda_{dr} = L_{lr} i_{dr} + L'_m (i_{d1} + i_{d2} + i_{dr}) \tag{3.34c}$$

The $d$-axis flux linkage is assumed to be aligned with the rotor flux-linkage vector $\lambda_r$ and $q$-axis flux-linkages are set to zero. If the operation of field-weakening is not involved, the rotor flux $\lambda_r$ will be constant. However, if field-weakening is involved, the rotor rotor flux linkage is reduced for the same value of torque component of the current, the electromagnetic torque is reduced, and since the speed will increase constant power is obtained.

$$\begin{aligned} \lambda_r &= \lambda_{dr} \\ \lambda_{qr} &= 0 \\ p\lambda_r &= 0 \end{aligned} \tag{3.35}$$

By substituting 3.6.2 in 3.33, the new rotor equations can be formed as

$$r_r i_{qr} + (\omega_{sl})\lambda_r = 0 \tag{3.36a}$$

$$r_r i_{dr} - (\omega_{sl})\lambda_r = 0 \tag{3.36b}$$

The rotor currents can be rewritten in terms of stator currents as

$$i_{qr} = -\left(\frac{L_m}{L_r}\right) i_{q1} + i_{q2} \tag{3.37a}$$

$$i_{dr} = \left(\frac{\lambda_r}{L_r}\right) - \left(\frac{L_m}{L_r}\right) i_{d1} + i_{d2} \tag{3.37b}$$

By substituting 3.37 in 3.36, equation can be obtained as

$$i_f = \left(\frac{1}{L_m}\right) [1 + \tau_r p]\lambda_r \tag{3.38a}$$

$$\omega_{sl} = \left(\frac{L_m}{\tau_r}\right) \left(\frac{i_T}{\lambda_r}\right) \tag{3.38b}$$

where,

$$i_f = i_{d1} + i_{d2}, \qquad i_T = i_{q1} + i_{q2}, \qquad \tau_r = \frac{L_r}{r_r}$$

As *d*-axis current is responsible for the flux-production, it is renamed as $i_d$ and *q*-axis current is responsible for torque production, it is renamed as $i_T$. The electromagnetic torque can be given by,

$$T_e = K_e \lambda_r i_T \tag{3.39}$$

where,

$$K_e = \left(\frac{3}{2}\right)\left(\frac{P}{2}\right)\left(\frac{L_m}{L_r}\right) \tag{3.40}$$

### 3.6.3 Disturbance reduction feed-forward loop

The main objective of any control technique is to improve the system speed response, but a change in load torque will cause a sluggish reaction and affect the speed under closed-loop control. In order to avoid this kind of interference, a modification in the existing IRFOC is proposed by feed-forwarding load torque compensating current $i_{qL}$. However, load torque measurement is very difficult in real time, therefore a method to estimate the load torque from rotor speed, and electromechanical torque is discussed in this section. Using speed dynamic equations, load torque can be written as,

$$T_l = T_e - B\omega_r - J\frac{d\omega_r}{dt} \tag{3.41}$$

With a discrete time difference, aforementioned equation can be written as,

$$T_l(k) = T_e(k-1) - B\omega_r(k-1) - J\frac{\omega_r(k) - \omega_r(k-1)}{t_s} \tag{3.42}$$

By substituting for $T_e$ from equations (3.39) and (3.40), load torque can be rewritten as,

$$\begin{aligned} T_l(k) = K_e \cdot \lambda_r(k-1) \cdot i_T(k-1) - B\omega_r(k-1) \\ - J\frac{\omega_r(k) - \omega_r(k-1)}{t_s} \end{aligned} \tag{3.43}$$

Load torque compensating current $i_{qL}$ can be obtained by the following equation,

$$i_{qL} = \frac{2L_r}{PL_m\lambda_r} T_l(k) \qquad = G_1 T_l(k) \tag{3.44}$$

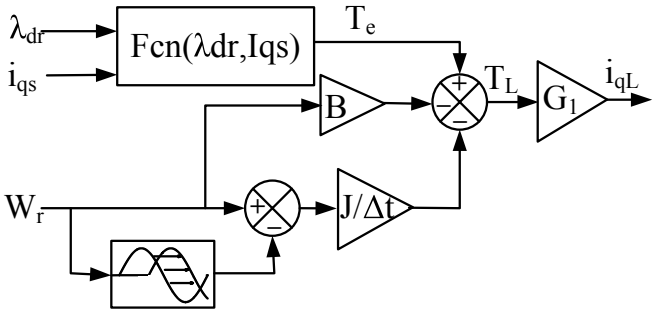


Fig. 3.9: Feed forwarding load torque as an equivalent q-axis current $i_{qL}$.

The effective sum of $i_{qs}$ and $i_{qL}$ are capable of compensating for the change in load torque and simultaneously maintain the desired speed demand too. Estimation of load torque compensating current $i_{qL}$ is shown in Fig. 3.9. Feed forwarding input load torque as an equivalent q-axis current in the current loop gives an effective improvement in speed response.

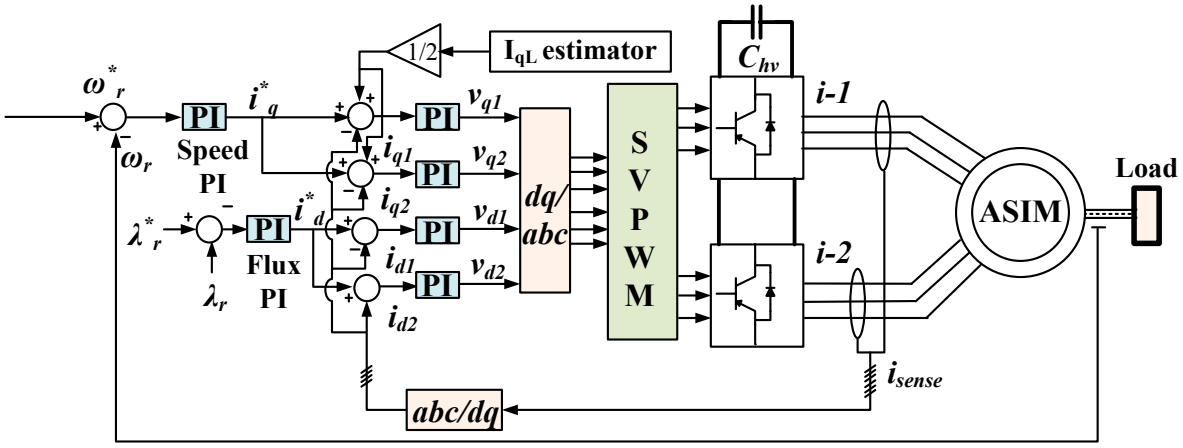


Fig. 3.10: Schematic diagram of ASIM with indirect rotor field-oriented control.

### 3.6.4 Implementation of Indirect Rotor Field-Oriented Control

The speed and flux requests are processed by the outer loop PI controllers that generate the command values of torque ($i_q^*$ ) and flux-producing ($i_d^*$) components of stator current. The commanded current values are further processed by four internal loop PI controllers to generate two sets of reference voltage vectors $v_{q1}, v_{d1}$ and $v_{q2}, v_{d2}$. These reference voltage vectors are used to generate two sets of three-phase reference voltage vectors. The two sets of voltage vectors generated are supplied as reference to SVPWM, which in order generates

the switching signals to base drive of the inverter switches. The schematic of indirect rotor field-oriented control for ASIM is depicted in Fig. 3.10.

It is worth to mention here that an asymmetrical six-phase machine can also be controlled by using only two PI controllers as described in [44]. In this, x-y reference voltages and currents are set to zero, causing asymmetries. To avoid this, the aforementioned control strategy uses the six PI controllers by developing a system transfer function of the entire drive.

## 3.7 Simulation results

Analysis of different SVPWM techniques for the voltage source converter supplied ASIM is performed with a series of modulation index values. The ASIM parameters (listed in the appendix) used in simulation are acquired from the laboratory prototype developed. The same switching frequency is maintained for all the SVPWM strategies. Average leg voltages, per phase RMS voltage and phase current waveforms for all the SVPWM techniques are presented. Total harmonic distortion, harmonic contents in the stator current is analyzed for different SVPWM techniques. The simulated waveforms for conventional SVPWM are presented in Fig. 3.11. In this method, two adjacent vectors of $d_1$-$q_1$ are utilized for synthesizing the space vector ,and the $d_2$-$q_2$ plane is uncontrolled, because of this considerable amount of fifth and seventh order harmonics can be observed in the stator current.

The simulation results of VSD SVPWM are shown in Fig. 3.12. In this technique, a null vector and four active vectors from the outermost polygon are selected to obtain the reference voltage; hence, decreasing the amplitude of $d_2$-$q_2$ vectors. This controlling of switching vectors in $d_2$-$q_2$ subspace decreases the harmonic content in phase current when compared to that of conventional SVPWM method.

Simulated waveforms of vector classification SVPWM technique is depicted in Fig. 3.13. In this case, a six-phase inverter is considered as two three-phase inverters sharing a common DC bus voltage. By doing this, complexities in the implementation of SVPWM can be decreased. Two adjacent active vectors and a null vector is selected individually for two three-phases, which in order decreases the lower order harmonics that can be observed in conventional SVPWM. Higher order harmonics can be observed in the phase voltage, but it

does not cause any effect on the system efficiency. The resulting six-phase space vector is an addition of three-phase space vectors, thus increasing the DC bus utilization.

Simulated waveforms of CMVI SVPWM technique is depicted in Fig. 3.14. This method does not involve any complicated procedures like sector identification or vector selection as in other SVPWM techniques. Phase current does not contain any 5th or 7th order harmonics; moreover, waveforms are similar to that of vector classification with decreased implementation time. Phase voltage contains the higher order harmonics, however, it does not affect the overall performance of the system.

IRFOC simulations are performed at a reference speed of 40 rad/s. A load torque of 5 N-m was applied at t=1 s. Drive performance is evaluated for the change in speed and change in load torque. Machine speed, electromagnetic torque, rotor flux, and stator currents for variation in the reference speed, and load torque are presented in Fig. 3.15. As it can be observed, machine speed is tracking reference speed very effectively, and it continues to do so even with the load torque variation. Simulated waveforms of $d-$ and $q-axis$ currents in synchronous frame of reference are exhibited in Fig. 3.16. Torque producing components of the machine, $i_{q1}$, and $i_{q2}$ are varying with the change in speed and load torque, whereas flux producing components $i_{d1}$, and $i_{d2}$ are maintained constant.

An extended view of drive speed, with and without feedforward control is presented in Fig. 3.17. From the simulated waveform, reduction in the disturbance can be observed with feed-forward control. Reduction of disturbance depends on the size and rating of the machine. As a machine considered in this analysis is a smaller one, observable variation is quite less, but for a high power machine, even a small reduction can benefit from a larger impact.

## 3.8 Experimental results

Experimental evaluation of the aforementioned SVPWM strategies is performed on a laboratory prototype detailed in Chapter 2.

ASIM is operated with conventional SVPWM technique. Obtained experimental results are exhibited in Figs. 3.18a and 3.18b, as it can be observed that the current waveform is not sinusoidal. The amplitude of pulsating torque is also increased. This is caused by the presence of lower order harmonics. Lower order harmonics can be reduced by utilizing more

vectors for synthesizing reference space vectors.

Experimental waveforms of phase current, phase voltage and steady-state torque with VSD SVPWM are presented in Figs. 3.19a and 3.19b respectively. As the number of active vectors for synthesizing reference space vector is increased in this method, improvement in the quality of current and torque can be clearly observed.

The vector classification method is implemented on ASIM drive and corresponding waveforms are shown in Figs. 3.20a and 3.20b. The recorded current waveform is sinusoidal and better than the classical SVPWM. Pulsating torque is also observed to be decreased, but when compared with vector space decomposition SVPWM, the amplitude of pulsating torque is increased. This is the result of arbitrary switching of active space vectors. As this method treats six-phase space vector as the combination of two three-phase vectors, control in selection of active space vector does not exist.

Finally, the modified common mode voltage injection SVPWM technique is implemented on ASIM drive, and corresponding results are presented in Figs. 3.21a and 3.21b. This method is an extension of three-phase common mode voltage injection SVPWM. Phase current is found to be sinusoidal and the amplitude of pulsating torque is lower than all other SVPWM techniques. Implementation is also easier as it does not involve any kind of sector identification, which is necessary for the remaining SVPWM technique.

## 3.9 Conclusion

This chapter discusses the detailed dynamic modeling of asymmetrical six-phase induction machine and six-phase PWM converter. Three-existing and proposed SVPWM techniques are analyzed in terms of current harmonics and torque pulsations. The performance of space vector PWM techniques on ASIM has been verified through simulation and hardware results. Phase voltages and currents recorded are found to be similar and in close agreement. Small disturbances and stepped waveforms observed in hardware results are due to the reduced sampling time. The observations noted from the simulation and experimental are emphasized as follows.

The conventional SVPWM method contains lower order harmonics in the phase current as only two active vectors are selected for synthesizing the reference voltage. These har-

monics are considerably large and increases the motor losses. Vector space decomposition approach practically eliminates the lower order harmonics, whereas implementation of it can be quite complex as computation of it either involves the inverse calculation of $5\times5$ matrix or contains a large look-up table. The vector classification and common mode voltage injection SVPWM methods almost have the same output results, which are very satisfactory in terms elimination of lower order harmonics; however, a slight increase in the amplitude of pulsating torque can be observed in vector classification SVPWM. This is because in VSD SVPWM harmonic current cancellation due to phase angle diversity and attenuation due to system impedance. In vector classification and CMVI SVPWM techniques, the volt-second balance of the $d_2$-$q_2$ plane inherently becomes zero, which is similar to VSD SVPWM. Implementation is simple and convenient in both methods. As CMVI SVPWM does not involve any sector identification or vector selection, it requires less computation time as compared to other methods. Vector space decomposition, vector classification, and CMVI SVPWM techniques offer reduced harmonics as observed in simulation and experimental results.

The outcome of comparative SVPWM analysis is utilized for developing a simple and very effective form of IRFOC. In this, both stator terminals are controlled as separate entities, and therefore unbalance current sharing observed in previous works is eliminated inherently. Simulation results are exhibited for verification. With an additional feed-forwarding loop injecting load torque equivalent q-axis current, improvement in speed response is observed. This feed-forwarding loop will be much more beneficial for the fault-tolerant operation of ASIM.

In the following chapters, indirect rotor field-oriented control is utilized for variable speed operation of grid-connected ASIG, and power electronic interface in PEVs. The experimental results of the ASIM with IRFOC are presented in accordance with these applications.

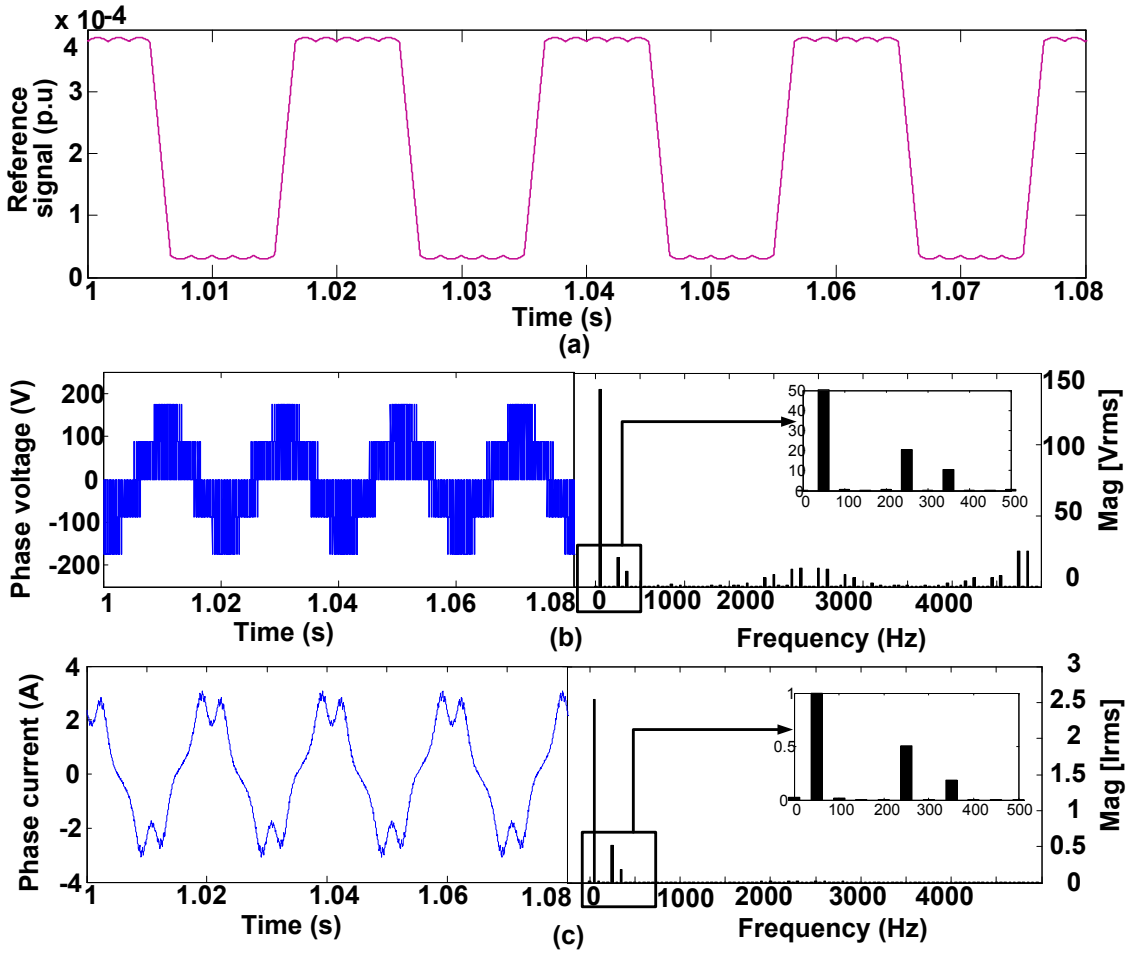


Fig. 3.11: Conventional SVPWM waveform. From top to bottom: Reference signal, phase voltage with frequency spectra, phase current with frequency spectra.

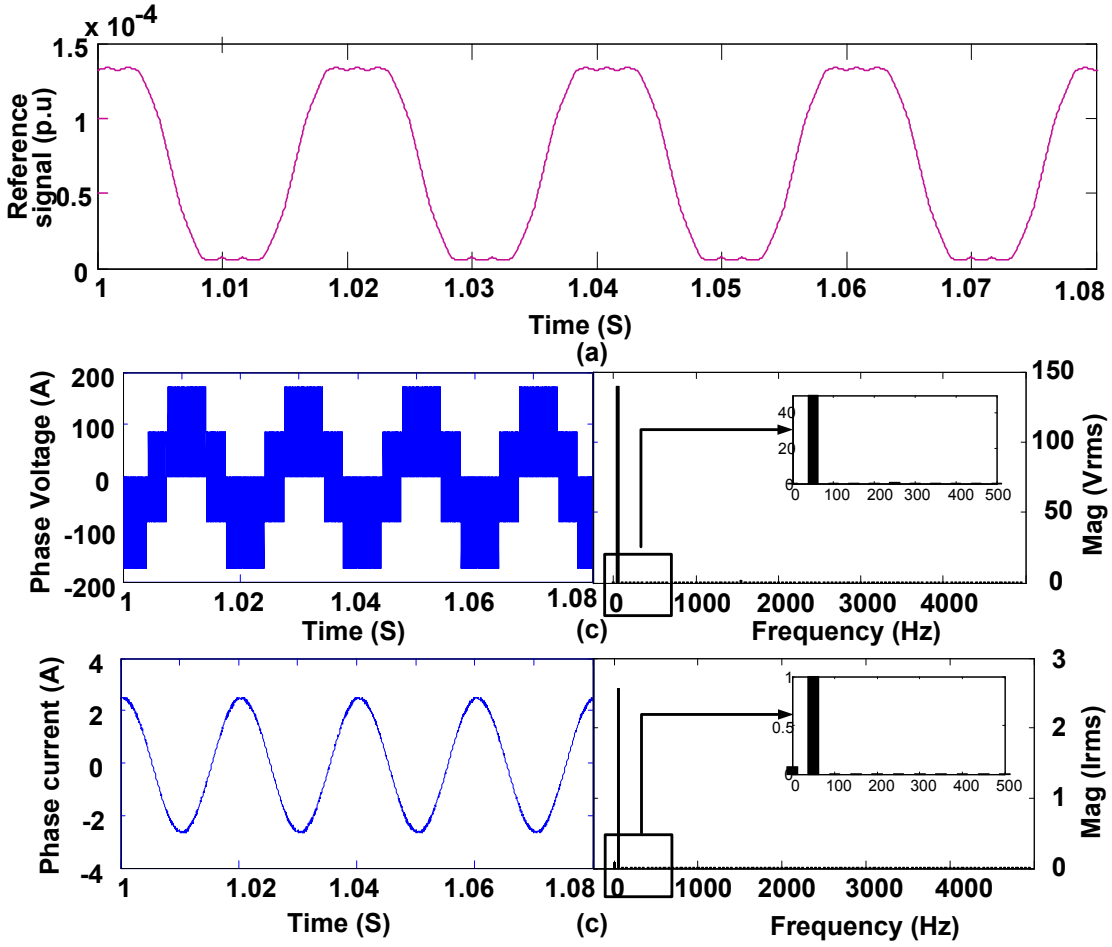


Fig. 3.12: VSD SVPWM waveform. From top to bottom: Reference signal, phase voltage with frequency spectra, phase current with frequency spectra.

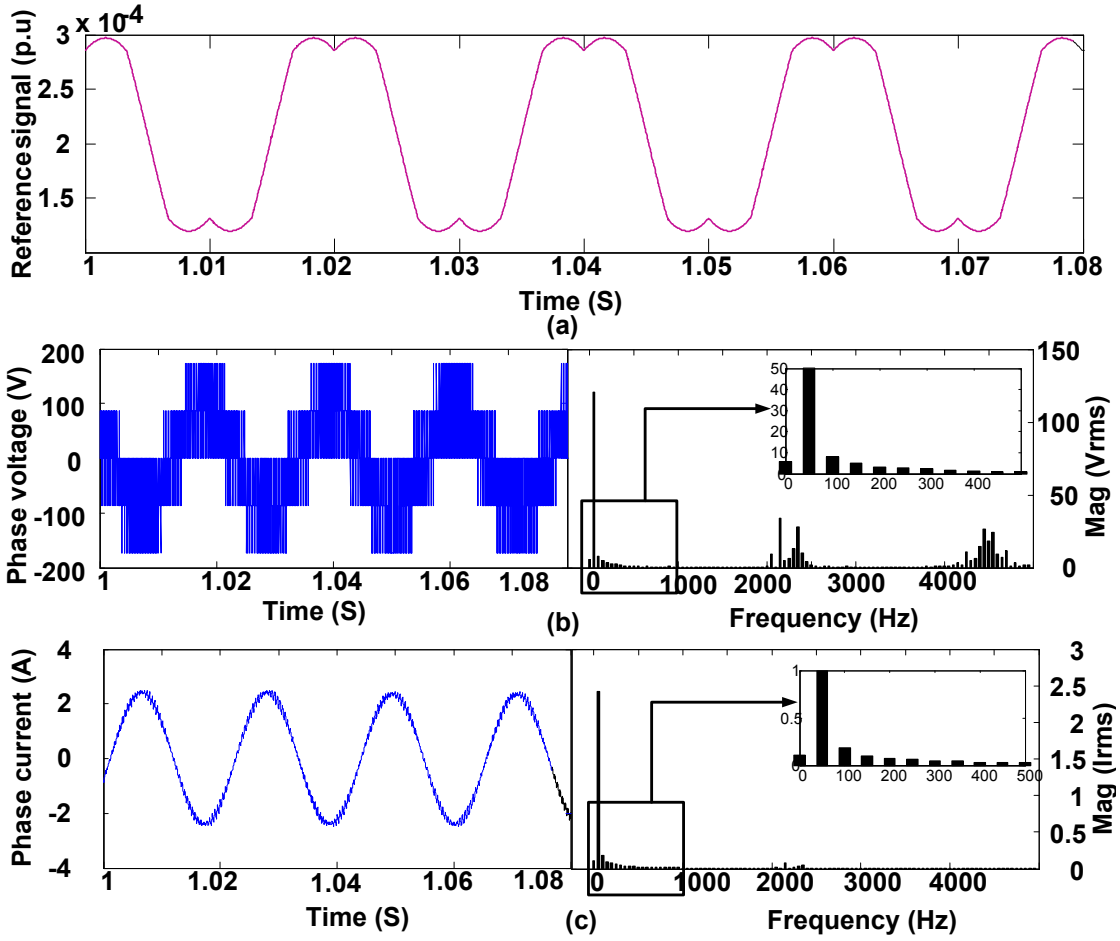


Fig. 3.13: Vector classification SVPWM waveform. From top to bottom: Reference signal, phase voltage with frequency spectra, phase current with frequency spectra.

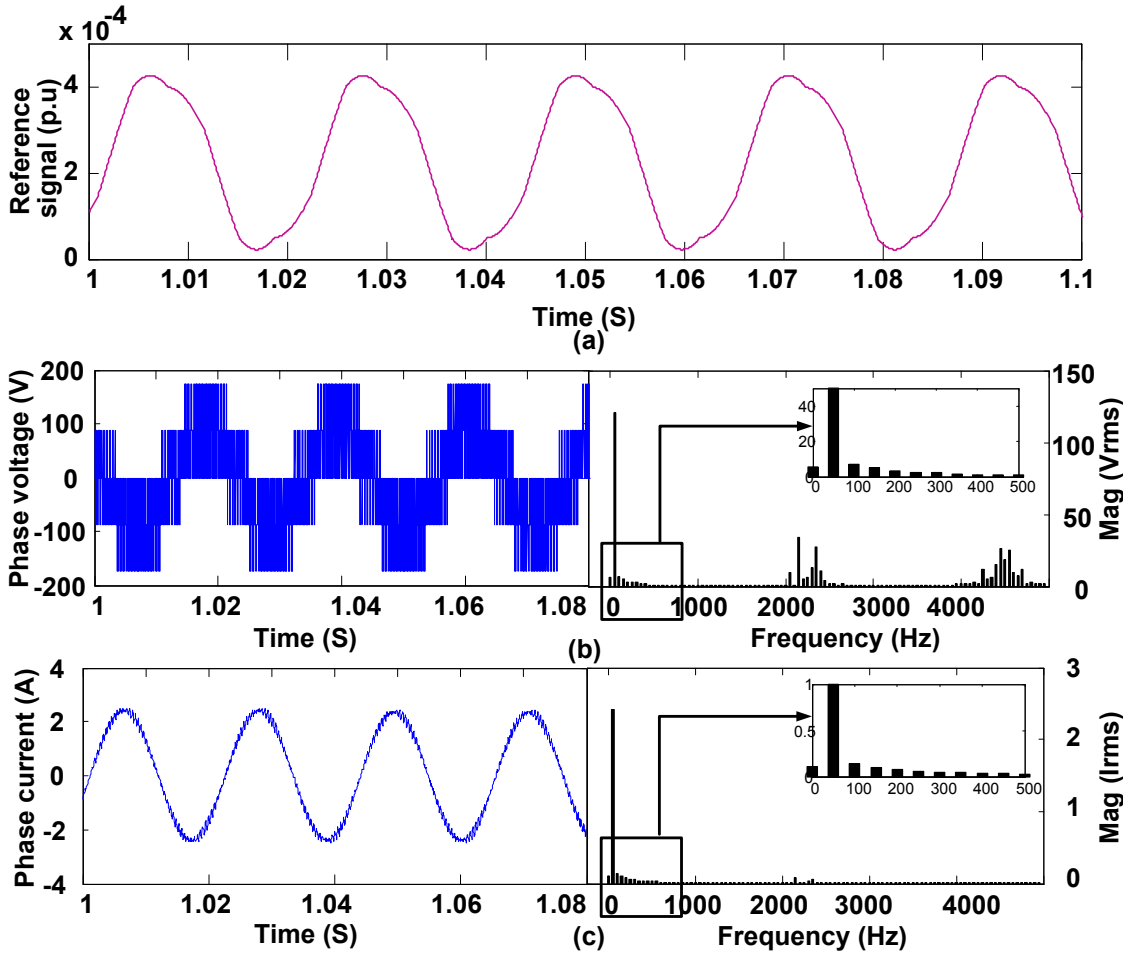


Fig. 3.14: CMVI SVPWM waveform. From top to bottom: Reference signal, phase voltage with frequency spectra, phase current with frequency spectra.

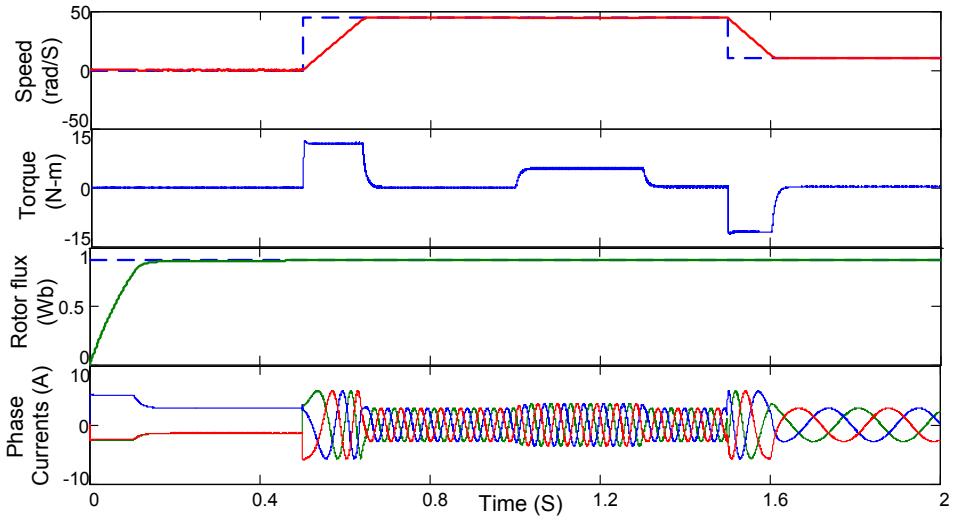


Fig. 3.15: Simulated waveforms of; speed, torque, rotor flux, and motor currents.

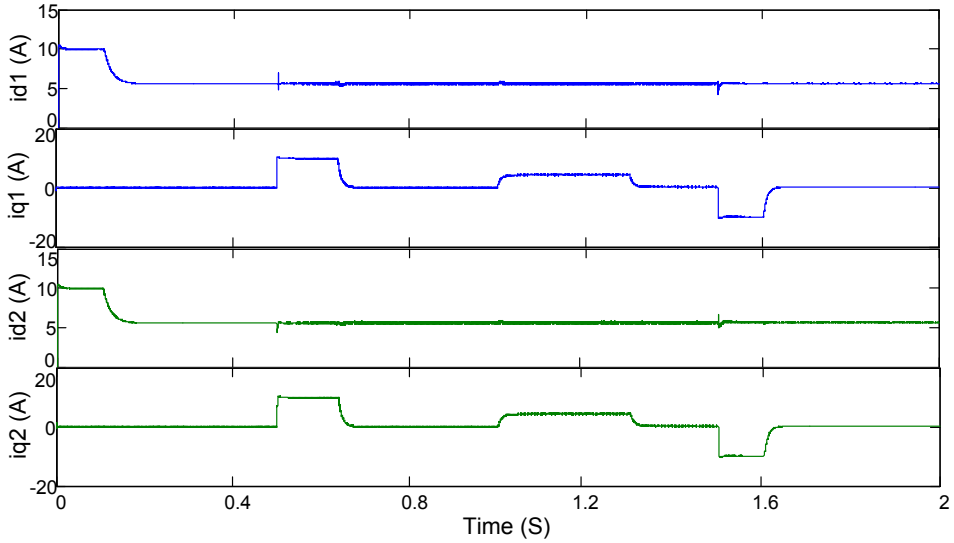


Fig. 3.16: Simulated waveforms of $q-$ and $d-axis$ currents in the synchronous frame of reference.

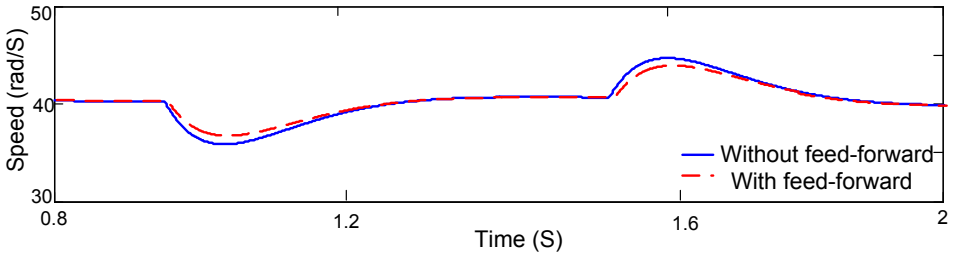


Fig. 3.17: Extended view of drive speed for change in load torque.

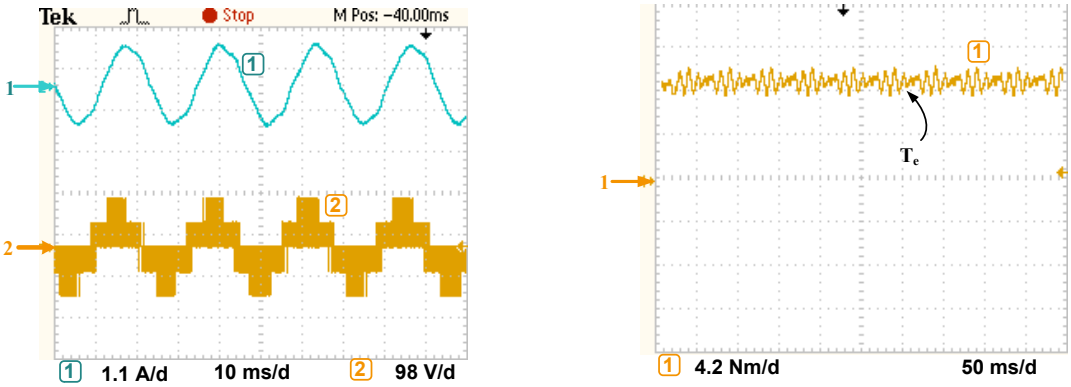


(a) (b)

Fig. 3.18: Experimental waveforms of conventional SVPWM: (a) CH1: Phase current, and CH2: phase voltage. (b) Steady-state torque ($T_e$).

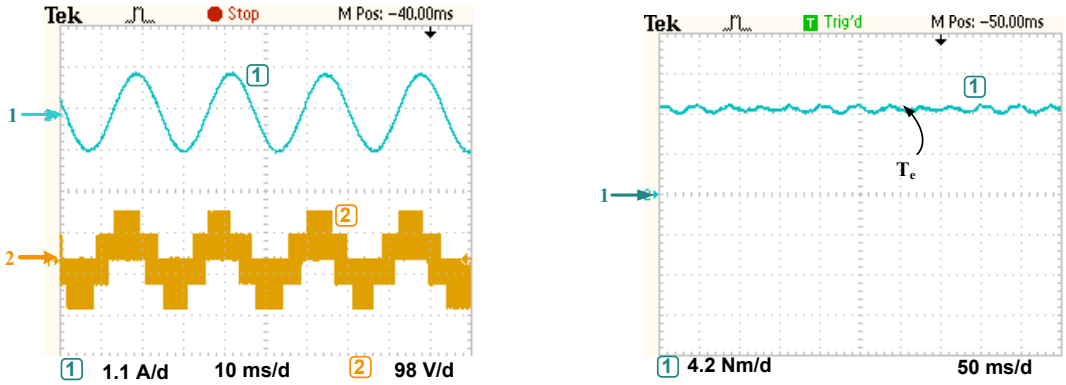


(a) (b)

Fig. 3.19: Experimental waveforms of vector space decomposition SVPWM: a) CH1: Phase current, and CH2: phase voltage. (b) Steady-state torque with VSD SVPWM ($T_e$).

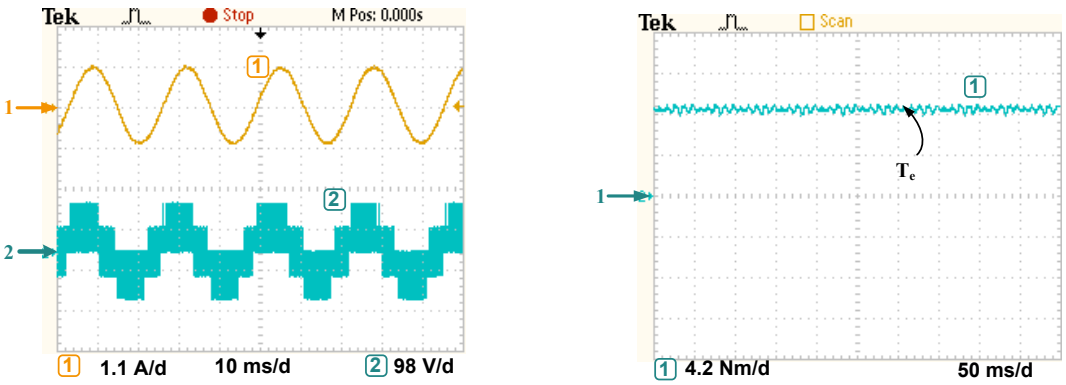


(a) (b)

Fig. 3.20: Experimental waveforms of vector classification SVPWM: (a) CH1: Phase current, and CH2: phase voltage. (b) Steady state torque ($T_e$).

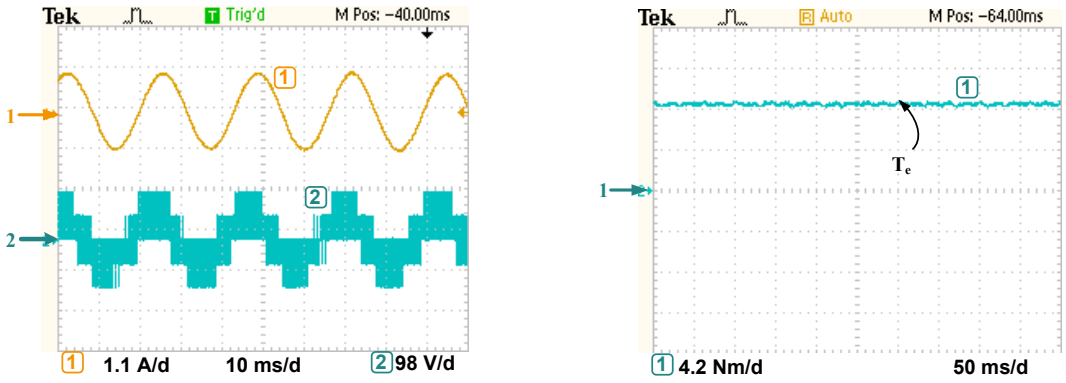


(a) (b)

Fig. 3.21: Experimental waveforms of common mode voltage injection SVPWM: (a) CH1: Phase current, and CH2: phase voltage. (b) Steady state torque ($T_e$).

# CHAPTER 4

# ASYMMETRICAL SIX-PHASE INDUCTION GENERATOR FOR WIND ENERGY APPLICATIONS

## 4.1 Introduction

Advantages of multiphase generators can be effectively utilized for wind power plants. Failure of one or two phases does not affect the generation drastically as compared to that of three-phase induction generators. Because of this, multiphase induction generators are being considered for self-excited and grid-connected power generation in both offshore and onshore wind power plants. Based on the operation, grid-connected induction generators can be classified into fixed speed and variable speed generators.

This chapter presents a detailed modeling and analysis of six-phase induction generator in variable speed WECS. Moreover, advantages of asymmetrical six-phase induction generator in stand-alone, and grid-connected fixed speed operation is also evaluated. Various aspects such as efficiency, reliability, and productivity are considered while performing the analysis.

Variable speed wind energy conversion utilizes the voltage source converters (VSC) connected in back to back with decoupled with DC-link capacitors. Because of decoupling between the grid and generator, it is not necessary to use the three-phase generators. On the other hand, utilizing multiphase machines can be beneficial for variable speed WECS. The objective of generator side converters is to extract maximum power by operating the generator at a certain optimum speed. The reference optimum speed is obtained from MPPT algorithm. ASIG is operated at this speed with rotor field-oriented control, which is detailed in the previous chapter. This chapter focuses on developing an MPPT algorithm, and modeling of grid side system consisting of a three-level converter, inductive filter, grid and DC-link. Grid side converter is responsible for maintaining the constant DC bus voltage and controlling the active and reactive power flow between the grid and generator. This is achieved by operating the PWM converter with grid vector-oriented control.

In fixed speed operation, a generator is directly connected to the grid through a transformer. Mechanical speed conversion is done by a multi-stage gearbox situated between the

turbine and generator.

Self-excited generators are completely isolated from the grid and requirement of reactive power will be rendered either by capacitors or converters. Whereas, as the term suggests, grid-connected induction generators are interfaced with the utility grid.

## 4.2 ASIG for Variable speed WECS

Variable speed wind energy conversion system shown in Fig. 4.1 consists of a wind turbine driving ASIG connected to the grid through a full scale back to back converter. Two three-phase, two-level converters are connected across the generator side, and grid side consists of a single three-phase three-level converter. Both converters share a common DC-link in between. All the converters are IGBT based and voltage source operated. Vector space decomposition SVPWM is used for switching of converters. Machine side converter controls the generator for variable speed operation by using rotor field oriented control. Reference speed is obtained from MPPT to operate the generator at optimum speed, thereby extracting maximum power from the wind. It also supplies magnetizing current for the induction generator, consequently eliminating the need for excitation capacitors. The power generated by ASIG is fed from the machine side converter to grid side converter. PWM converter on grid side controls the active and reactive power flow independently by orienting the reference frame according to voltage vector of the supply grid. It also maintains the DC bus voltage constant. Generally, unity power factor operation is performed, in which reactive power is kept zero. A coupling inductor is connected between the grid and converter which filters the high-frequency ripples generated from converter switching. An isolation transformer is used while grid interfacing, and by doing so fault transmission between the grid and WECS can be avoided.

### 4.2.1 Wind turbine optimization.

Maximum power can be extracted at different wind speeds by operating the generator at an optimum speed. This can be achieved by adjusting the power coefficient ($C_p$) depending on the aerodynamic conditions. Different MPPT methods can be found for variable speed WECS, among those one method is based on the power-speed curve of wind turbine. In this method, maximum power, which can be obtained at different wind speeds for the particular

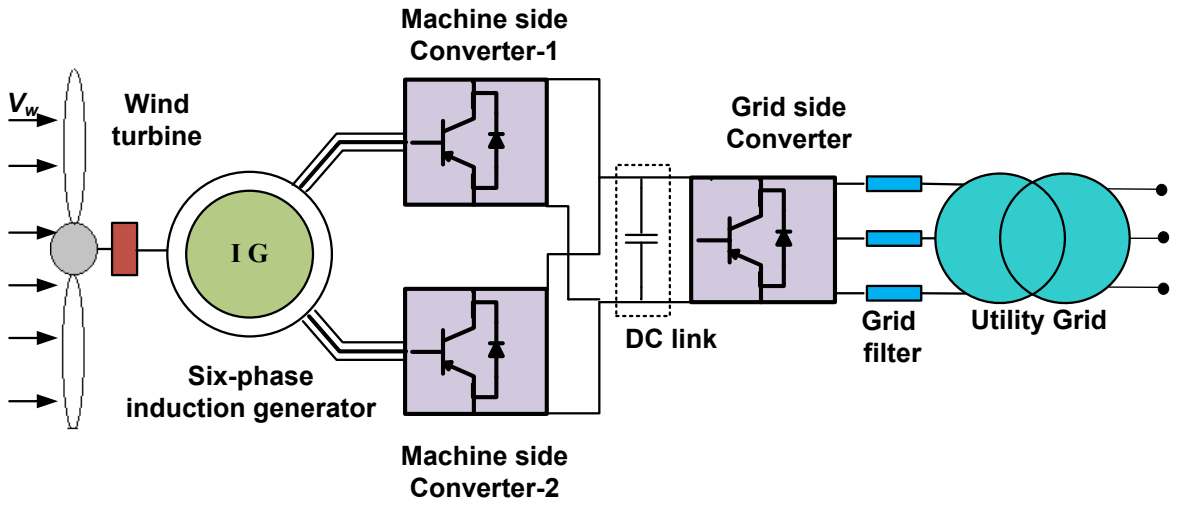


Fig. 4.1: Schematic of the proposed system.

wind turbine is calculated, and a curve is plotted with respect to the speed of wind turbine. A locus of a point can be tracked for different wind speeds, and a differential equation $K_{eq}$ is obtained for a particular turbine. In real time, the wind speed is measured by using a wind speed sensor or an anemometer. According to plotted MPPT profile, the speed reference $\omega_m^*$ is generated and provided to the generator control system that compares the speed reference with the speed measured from generator $\omega_g$ to produce control signals for the power converters to achieve maximum power operation.

The relationship between the wind speed and power captured by the turbine blade to convert it into mechanical energy can be described as follows [85],

$$P_M = \frac{1}{2}\pi\rho R^2 v^3 C_P(\lambda, \beta) \tag{4.1}$$

where, $P_M$ is the mechanical power extracted by turbine blades, $R$ is the radius of wind turbine, $\rho$ is the air density, $v$ is the velocity of wind and $C_p$ is the power coefficient of blade and is a function of tip speed ratio $\lambda$ and blade pitch angle $\beta$. $C_p$ can be approximated by using,

$$C_P(\lambda, \beta) = C_1 \left[\frac{C_2}{\lambda_i} - (C_3 + C_4)\beta - C_5\right] e^{\frac{-C_6}{\lambda_i}} \tag{4.2}$$

with

$$\frac{1}{\lambda_i} = \frac{1}{\lambda + 0.08\beta} - \frac{0.0365}{\beta^3 + 1} \tag{4.3}$$

$C_1$- $C_6$ values are chosen from the blade element momentum [86].

Tip speed ratio $\lambda$ can be defined as,

$$\lambda = \frac{\omega_t R}{v} \tag{4.4}$$

For a fixed pitch rotor, $\beta$ is set to zero, therefore $C_p$ is a function of $\lambda$. For particular wind speed, there is only one optimal point, where $C_p$ is maximum. Maximum power can be extracted from the wind if the turbine is continuously operated with maximum $C_p$. Optimum tip speed ratio for different wind speeds ranging from 6 m/s to 14 m/s has been plotted in Fig. 4.2. This $\lambda_{opt}$ line is converted into a function to obtain the optimum turbine speed $\omega_t^*$. Further, optimum generator speed $\omega_m^*$, which is given as reference to IRFOC is obtained from,

$$\omega_m^* = G\omega_t^* \tag{4.5}$$

where, G represents a multiplier gain or gear ratio.

The grid-connected ASIG system consits of ASIM drive, grid side VSC and an inductive filter connected between the grid and VSC. A simplified model of the grid side system is shown in Fig. 4.3.

### 4.2.2 Model of three-level grid side NPC Converter.

Multilevel converters can be availed to achieve higher voltage levels in order to improve the performance and quality of output power and voltage. Three-level neutral point clamped converter (NPC) consists of twelve IGBT switches and six independent diodes. All the IGBT switches are connected with anti-parallel diodes for bidirectional operation. Output voltage waveforms ($v_{ao}$, $v_{bo}$, $v_{co}$) generated by NPC converter comprises of three switching levels of amplitude $V_{DC}/2$ (0, $V_{DC}/2$, $V_{DC}$). The output phase voltage of the converter with respect to point 'O' can be express as follows [87],

$$v_{ao} = S_{a1}V_{C1} + S_{a2}V_{C2} \tag{4.6}$$

$$v_{ao} = S_{a1}V_{C1} + S_{a2}V_{C2} \tag{4.7}$$

$$v_{ao} = S_{a1}V_{C1} + S_{a2}V_{C2} \tag{4.8}$$

$V_{C1}$ and $V_{C2}$ are the voltages across capacitor $C_1$ and $C_2$ respectively Output AC voltages can be realized by combining equations (4.6)-(4.8) as,

$$v_{an} = \frac{V_{C1}}{3}(2S_{a1} - S_{b1} - S_{c1}) + \frac{V_{C2}}{3}(2S_{a2} - S_{b2} - S_{c2}) \tag{4.9}$$

$$v_{bn} = \frac{V_{C1}}{3}(2S_{b1} - S_{a1} - S_{c1}) + \frac{V_{C2}}{3}(2S_{b2} - S_{a2} - S_{c2}) \tag{4.10}$$

$$v_{cn} = \frac{V_{C1}}{3}(2S_{c1} - S_{b1} - S_{a1}) + \frac{V_{C2}}{3}(2S_{c2} - S_{b2} - S_{a2}) \tag{4.11}$$

### 4.2.3 Model of the grid, inductive filter, DC link.

The grid is modeled as an ideal three-phase balanced voltage source. An inductive filter is located between the NPC converter and grid. Output AC voltages of the converters with respect to neutral points are denoted as $v_{an}, v_{bn}$ and $v_{cn}$. Grid voltages are mentioned as $v_{az}, v_{bz}$ and $v_{cz}$.

Equations for steady-state converter output voltages in terms of grid can be written as,

$$v_{an} = R_i i_{az} + L_i \frac{di_{az}}{dt} + v_{az} \tag{4.12}$$

$$v_{an} = R_i i_{bz} + L_i \frac{di_{bz}}{dt} + v_{bz} \tag{4.13}$$

$$v_{an} = R_i i_{cz} + L_i \frac{di_{cz}}{dt} + v_{cz} \tag{4.14}$$

where, $R_i$ is the resistance of grid filter, $L_i$ is the inductance of grid filter and $i_{az}, i_{bz}, i_{cz}$ are the currents flowing through NPC converter's output. For grid side control, dynamic modeling is required. Grid equations, by decoupling into *d-q* components, can be written as,

$$v_{dn} = R_i i_{dz} + L_i \frac{di_{dz}}{dt} + vdz - \omega_a L_i iqz \tag{4.15}$$

$$v_{qn} = R_i i_{qz} + L_i \frac{di_{qz}}{dt} + vqz - \omega_a L_i idz \tag{4.16}$$

$\omega_a$ is the angular position in arbitrary frame of reference.

Combination of several capacitors between the grid side converter and generator side converter is referred as DC link or DC bus. The voltage across DC link depends on the currents flowing through the capacitor $i_c$, a simplified model of DC bus is shown in 4.4, voltage and current of DC bus capacitor can be expressed as

$$V_{DC} = \frac{1}{C_{DC}} \int i_c dt \tag{4.17}$$

$$i_c = i_{gdc} - i_{zdc} - i_R \tag{4.18}$$

where, $C_{DC}$ is the DC link capacitance, $i_c$ is the current through DC link capacitor, $i_{gdc}$ is the DC current flowing from DC bus to grid side converter, $i_{zdc}$ is the DC current flowing from generator side converter to DC bus and $i_R$ is the current through DC bus resistance.

### 4.2.4 Sizing of DC-link capacitor and grid filter

For real-time implementation, the DC link capacitor value is selected on the basis of the worst case current stress on the capacitor. The output current of the inverter is assumed to be sinusoidal. Variations in the capacitor RMS current $(I_{CRMS})$ with modulation index $(m_a)$ as well as line side power factor as correlated by the following expression is utilized and accordingly sizing of the DC link capacitor is performed [88].

$$I_{CRMS} = \sqrt{\frac{3I_N^2 m_a}{4\pi}\left[\sqrt{3} + cos(2\phi)\left[\frac{2}{\sqrt{3}}\right]\right] - \frac{9}{16}(I_n m_a)^2 cos^2(\phi)} \tag{4.19}$$

where $I_N$ is the amplitude of the output current, $\phi$ is the power factor angle and $m_a$ is the modulation index.

L-filter removes the current harmonics from the grid side converter. It is sized for 5% ripple in output current of the inverter using the expression

$$L_f = \frac{\left[\frac{\sqrt{3}}{2}\right] m_a V_{DC}}{6 f_s I_{rpl}} \tag{4.20}$$

where, $m_a$ is the modulation Index, $I_{rpl}$ is the allowed ripple current, $f_s$ is the switching frequency. This work considers 5 mH inductive filters between the grid side converter and grid and two capacitors of 6800 $\mu$F in series for DC-link.

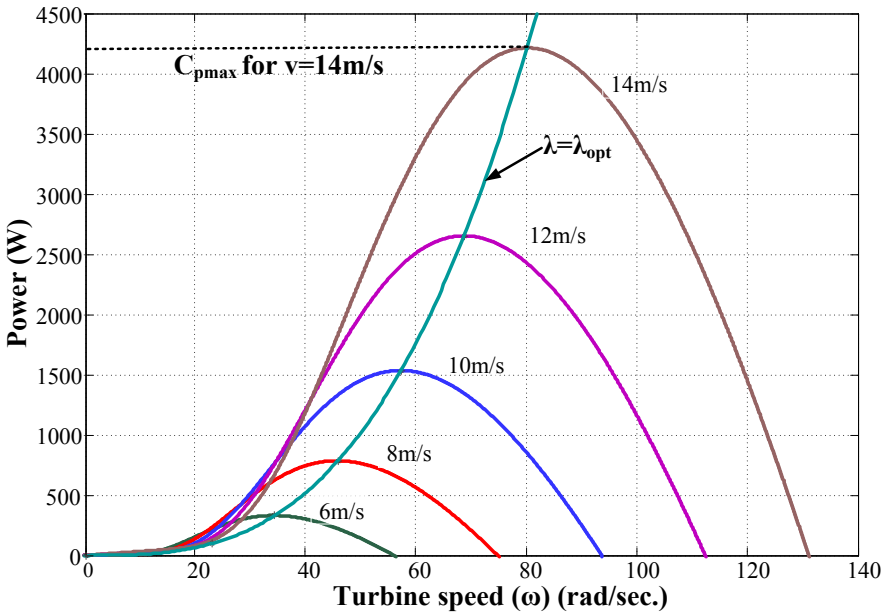


Fig. 4.2: Optimum operating characteristics of the turbine.

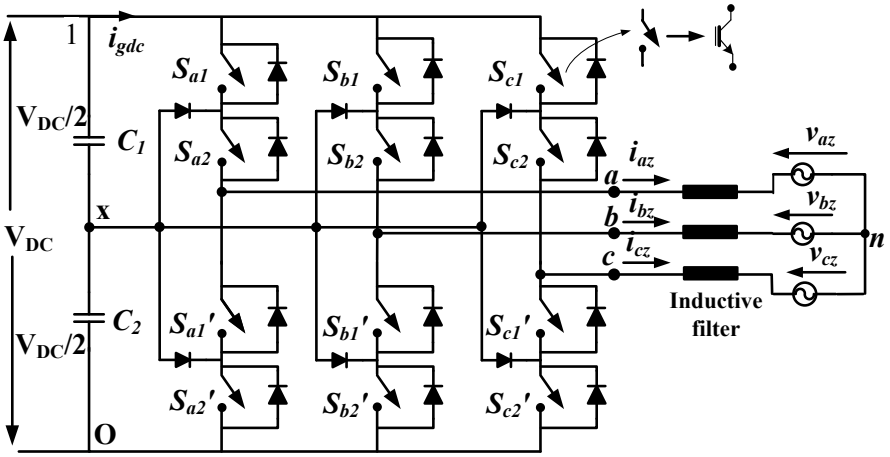


Fig. 4.3: Simplified model of the converter, filter and grid.

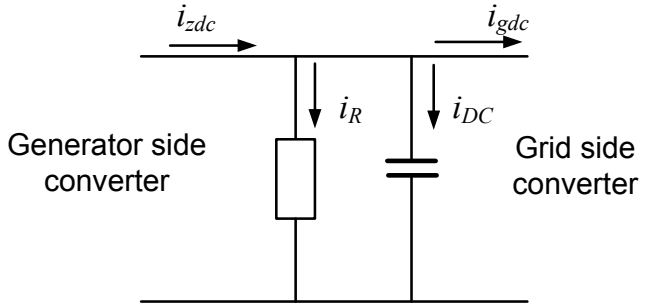


Fig. 4.4: Simplified DC bus system

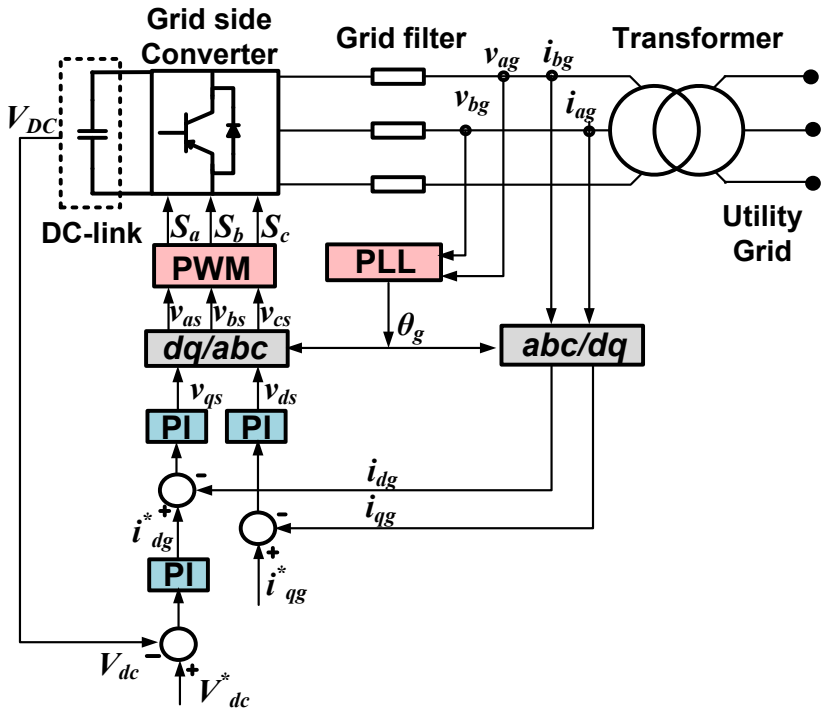


Fig. 4.5: Schematic diagram of grid-side control.

### 4.2.5 Grid vector-oriented control.

In order to achieve a controlled active and reactive power exchange between the grid and converter, it is necessary to control the grid side converter (GSC). GSC can be controlled with different schemes. In this work, vector oriented control (VOC) is utilized for this purpose. To achieve this, $d$-axis of the synchronous frame is aligned with the supply voltage vector. Active and reactive power can be calculated by the following equations [85],

$$\begin{aligned} v_g &= \sqrt{{v_q}^2 + {v_d}^2} \\ P_g &= \frac{3}{2}(v_d i_d + v_q i_q) \\ Q_g &= \frac{3}{2}(v_q i_d - v_d i_q) \end{aligned} \tag{4.21}$$

In VOC, $v_d = v_g$ and $v_q = 0$ therefore,

$$\begin{aligned} P_g &= \frac{3}{2} v_d i_d \\ Q_g &= -\frac{3}{2} v_d i_q \end{aligned} \tag{4.22}$$

The $q$-axis reference current $i_q^*$ can be obtained from,

$$i_q^* = \frac{-2Q_g^*}{3v_d} \tag{4.23}$$

where, $Q_g^*$ is the reference reactive power, and for unity power factor operation, this can be set to zero. Active power must flow through the DC bus to be transmitted to the grid. Therefore, only by maintaining the constant $V_D C$, this active power flow through the converters is ensured. The error between the actual and reference DC voltage is provided to PI controller. This PI controller generates $i_d^*$ according to operating conditions. The control strategy is shown in Fig. 4.5. DC bus voltage $v_{dc}$ is kept constant throughout the operation. Grid side converter operates both as a rectifier and inverter based on the direction of power flow.

## 4.3 Self-excited ASIG

Improved reliability and higher efficiency offered by the multiphase induction machine can be utilized effectively for stand-alone power generation. Voltage build-up process in an induction generator is similar to that of a DC generator. Per phase equivalent circuit of asymmetrical six-phase induction generator in self-excited and grid-connected mode under load condition is exhibited in Fig. 4.6 The "f" and "v" parameters in self-excited mode denote frequency and rotor speed respectively. Rotor speed "v" is fixed but "f" varies with the load and excitation capacitor.

Capacitor banks are connected across the stator terminals to provide lagging magnetizing reactive power, which is necessary for air gap flux establishment in the machine. Self-excitation can be achieved in an asymmetrical or symmetrical six-phase induction machine either by connecting the three-phase capacitor banks (delta or star) to one of the three-phase winding sets or to both the three-phase sets. For both the configurations, values can be determined analytically, or experimentally through 'synchronous speed test' [18]. The selected capacitor should be capable of maintaining the magnetizing current in the nonlinear portion. A minimum value of excitation capacitor (per phase) required to be connected to both three-phase sets to maintain sufficient self-excitation under steady state can be calculated

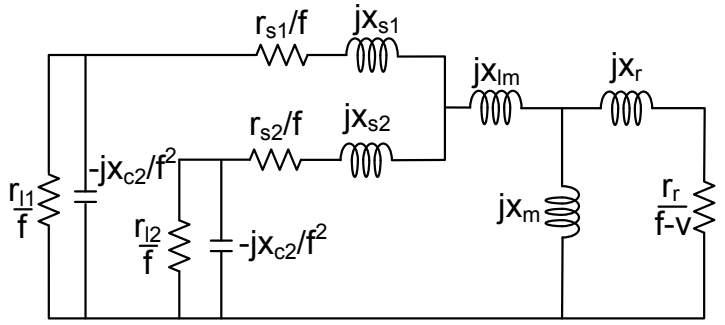


Fig. 4.6: Per phase equivalent circuit of asymmetrical six-phase induction generator under load condition in self-excited mode.

analytically as follows [89].

$$C_{min} = \frac{1}{(\omega)^2 v^2 (L_{ls} + L_{lm})} \tag{4.24}$$

where, $\omega$ is the angular frequency, $v$ is the operating speed of ASIG in per unit, and $L_{ls}$ and $L_m$ are leakage and stator magnetizing inductance of the generator.

However, the value of capacitor determined from this equation is just sufficient to have self-excitation under steady state only. Under transient conditions, the excitation process is also affected by the machine acceleration. To achieve better performance under loading condition, it becomes necessary to optimize the value of shunt and series capacitance. The value of shunt capacitance at a given speed to generate a desired no-load terminal voltage can be obtained experimentally by using a variable capacitor bank. For optimal performance, the value of shunt/excitation capacitance has to be from the values that will give no-load voltage lower than 1.0 p.u. Hence, for the purpose of analysis, a range of shunt capacitance value can be selected that will give the no-load terminal voltage in the range of 0.9 -1.0 p.u.

ASIG is driven by a prime mover, shunt capacitor banks of 25$\mu$F are connected with both the three-phase winding sets. The output of two three-phase sets ($abc$ and $xyz$) are integrated through a $\Delta$/Y-Y six-phase to three-phase, three winding transformer and supplied to a variable resistive load. The utilization of a six-phase generator to supply a three-phase load is shown in Fig. 4.7a. Magnetizing characteristics of self-excited ASIG is shown in Fig 4.7b. In this, the reliability of the system is improved, because a continuous supply to load is provided even when there is a failure in one of the two three-phase winding sets.

Reliability of this system is investigated by observing its performance when only one winding is excited and the other is disconnected from the load.

When there is an increase in load, shunt capacitors connected in the delta are not sufficient to balance the reactive power demand of ASIG. This may cause poor voltage regulation of the system. The capacitors connected in series with the load are utilized to overcome this problem. The selection of series capacitance should be justified not only on the basis of full load voltage regulation, but also from the viewpoint of load voltage profile and maximum utilization of machine as the generator. Once the shunt capacitance requirement for obtaining any particular no-load terminal voltage has been computed, series capacitance values are used starting from some initial value in equal steps up to some maximum values. A detailed discussion is given in. [27].

## 4.4 Fixed speed grid-connected ASIG

Per phase equivalent circuit of asymmetrical six-phase induction generator in grid-connected fixed speed mode under load condition is exhibited in Fig. 4.8.

Performance characteristics of grid-connected ASIG for fixed speed operation are analyzed with two different types of configurations. In the first setup, only one set of three-phase windings is connected to the grid, while other is supplying a local resistive load as shown in Fig. 4.9a. In the second configuration, both the three-phase winding sets are connected to the utility grid via six-phase to three-phase, three winding transformer, as shown in Fig. 4.9b.

For the first set of configuration, a star connected resistive load is connected to three-phase winding *xyz* and another three-phase winding *abc* is connected to the grid through an autotransformer. In the second set of configuration, the output of both three-phase winding sets *abc* and *xyz* are combined through a $\Delta/Y - Y$ transformer and supplied to the utility grid. An autotransformer is used in between the grid and three-winding transformer to adjust the voltage level according to the laboratory bus bar.

## 4.5 Simulation Results

The system is simulated with MATLAB/SIMULINK in order to verify the effectiveness of the proposed control strategies. The ASIG parameters (listed in the appendix) used in the simulation are acquired from the laboratory prototype developed. Stator terminals of ASIG

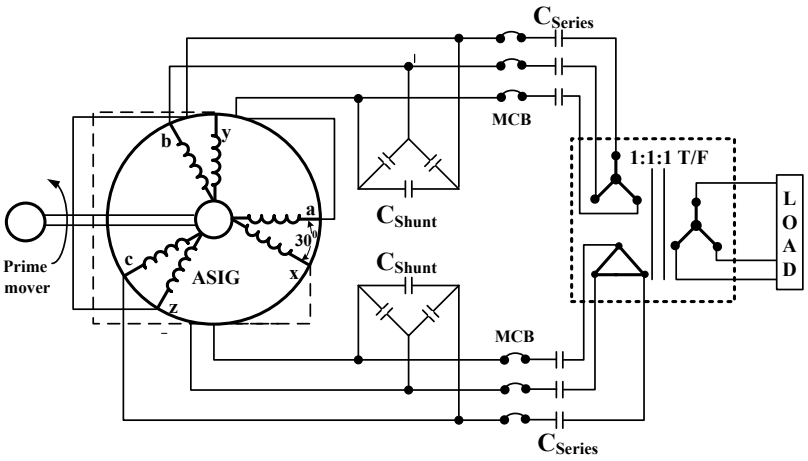


(a)

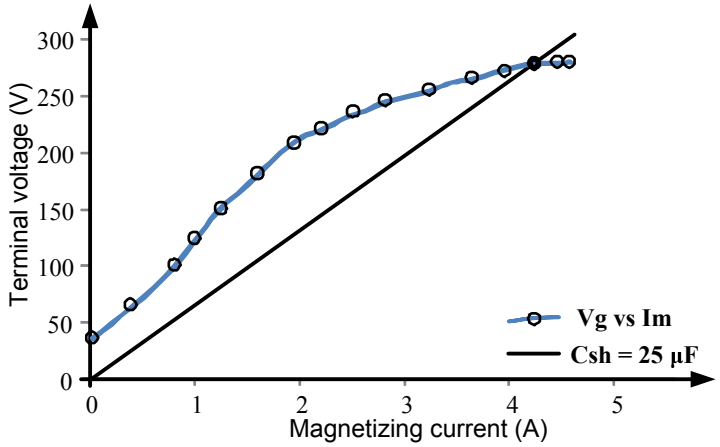


(b)

Fig. 4.7: (a) Schematic diagram of self-excited asymmetrical six-phase induction generator, and (b) Magnetizing characteristics of self-excited SEIG at 1000 rpm.

are connected to distribution grid of 415V, 50Hz via back to back PWM converters. Three-level three-phase grid side converter is connected to two 2-level machine side converters with a common DC link. The system is operated by considering the practical conditions of a variable speed WECS. Generator control acts on the change in wind speed to operate the machine at reference speed obtained from MPPT. DC bus voltage is kept constant at 600V by the supply-side converter. The reactive power required for the generator is supplied by varying $i_q$.

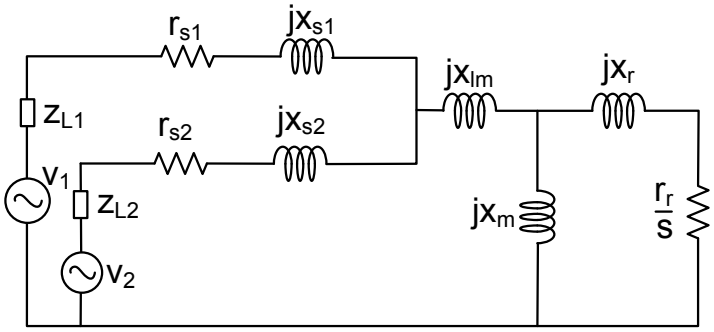


Fig. 4.8: Per phase equivalent circuit of asymmetrical six-phase induction generator under load condition in grid-connected fixed speed mode.

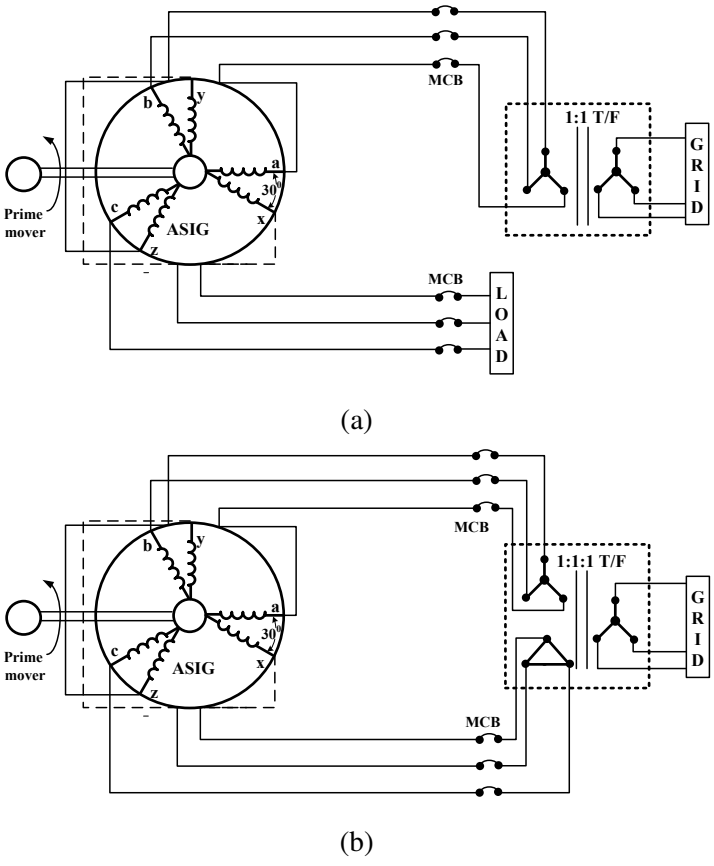


Fig. 4.9: Schematic diagram of ASIG: (a) one set of three-phase winding connected to grid, (b) both sets of three-phase windings connected to utility grid

At t=0.5 secs, wind speed changes from 0 to 8 m/s, Fig. 4.10 shows the generator speed control for variation in wind speeds by using IRFOC, reference speed for generator control at different wind speeds are obtained from MPPT. Generator flux and electromagnetic torque for different wind speeds are presented in Fig. 4.11, as it can be observed, flux remains constant irrespective of the speed change and generator torque changes along with the wind speed.

Direct and quadrature axis currents of the generator, when a change in the wind speed has occurred, are shown in Fig. 4.12. As d-axis current is the flux producing component, it remains constant. Torque producing q-axis current changes with the change in wind speed. The same procedure is repeated when wind speed changes from 8 m/s to 6 m/s at t=1.5 secs

In order to compare the ASIG and conventional three-phase induction generator (TPIG) in the same machine frame, simulations were performed for torque, rotor currents and active power generation. Obtained torque and rotor current waveforms are exhibited in Figs. 4.13 and 4.14. Active power generated by ASIG and TPIG, supplied to the grid at different wind speeds are shown in Fig. 4.15. From these figures, a clear improvement in the quality of torque and rotor current can be observed with ASIG. It should also be noted that ASIG produces more power than conventional TPIG for the same wind speed. Active power flow to the grid increases with the increase in wind speed.

Waveforms of DC-bus voltage and reactive flow between the generator and grid are presented in Fig. 4.16. DC-link voltage is maintained at 600V by continuously varying the d-axis current with the change in wind speed. Reactive power is kept zero for unity power factor operation. Waveforms of quadrature and direct axis currents of supply-side converter for the change in wind speed are depicted in Fig. 4.17.

## 4.6 Experimental results

Laboratory set up detailed in Chapter 2 is developed for performing the experimental investigations of the proposed system.

A multiplication factor as gear ration is considered for deciding the prime mover speed. Depending on the wind speed, the MPPT algorithm decides the optimum generator speed. Rotor field oriented control achieves speed control of ASIG by varying d and q axis currents. Experimental current waveforms of ASIG phase ‘a’ and ‘x’ during steady state are shown

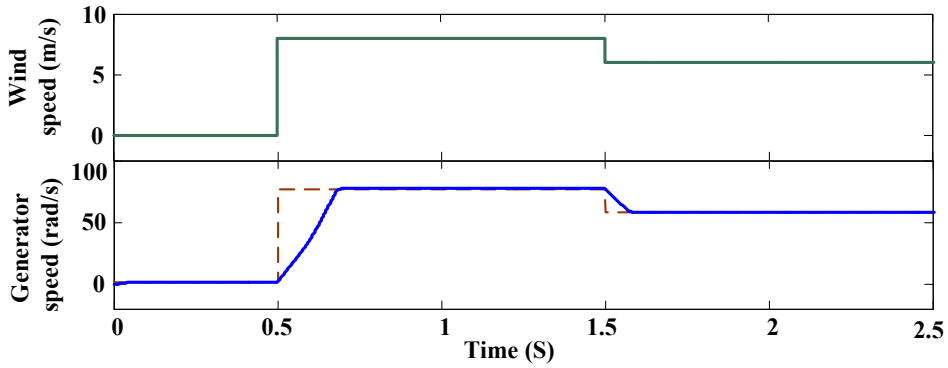


Fig. 4.10: Simulated waveforms of generator speed for change in wind speed.

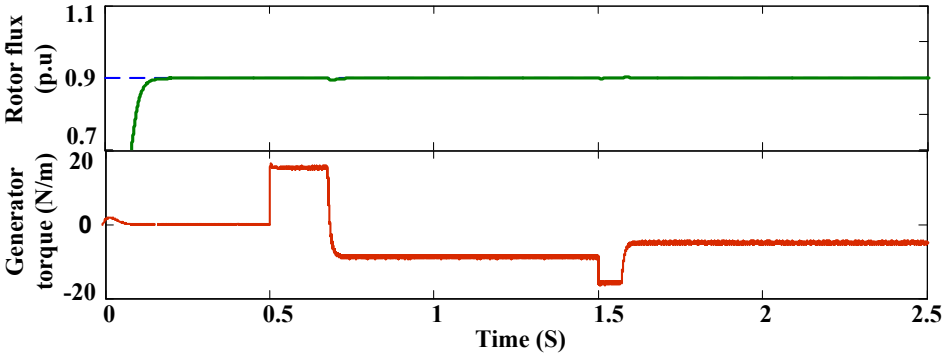


Fig. 4.11: Simulated waveforms of generator flux and torque for change in wind speed.

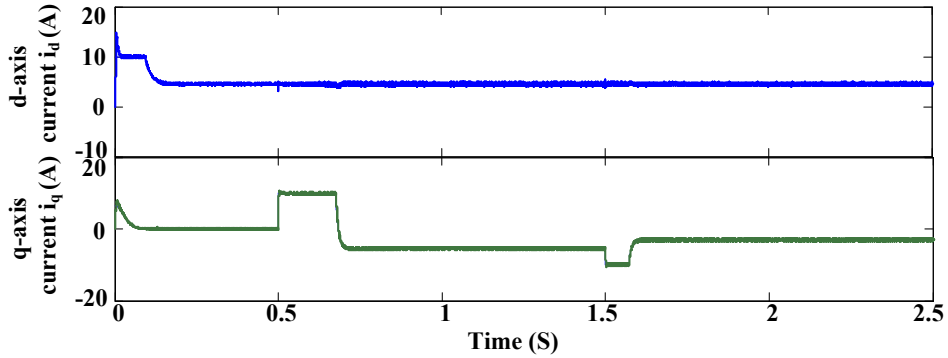


Fig. 4.12: Simulated waveforms of generator direct and quadrature axis currents for change in wind speed.

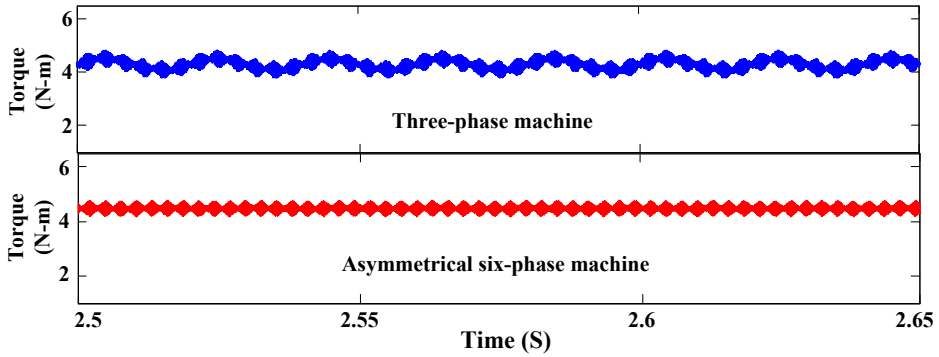


Fig. 4.13: Simulated torque waveforms of conventional three-phase and asymmetrical six-phase induction generator.

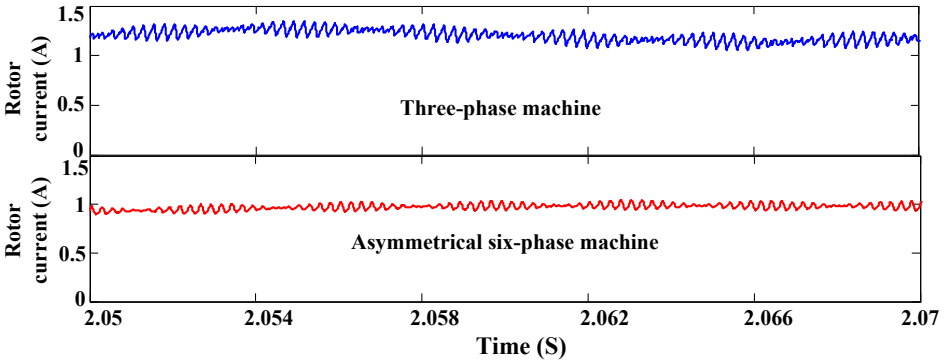


Fig. 4.14: Simulated rotor current waveforms of conventional three-phase and asymmetrical six-phase induction generator.

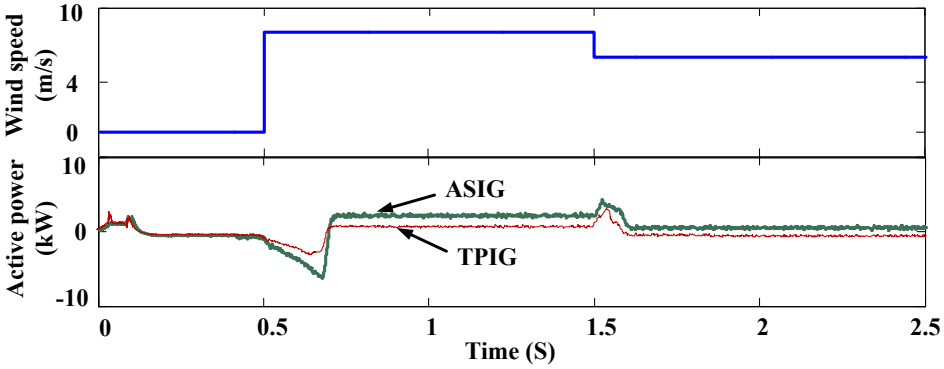


Fig. 4.15: Power supplied to the grid with different wind speeds.

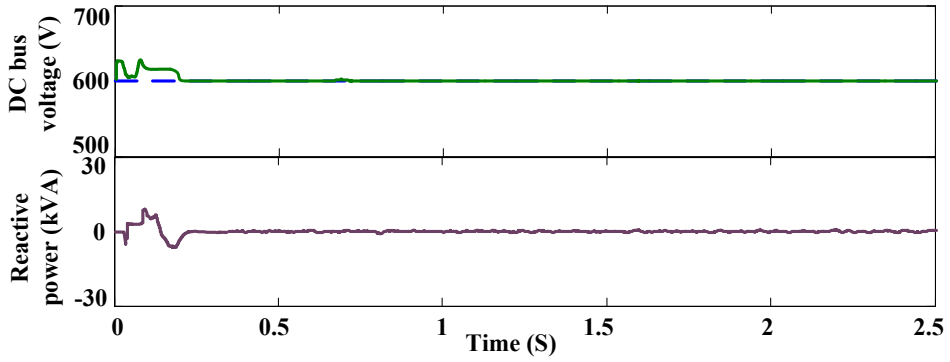


Fig. 4.16: Simulated waveforms of DC bus voltage, reactive power flow for different in wind speed

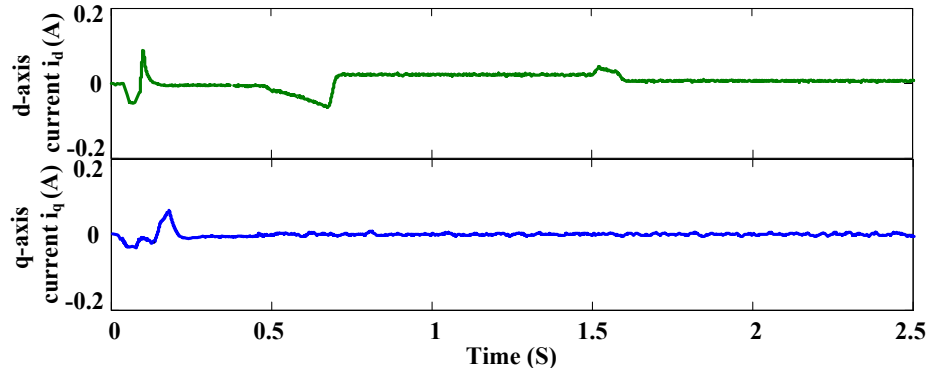


Fig. 4.17: Simulated waveforms of quadrature and direct axis currents of supply side control for different in wind speed

in Fig. 4.18a. A 30°phase shift can be clearly observed between the two sets of three-phase windings. Steady-state generator torque is exhibited in Fig. 4.18b. Experimental waveforms of direct and quadrature axis currents of DTIG ($i_{d1}, i_{q1}, i_{d2}, i_{q2}$) for real-time change in wind speed are shown in Fig. 4.18c, and d. As it can be seen, only $i_q$ varies with $T_e$, $i_d$ is constant so as the generator flux. Negative $i_q$ represents that the machine is operating in generator mode. From these waveforms, the close proximity between the simulated and experimental results can be observed, thus it can be concluded that the model is well capable of predicting the accurate output. Simulated and experimental waveforms also demonstrate that no unbalanced current is shared between the two converters. This is possible because both windings of ASIG are controlled separately in this method.

Grid voltage and current obtained from the experiment are presented in Fig. 4.19a and Fig. 4.19b respectively. Power is fed to the grid with unity power factor operation at varying

wind speeds. Active power of 630W delivered to the grid by ASIG at a wind speed of 6m/s, is shown in Fig. 4.19c. It can be observed reactive power is almost zero thus maintaining unity power factor. Negative sign shows that power is being fed to the grid. The efficiency of ASIG improves with the increase in wind speed.

To transfer power from machine side converter to grid side converter, DC-link voltage should be higher than the peak of the grid voltage, therefore 600V is maintained across the DC link as shown in Fig. 4.19d.

In order to investigate the reliability ASIG in self-excited mode, its performance can be observed when only one winding is excited and other three-phase winding set is disconnected from the load. Experimental tests are conducted by connecting capacitor banks to only one of the two three-phase sets. A three-phase resistive loading is provided to the same set via transformer. Prime mover is operated at a speed of 1000 rpm.

Experimental results obtained are shown in Fig. 4.20. Voltage and current build-up across windings *abc* and *xyz* during excitation process are presented in Figs. 4.20a and b respectively. Its steady state voltage and current waveforms across windings *abc* and *xyz* are presented in Figs. 4.20c and d respectively. From these figures, it is well evident that ASIG in self-excited mode is capable of supplying a load even when capacitor bank is connected across one three-phase winding set. Current across winding *xyz* is zero during both transients and steady state as it is kept open.

Experimental relsults of ASIG in grid-connected fixed speed mode is shown in Fig. 4.21. Only one set of three-phase windings is connected to the grid, while other is supplying a local resistive load active power generated by ASIG is shared between the resistive load and the grid. Variation of power factor, active and reactive power is observed with different values of slip. Figs. 4.21a and b shows the experimental results for this configuration at 0.5% slip. In Fig. 4.21a, steady-state voltage and current waveform across *xyz* terminals are presented, and Fig. 4.21b shows the active power (150 W), reactive power (70 VAR) and operating power factor (0.90) across the resistive load. From these waveforms, it can be concluded that a fixed speed ASIG is well capable of supplying two individual loads.

When both the three-phase winding sets are connected to the utility grid via six-phase to three-phase, three winding transformer total power generated is supplied to the grid. This

configuration is operated at 0.5% slip. Steady state voltage and current waveforms across output terminals of $\Delta/Y - Y$ transformer shown in Fig. 4.21c, and Fig. 4.21d shows active power, reactive power and power factor while supplying utility grid. These waveforms demonstrate that six-phase generator is able to supply three-phase utility grid. Fixed speed ASIG receives reactive power from grid and supplies active power to the grid. This decreases the system power factor, which is improved by connecting a capacitor of suitable value to ASIG windings. Creeping of power factor is observed with the increase in slip, and after a while, it becomes constant at a particular point.

## 4.7 Conclusion

Performance analysis of an asymmetrical six-phase induction generator with different types of configurations is presented in this chapter. For comparative evaluation, the same test machine is utilized as a conventional three-phase induction generator by reconnecting winding terminals.

Asymmetrical six-phase induction generator is operated for variable speed wind power plant. Detailed modeling and analysis in this mode is presented. Control methodologies are designed to regulate the DC-link voltage and to operate the system to supply maximum available power to the grid. Transient and steady-state results obtained from simulation, and experimental investigation proves that this control can operate ASIG at optimum speed without any unbalanced current in the system.

It also focuses on improvements, which can be obtained in the quality of torque and rotor current waveforms when compared to its three-phase counterpart. Implementation of control methodologies are similar to that of a three-phase induction generator, the advantageous feature of ASIG makes it a perfect machine, where reliability and efficiency are the main concern. Fig. 4.22a depicts the power supplied to the grid by test machine operated in six-phase and three-phase mode. As can be seen, power generated in six-phase mode is enhanced, when compared with the power generated as a three-phase induction generator in the same machine frame. Power generation increases, because of dual stator operation, where the output of two stator windings is combined while supplying to the grid. Increase in generated power increases the efficiency of variable speed WECS. Circulating current is avoided with

separate neutral connections.

It is observed that ASIG can be operated in a self-excited mode without any difficulty, even when only one set of three-phase windings is excited. This means that self-excited ASIG can sustain and continue its operation when there is a loss of excitation at one of the three-phase winding sets. Short shunt configuration is observed to be better in terms of voltage regulation and cost-effectiveness, whereas simple shunt in terms of efficiency. Evaluation of test machine in three-phase and six-phase self-excited mode of operation is illustrated in Fig. 4.22b. A variation of output power is plotted with generator terminal voltage. In this, it is noticed that the voltage regulation and power handling capability of six-phase self-excited generator is superior to its three-phase counterpart.

Similar reliability can also be noticed when ASIG is operated in the grid-connected mode with a fixed speed operation. This configuration is well capable of supplying two different loads (local resistive load and utility grid) at the same time. When the output of two-three phase windings are combined with a star-delta transformer and fed to the local utility grid, it is observed that six-phase configuration is able to deliver more power than test machine operated as three-phase in the same machine frame. Power supplied to the grid by ASIG increases with the increase in slip, Fig. 4.22c depicts the variation of output power with slip when the test machine is operated in six-phase and three-phase mode. The system is observed to be well operating even when there is a failure in one of the three-phase sets. The sinusoidal output is obtained in a wide range of speed without causing any overheating. Capacitors are connected across the windings to improve the power factor.

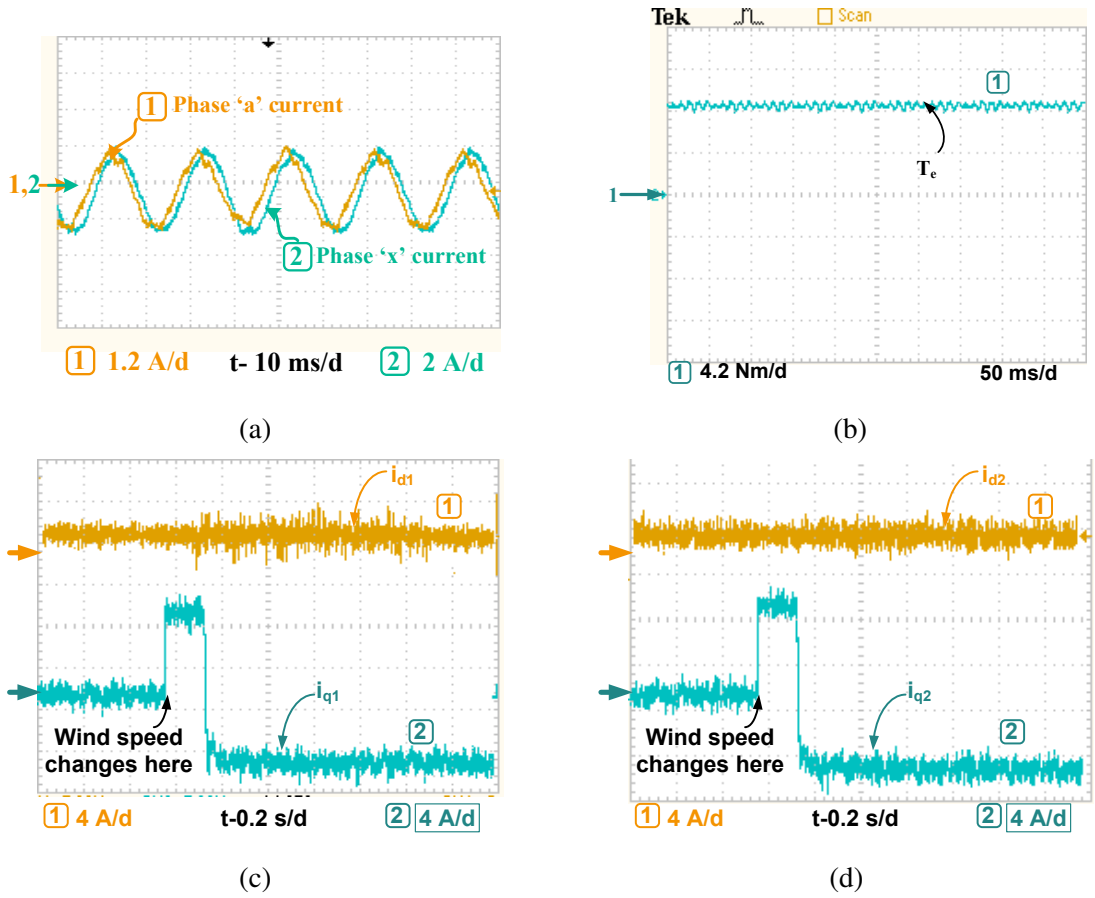


Fig. 4.18: Experimental waveforms of: (a) Generator phase currents $i_a$ and $i_x$, (b) steady state torque, (c) $i_{d1}$ and $i_{q1}$ for variation in wind speed, (d) $i_{d2}$ and $i_{q2}$ for variation in wind speed.

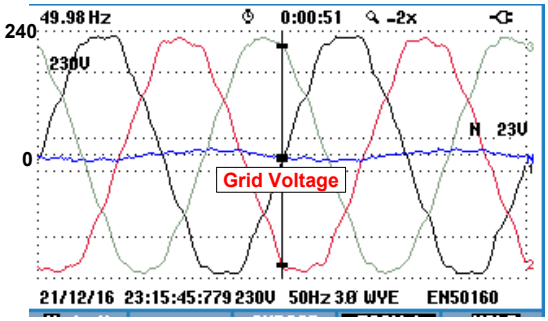


(a)

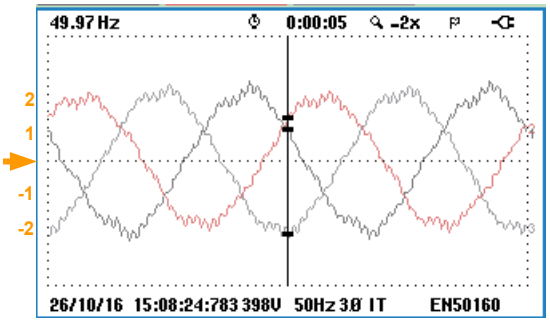


(b)

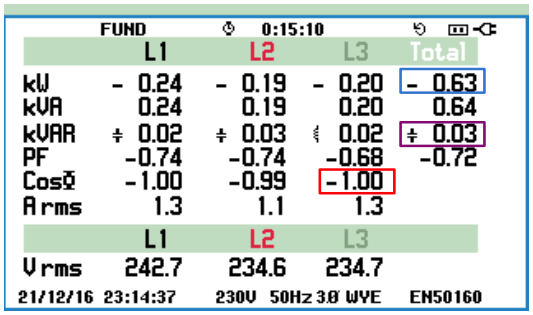


(c)

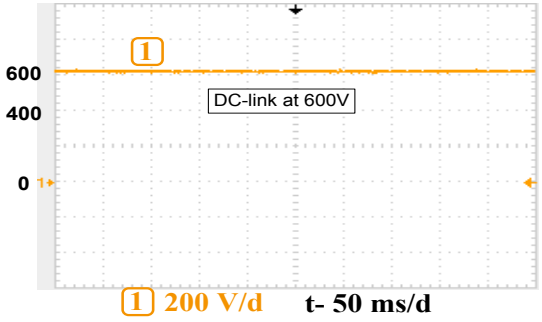


(d)

Fig. 4.19: Experimental waveforms of; (a) Three-phase grid currents $i_a$, $i_b$ and $i_c$, (b) three-phase voltage at grid terminals, (c) power supplied from generator to the grid,(d) constant DC-bus voltage $V_{dc}$

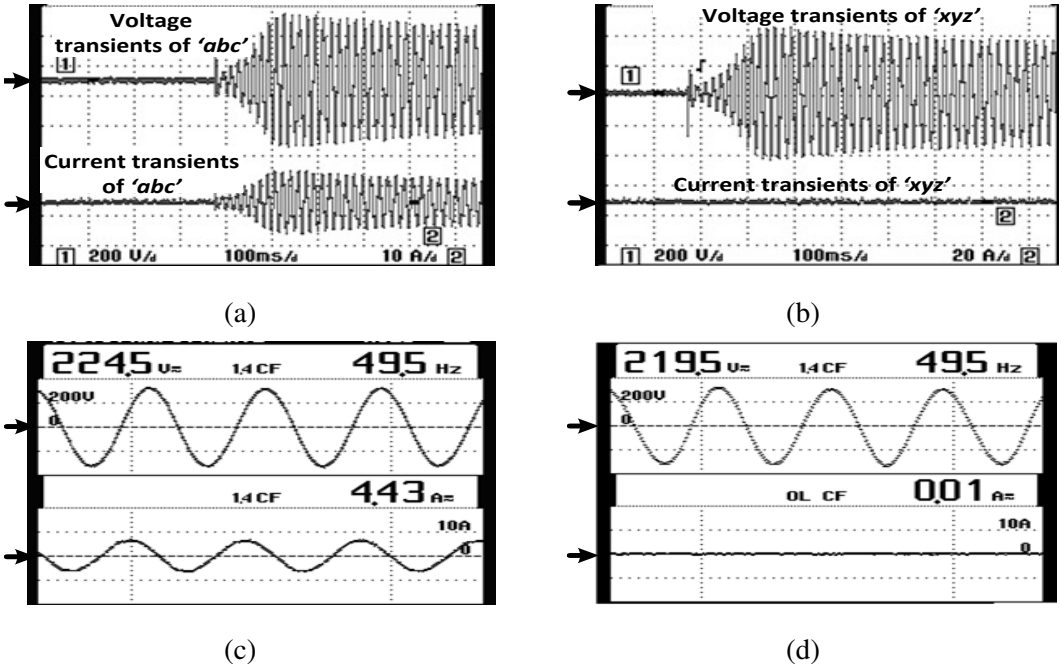


Fig. 4.20: Experimental waveforms of voltage and current build-up across, (a) winding *abc* (connected to three-phase resistive load), and (b) winding *xyz* (kept open). Steady state voltage and current waveforms of, (c) winding *abc* (connected to three-phase resistive load), (d) winding *xyz* (kept open).

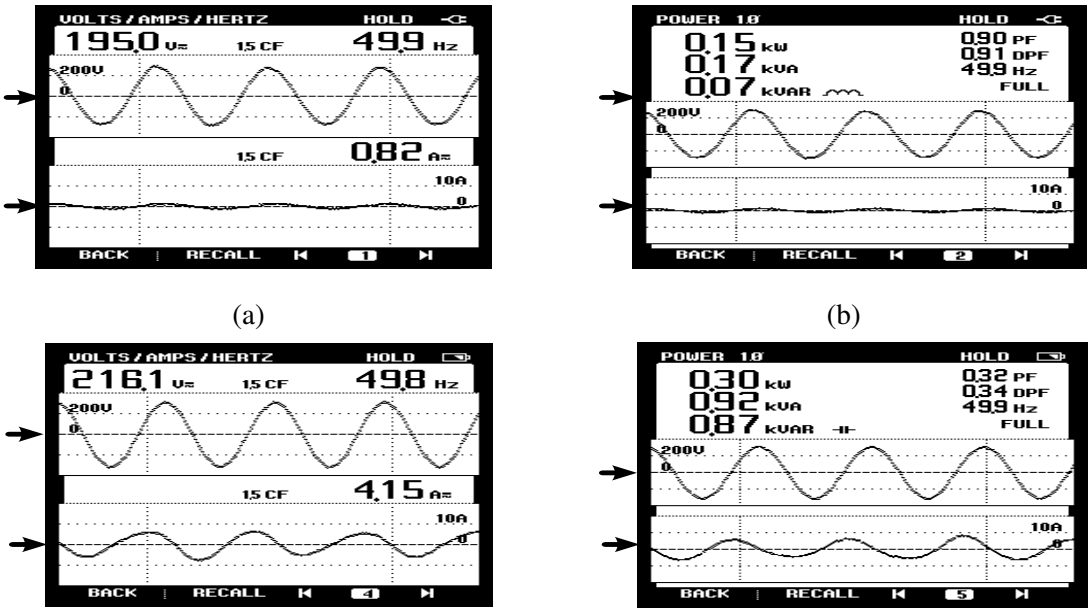


Fig. 4.21: Experimental waveforms across winding $xyz$ supplying 150 W resistive load: (a) Steady state voltage and current, (b) active power, reactive power and power factor.Experimental waveforms across output of three winding transformer: (c) steady state voltage and current, (d) active power, reactive power and power factor.

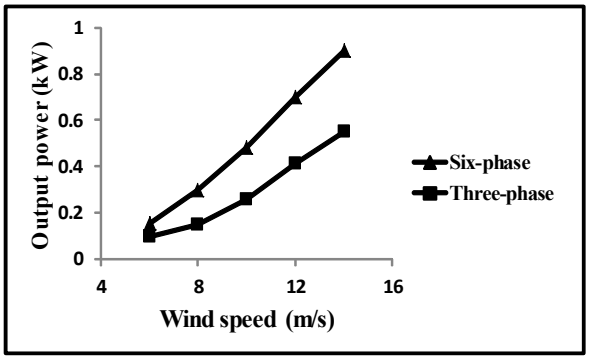


(a)

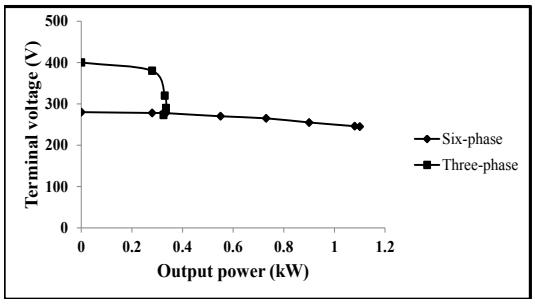


(b)

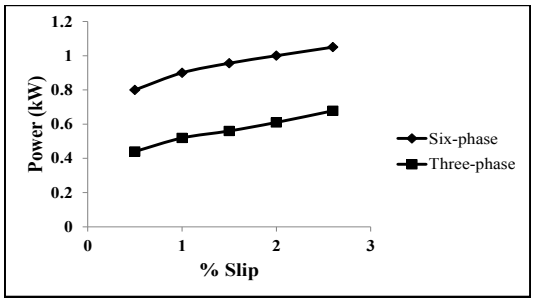


(c)

Fig. 4.22: Comparative performance assessment of test machine operated in three-phase and six-phase; (a) variable speed grid-connected mode, (b) self-excited mode, and (c) fixed speed grid-connected mode.

# CHAPTER 5

# POWER ELECTRONIC INTERFACE INCORPORATING ASIM DRIVE FOR PLUG-IN ELECTRIC VEHICLES

## 5.1 Introduction

This chapter proposes an integrated battery charger for plug-in electric vehicles that involves an asymmetrical six-phase induction motor as propulsion drive. Proposed power electronic interface uses a CuK based bidirectional DC/DC converter, which is capable of performing buck/boost function during all modes of operation. It operates as a power factor correction (PFC) converter during plug-in charging mode, and a single switch inverting buck/boost converter in propulsion and regenerative braking modes. Selection of a wide range of battery voltages and adequate control over regenerative braking can be achieved with the proposed multi-functional converter. In addition, size, weight and cost of the charger are also reduced, as it involves a minimum number of components compared to existing buck/boost converters used in charger. By utilizing a six-phase drive in propulsion system, efficiency and power density of the PEI is improved. This drive even allows further modifications to the proposed topology. Indirect field-oriented control detailed in Chapter 4 is utilized for drive side control. The proposed PEI is highly suitable for onboard charger and propulsion system of PEVs. Aforementioned converter and propulsion drive are validated during all modes of vehicle operation with the laboratory prototype developed.

## 5.2 Onboard battery charger with CuK converter

Most PEVs use two individual converters for their onboard battery charger [46, 50]. The first converter is used to convert ac/dc with unity power factor (UPF) operation, i.e. in plug-in charging mode. The second converter is used for boosting the battery voltage as well to control the power during propulsion and regenerative braking modes. Block diagram of a conventional onboard battery charger (OBC) is shown in Fig. 5.1a. In this system, a large number of components are utilized, which has a negative effect on size and weight of the charger.

The number of components and size can be reduced by utilizing the integrated onboard chargers. These integrated chargers can be designed by either utilizing the inverter and motor windings in the charging process, or by combining DC/DC front end converter (FEC) with power factor correction converter.

The bidirectional DC/DC converter connected between the battery and AC/DC power factor correction (PFC) converter can be combined to have a converter for all modes as shown in Fig. 5.1b. In this regard, this work presents a newly integrated charger consisting of a bidirectional DC/DC converter for PEVs. Fig. 5.2 exhibits the proposed bidirectional DC/DC CuK converter with diode rectifier. Proposed converter has voltage stepping-up and stepping-down capabilities during all vehicular modes. This allows selection of a wide range of battery voltages, and the battery can be charged with universal supply voltage range (100-260 V) as well as effective control of regenerative braking energy. It also offers several advantages in PFC applications such as; continuous input and output current, inrush current limits during transients and overload condition, and lower size of electromagnetic interference (EMI) filter. The presence of output inductor ($L_2$) limits the switching ripples in current reducing the associated losses. This topology would further reduce the number of components compared to other integrated /single-stage converters. In this chapter, this DC/DC converter is further referred to as a battery side converter (BSC).

Asymmetrical six-phase induction machine with two parallel connected inverters is operated as propulsion drive. The six-phase converter system supplying ASIM is referred to as a drive side converter (DSC).

## 5.3 Operation of proposed topology

The Proposed topology consists of an integrated BSC coupled with six-phase DSC. BSC consists of four switches, two diodes, two inductors and three capacitors. It has three modes of operation; plug-in charging, propulsion and regenerative braking, and in each mode, the converter operates in continuous conduction mode (CCM). DSC consists of two parallel converters having twelve switches driving the ASIM operated with indirect rotor field-oriented control. BSC and DSC are coupled with the DC-link. DSC operates only during propulsion and regenerative braking modes of operation, and it remains uninterrupted during plug-in

charging mode.

### 5.3.1 Plug-in charging mode

In this mode, the battery is charged from the grid, so only BSC operates and DSC is in stand still. In BSC, Switch $S_1$ is PWM gated, and switch $S_2$ and $S_3$ are in OFF-state. The proposed converter operates as a CuK PFC converter. Operation of the converter with equivalent circuits is shown in Fig. 5.3a.

In stage: 1, $S_1$ is switched ON, energy is stored in inductor $L_1$ through the path $\mid v_g \mid$-$L_1$-$S_1$-$\mid v_g \mid$, and capacitor $C$ transfers its energy to output capacitor $C_b$ and battery through

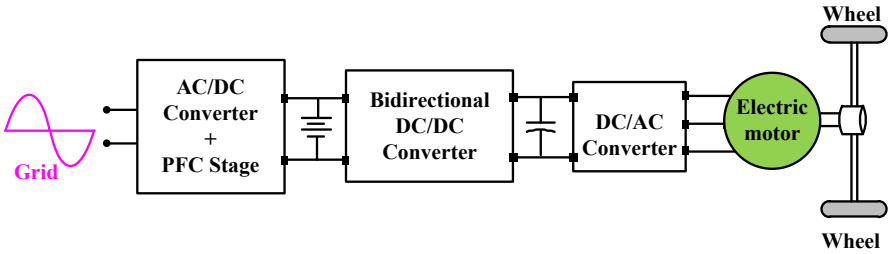


(a)

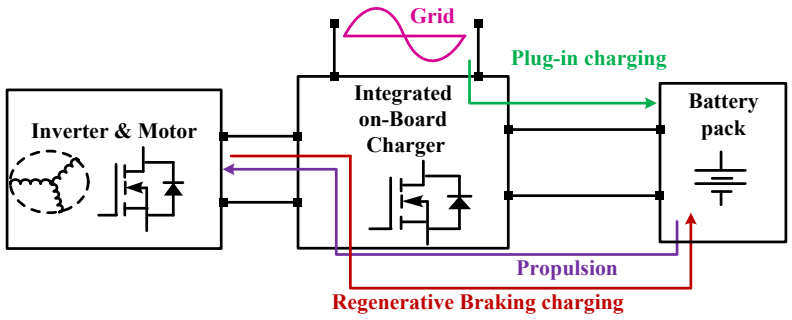


(b)

Fig. 5.1: Block diagram of; (a) conventional battery charger, (b) integrated battery charger.

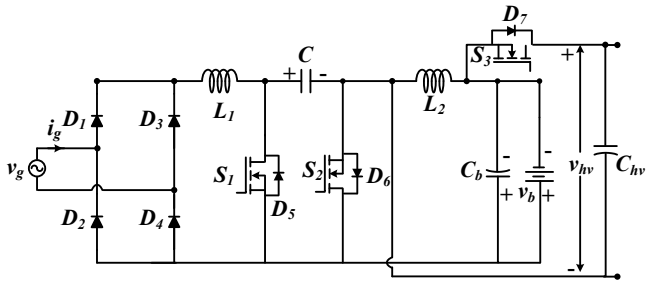


Fig. 5.2: Proposed bidirectional CuK converter for integrated charger in PEVs.

the path $C$-$S_1$-$C_b$-$L_2$-$C$, Inductor $L_1$ current increases and voltage across coupling capacitor decreases.

Switch $S_1$ is turned-OFF in stage: 2, inductor $L_1$ delivers its energy to capacitor $C$, and energy stored in inductor $L_2$ is transferred to capacitor $C_b$. By assuming the duty ratio of converter to be $d_1$, the volt-second balance of any one of the inductors among $L_1$ and $L_2$ in switching period $T_s$ can be written as

$$V_{gmax} \mid sin(\omega t) \mid \times d_1(t) = -V_b \times (1 - d_1(t)) \times T_s \tag{5.1}$$

Hence, the voltage conversion ratio, $M_1$ can be obtained as

$$M_1 = \frac{V_b}{V_{gmax} \left|\sin \omega t\right|} = -\frac{d_1(t)}{1 - d_1(t)} \tag{5.2}$$

### 5.3.2 Propulsion mode

During this mode, power flows from battery to DC-link for propelling of the motor-drive system of the vehicle. DSC operates ASIM in a closed loop. BSC switch $S_1$ and $S_3$ are in OFF-state and switch $S_2$ is PWM gated. Operation of the converter with propulsion mode equivalent circuits is presented in Fig. 5.3b.

Switch $S_2$ is turned-ON in stage: 1, battery charges the inductor $L_2$ through the path $V_b$-$S_2$-$L_2$-$V_b$, and current through inductor increases linearly, meanwhile capacitor $C_{hv}$ discharges to supply energy to the motor through an inverter. When switch $S_2$ is turned-OFF stage: 2, energy stored in $L_2$ is transferred to DC-link capacitor $C_{hv}$ through the path $L_2$-$D_7$-$C_{hv}$-$L_2$.

By assuming the duty ratio of converter to be $d_2$, with the volt-second balance of $L_2$, one can obtain;

$$V_b \times d_2 \times T_s = -V_{hv} \times (1 - d_2) * T_s \tag{5.3}$$

The voltage conversion ratio $M_2$ from (3) can be expressed as

$$M_2 = \frac{V_{hv}}{V_b} = -\frac{d_2}{1 - d_2} \tag{5.4}$$

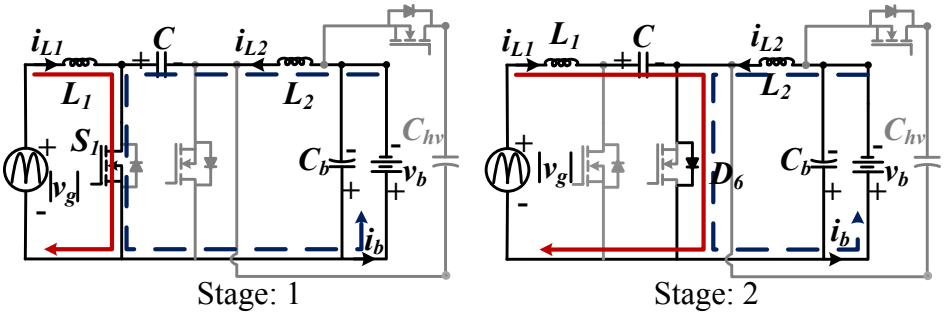


(a)

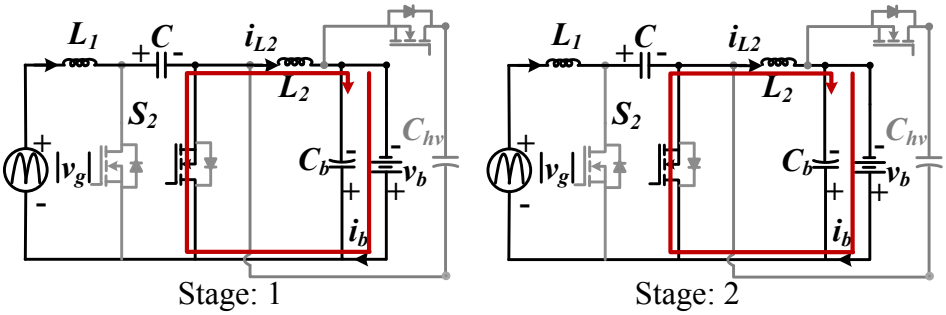


(b)

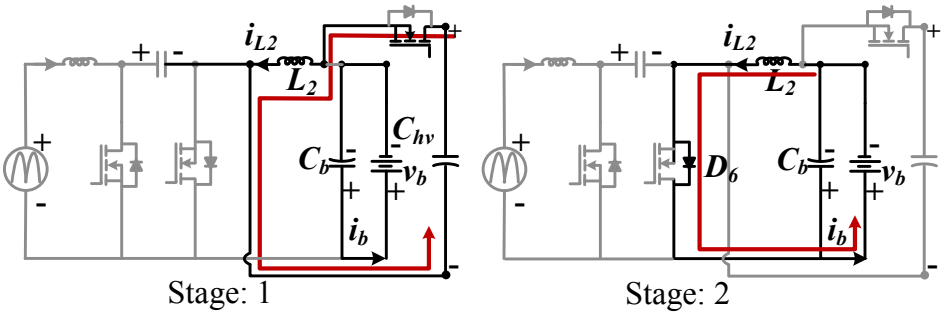


(c)

Fig. 5.3: Operating modes of the converter during; (a) plug-in charging mode, (b) propulsion mode, (c) regenerative braking mode.

### 5.3.3 Regenerative braking mode

In regenerative braking mode, the drive operates in generating mode and DC-link voltage increases the power flow from drive to battery. BSC switch $S_1$and $S_2$ are in OFF-state and switch $S_3$ is gated through PWM signal. In this mode, braking energy of the motor is used to charge the battery and maximizes the distance covered by vehicle per charge. Operation of the converter during regenerative braking is shown in Fig. 5.3c.

By turning-ON switch $S_3$ in stage: 1, inductor $L_2$ begins to charge through the path $V_{hv}$-$S_3$-$L_2$-$V_{hv}$. Meanwhile capacitor $C_b$ discharges to supply energy to the battery. Switch $S_3$ is turned-OFF in stage: 2, $L_2$ releases it stored energy to the capacitor and battery. By assuming the duty ratio of converter to be $d_3$, with the volt-second balance of $L_2$, one can obtain;

$$V_{hv} \times d_3 \times T_s = -V_b \times (1 - d_3) \times T_s \tag{5.5}$$

The voltage conversion ratio $M_3$ from (3) can be expressed as

$$M_3 = \frac{V_b}{V_{hv}} = -\frac{d_3}{1 - d_3} \tag{5.6}$$

## 5.4 Control algorithm

The control strategy is divided into two parts; BSC control and DSC control. BSC control focuses on charging the battery from grid in plug-in charging mode, supplying power to the motor in propulsion mode and redirecting generated power to the battery in regenerative mode. In DSC control, there are only two modes of operation, propulsion and regenerative. Both modes are operated with IRFOC. The control structure of PEI during different modes of converter operation is shown in Fig. 5.4.

### 5.4.1 Control of BSC

In battery control, each mode is implemented by mode selector logic. Mode selector receives the input signals such as grid voltage ($v_g$), battery voltage ($V_b$), electromagnetic torque ($T_e$), speed ($\omega$), and charging power ($P_g$).

During battery charging from the grid, the reference charging power is divided by instantaneous battery voltage, which is input to the outer proportional-integral (PI) controller $G_{z1}$ of a two-loop closed control system. The output of this controller is a reference dc signal,

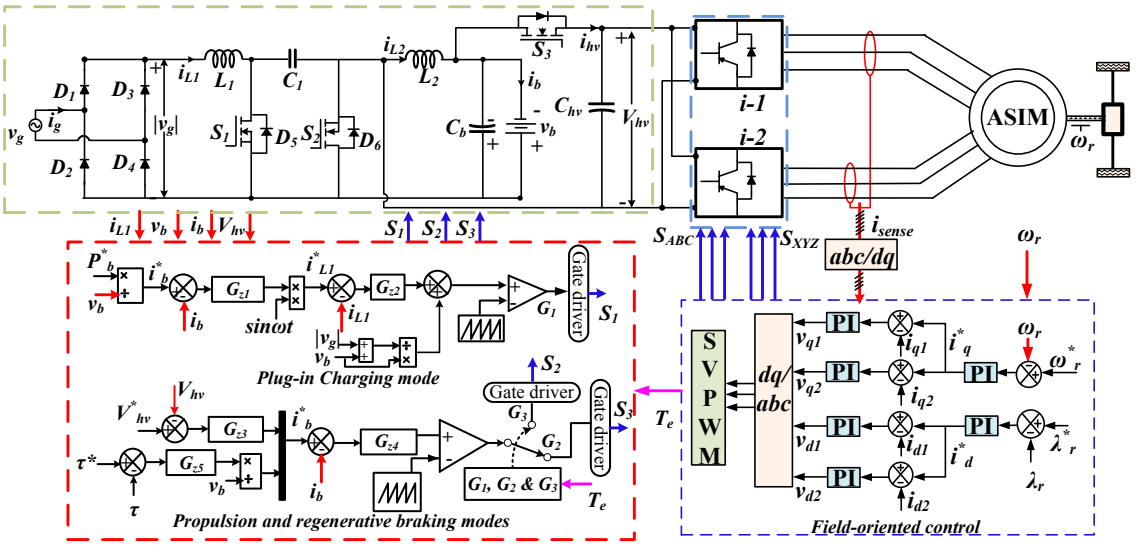


Fig. 5.4: Control scheme of the proposed system during different modes.

which is multiplied by a unit rectified sinusoidal wave to generate final reference input to inner current PI controller $G_{z2}$. This controller is used to correct the power factor on the grid side.

In order to achieve accurate current tracking and make the control system robust against supply variation, a feed-forward loop is implemented in the control loop. The open loop duty cycle from equation 5.2 is added at the output of inner current controller ($G_{z2}$) to arrive final reference PWM signal to switch $S_1$, as shown in Fig. 5.4.

The objective of propulsion mode is to keep the DC-link voltage constant irrespective of any load change for satisfactory operation of the inverter drive system. Therefore, the outer PI controller $G_{z3}$ regulates the DC-link voltage by generating reference battery current to the inner current controller $G_{z4}$, which is provided by an average current mode controller.

In regenerative braking, the reference quantity is usually torque. Therefore, torque is converted into reference charging power, and this reference power is divided by instantaneous battery voltage to generate reference battery current, which is input to current controller $G_{z4}$ for battery current tracking.

### 5.4.2 Control of DSC

Efficient speed control of propulsion drive is necessary for better performance of a PEV. Indirect rotor field-oriented control detailed in Chapter 4 is utilized in this work. It employs

two sets of $d-q$ current controllers.

ASIM increases the efficiency, and improves the performance of propulsion drive. It also provides higher power in the same machine frame. Superior qualities offered by ASIM over its three-phase counterpart can be effectively utilized for EV application. Presented topology can be further improved to involve two sources in the charging process. Details regarding this have been discussed in the future scope.

## 5.5 Simulation results

The simulation results of the proposed converter with 1.5 hp six-pole induction motor drive in all three modes of operation is verified in MATLAB/SIMULINK environment. The parameters (listed in the appendix) used in the simulation are acquired from the laboratory prototype developed.

Fig. 5.5 shows the simulation waveforms in plug-in charging mode, during which DSC is at rest, as is the case for PWM inverter and ASIM. In this mode, the battery is charged from the grid and simultaneously converter operates under PFC mode. In Fig. 5.5a, the grid voltage and current are in the same phase with a sinusoidal shape, which shows that the converter is operating near unity power factor (UPF) condition. The coupling capacitor C in CuK converter is always connected between the input and output in switching cycle; therefore, the voltage developed across it is the sum of rectified grid and battery voltages, as shown in Fig. 5.5b. The battery voltage (with 20% SOC) and current are shown in Figs. 5.5c and d, respectively. In a single-stage charger, the low-frequency component of current oscillates with twice the grid (or line) frequency. This low-frequency ripple has a negligible effect on the battery, as long as voltage ripple caused due to current ripple is lower than 1.5 % of the root mean square (RMS) of float voltage of the batteries [58].

In propulsion mode, the battery delivers power to DC-link capacitor for propelling and acceleration of the vehicle. For smooth operation of the vehicle, the DC-link voltage of the inverter is kept constant during any change of load torque. In this work, DC-link voltage is selected as 400 V. Dynamic performance of PEV in propulsion mode is analyzed by step changing the load torque of ASIM drive. Recorded waveforms are exhibited in Fig. 5.6. At t = 1.5 s load torque is changed from 0 to 5 N.m and again reduced to 0 at t = 2 s, during this load

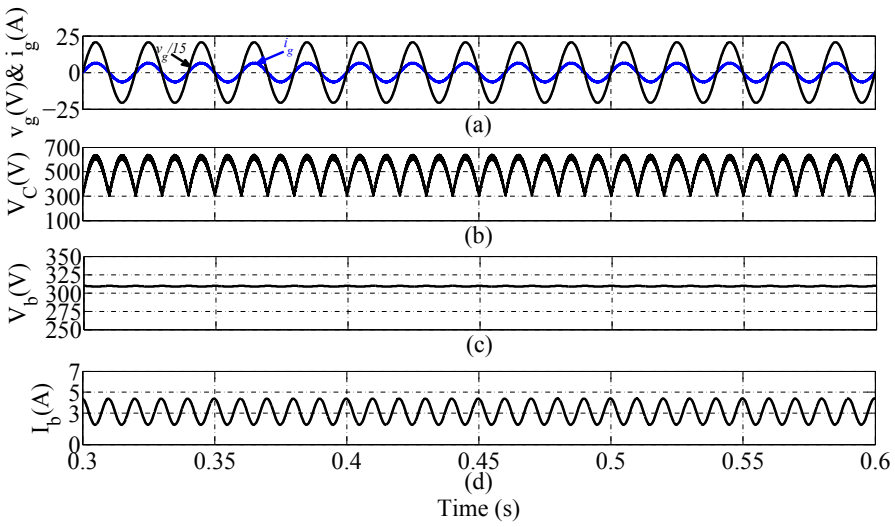


Fig. 5.5: Simulation results during plug-in charging operation; (a) grid voltage ($v_g$) and grid current ($i_g$), (b) voltage developed across coupling capacitor C ($V_C$), (c) voltage across battery ($V_b$), and (d) battery current ($I_b$).

change, DC-link voltage is regulated at 400 V, as shown in Fig. 5.6a. Corresponding change in battery voltage and current are shown in Figs. 5.6b and c, respectively. Fig. 5.6d shows the change in load torque $T_L$ and corresponding motor electromagnetic torque $T_e$. Figs. 5.6e, f and g exhibit the commensurable waveform of rotor flux $\lambda_r$, of $q-$ axis current $i_q$, and $d-$ axis current $i_d$ respectively. As it can be seen, $\lambda_r$ and $i_d$ are constant during load variation, only change in $i_q$ can be observed, hence proving the applicability of IRFOC in propulsion mode.

In regenerative braking mode, the battery is charged with braking energy of the motor. The simulated waveforms of this mode are shown in Fig. 5.7. In this mode, the machine performs as a generator, and the DC-link voltage varies with the generated power. Varying DC-link voltage during regenerative braking is shown in Fig. 5.7a. It operates between 300 and 350 V. Battery voltage and current are shown in Figs. 5.7b and c respectively. As evident from these figures, even though there is a variation in DC-link voltage, the battery is charged with constant current of 2 A. It is remaining constant even after machine stops operating in braking mode, however decrease in DC-link voltage can be observed. When DC-link voltage reaches to a pre-decided minimum value, current direction changes, and the battery starts supplying to drive. Variations in duty cycle waveform with DC-link voltage variations

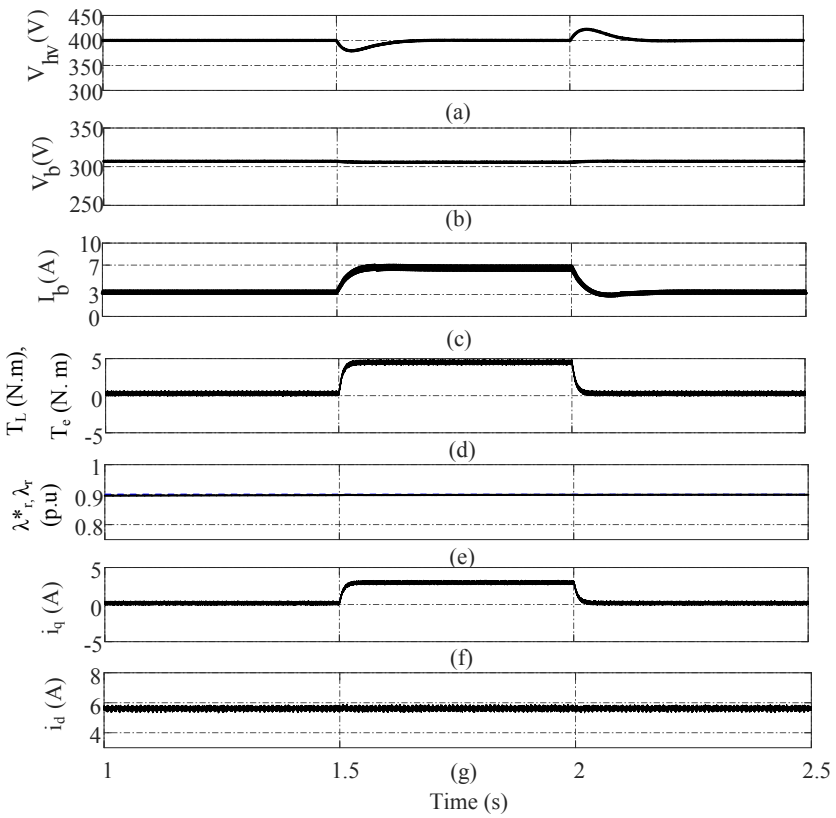


Fig. 5.6: Dynamic operation of converter for propulsion mode. Corresponding waveforms of; (a) DC-link voltage ($V_{hv}$), (b) voltage across battery ($V_b$), (c) battery current ($I_b$), (d) machine torque ($T_e$ and $T_L$), (e) rotor flux ($\lambda_r$), (f) quadrature axis current ($i_q$), and (g) direct axis current ($i_d$).

are exhibited in Fig. 5.7d. When DC-link voltage is more than battery voltage, the duty signal is below 0.5, thus operating in buck mode. When DC-link voltage is lower than the battery voltage, the duty signal increases above 0.5 to operate the converter in boost mode. Corresponding load torque $T_L$ and motor electromagnetic torque $T_e$ during regenerative mode are presented in Fig. 5.7e. Figs. 5.7f, g and h show the waveform of $q-$ axis current $i_q$, rotor flux $\lambda_r$, and $d-$ axis current $i_d$. Even in this mode $\lambda_r$ and $i_d$ are constant during load variation, only change in $i_q$ can be observed, thus demonstrating the applicability of IRFOC in regenerative braking mode.

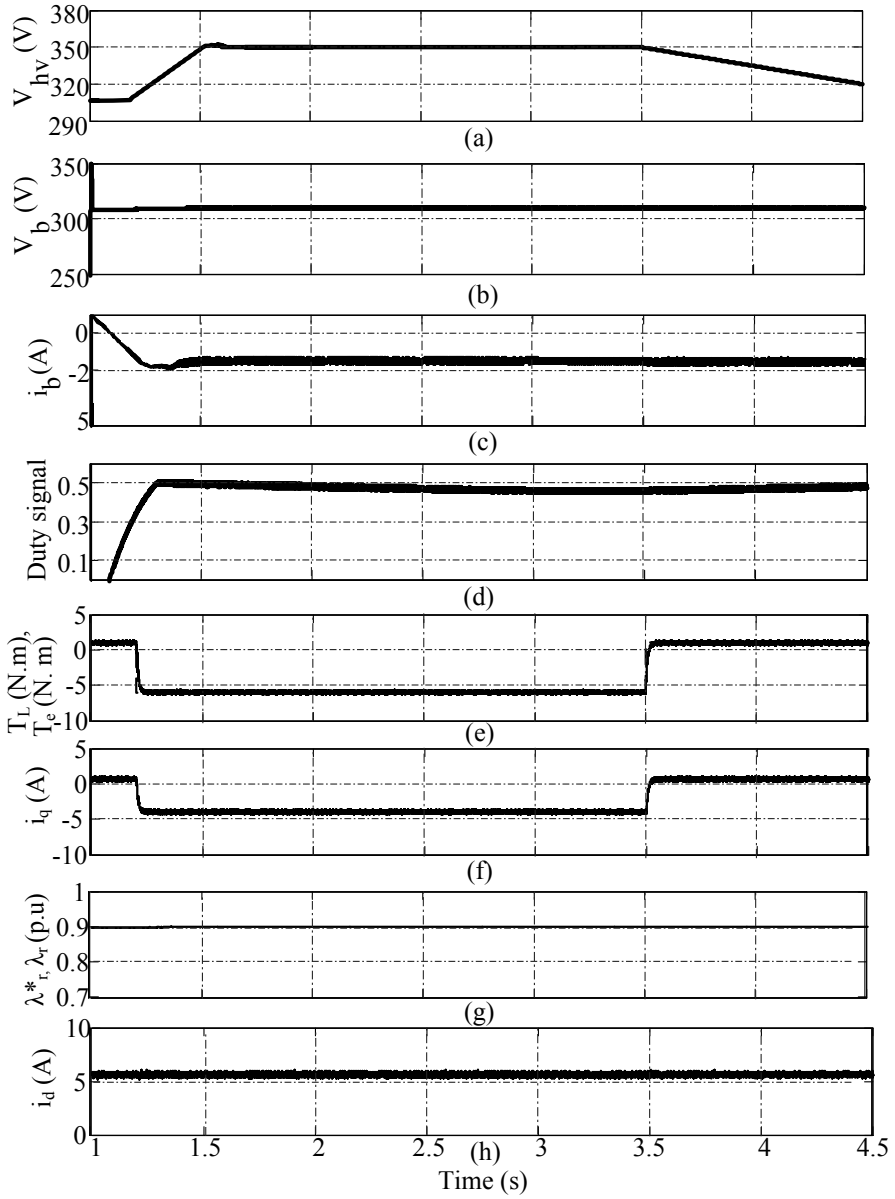


Fig. 5.7: Dynamic operation during regenerative braking mode.Corresponding waveforms of; (a) DC-link voltage ($V_{hv}$), (b) voltage across battery ($V_b$), (c) battery current ($I_b$) (d) duty cycle, (e) machine torque ($T_e$ and $T_L$), (f) quadrature axis current ($i_q$), (g) rotor flux ($\lambda_r$), and (h) direct axis current ($i_d$).

## 5.6 Experimental results

An experimental prototype of the power electronic interface (PEI) for PEV is built in the laboratory. It is explained in detail in Chapter 2.

Fig. 5.8 shows the experimental results obtained during plug-in charging mode and propulsion mode. The grid voltage (CH-1), grid current (CH-2), battery voltage (CH-3) and battery current (CH-4) are shown in Fig. 5.8a. As can be seen, grid voltage and currents are in the same phase with a sinusoidal shape, which indicates near unity power factor (UPF) operation of the converter. The UPF operation relieves the burden on supply systems and reduces the electricity usages. The low-frequency oscillations in battery current can be observed, and this depends on filter inductor connected in series with the battery. The voltage across coupling capacitor $C$ and current through inductor $L_1$ are shown in Fig. 5.8b. The coupling capacitor voltage is the sum of battery and rectified grid voltage, thus providing verification for simulation result in plug-in charging mode.

The dynamic operation during propulsion mode is tested by varying the load torque. Corresponding changes in the battery voltage ($V_b$) and battery current ($I_b$) are presented in Fig. 5.8c. The DC-link voltage ($V_{hv}$) is been maintained at 300 V. In this case, it is not necessary to maintain 600V as power is not supplied back to the grid. Therefore, this voltage is decided based on the availability of batteries in the laboratory. The direct ($i_d$) and quadrature axis ($i_q$) currents of ASIM drive during IRFOC are shown in Fig. 5.8d. As it can be observed, $i_q$ varies with the variation in load torque and electromagnetic torque $T_e$. $i_d$ is constant so as the rotor flux of ASIM.

In regenerative braking mode, braking energy of the motor is used to charge the battery, which leads to a long run of a vehicle per charge. As the regenerative power is marginal. DC-link is maintained at 200 V. Output waveforms in this mode are exhibited in Fig. 5.9a. In the figure, the battery voltage is constant 150 V, negative battery current of 2 A indicates charging of the battery from propulsion drive. Generating operation of ASIM is shown in Fig. 5.9b. Even in this mode, quadrature axis $i_q$ varies with the variation in input load torque. Direct axis current $i_d$ is constant so as the rotor flux of ASIM.

Fig. 5.9c depicts the machine currents in stationary frame of reference ($i_{\alpha 1}$ and $i_{\alpha 2}$) during speed reversal. Thirty-degree phase displacement between the current waveform of two

Table 5.1: Comparison study of the proposed charger with single-stage chargers

| Converter Topologies | Modes of operation | | | Switches | Diodes | Inductors |
|---|---|---|---|---|---|---|
| | Plug-in charging | Propulsion | Regenerative braking | | | |
| Boost PFC converter | Boost | Buck/boost | Buck/boost | 5 | 5 | 2 |
| Inverting buck/boost Converter | Buck/boost | Buck/boost | Buck/boost | 5 | 5 | 2 |
| SEPIC PFC converter | Buck/boost | Buck/boost | Buck/boost | 5 | 5 | 3 |
| CuK PFC converter | Buck/boost | Buck/boost | Buck/boost | 5 | 5 | 3 |
| Integrated converter [58] | Boost | Buck/boost | Buck/boost | 4 | 4 | 1 |
| Integrated converter [59] | Boost, buck/boost* | Boost | Buck | 5 | 1 | 1 |
| Integrated converter [60] | Buck/boost | Buck/boost | Buck/boost | 6 | 9 | 1 |
| Proposed integrated converter | Buck/boost | Buck/boost | Buck/boost | 3 | 4 | 2 |

*Boost in positive half cycle and buck/boost in negative half cycle

three-phase sets can be clearly observed. Quadrature and direct-axis currents ($i_q$ and $i_d$) for variation in reference speed during IRFOC is exhibited in Fig. 5.9d.

## 5.7 Comparative analysis

A comparative study of the presented charger with conventional single-stage and existing integrated chargers is presented in Table 5.1. To have a fair comparison, the dc/dc converters connected between the battery and DC-link are assumed to be a four-quadrant bidirectional converter. In addition to these conventional chargers, other existing integrated chargers are also included in the comparative analysis. It can be seen from Table 5.1, the proposed converter has the least components compared to those converters, which have buck/boost operation in each mode.

## 5.8 Conclusion

In this chapter, a new power electronic interface involving integrated DC/DC converter and a six-phase induction machine have been proposed for plug-in electric vehicles. As presented in the comparative analysis, the proposed charger utilizes the least number of components along with providing buck/boost operation in all vehicle modes. It also discusses the advantages of

utilizing a six-phase induction motor drive instead of a conventional three-phase drive.

The stepping-up and stepping-down capabilities offered by the charges in all modes of vehicle operation allows for the selection of wide range of battery voltages, and the battery can be charged with universal supply voltage range (100-260 V) as well as effective control of regenerative braking energy. A single converter is utilized to achieve all modes of vehicle operation without influencing the charging time. The charging time of the integrated CuK converter will remain same as that of conventional CuK converter. A six-phase machine is used in the propulsion drive to improve efficiency and reliability. Even though it increases the size of vehicle, it allows for further improvements to include another source for battery charging. Indirect field-oriented control of ASIM drive is able to perform both motoring and generating operations.

The performance of PEI in each mode has been verified by both simulations as well as hardware results. Efficient closed loop control algorithm has been developed to control BSC and DSC in all three modes of operation. The effectiveness of BSC controller is examined by achieving unity power factor operation in plug-in charging mode, regulating DC-link voltage at a desired value with a step change of loads in propulsion mode, and recharging of battery in the regenerative braking mode. Performance of DSC controller is analyzed by observing the torque and speed control in propulsion and regenerative braking mode. IRFOC presented can be further improved to obtain a fault-tolerant drive system using ASIM.

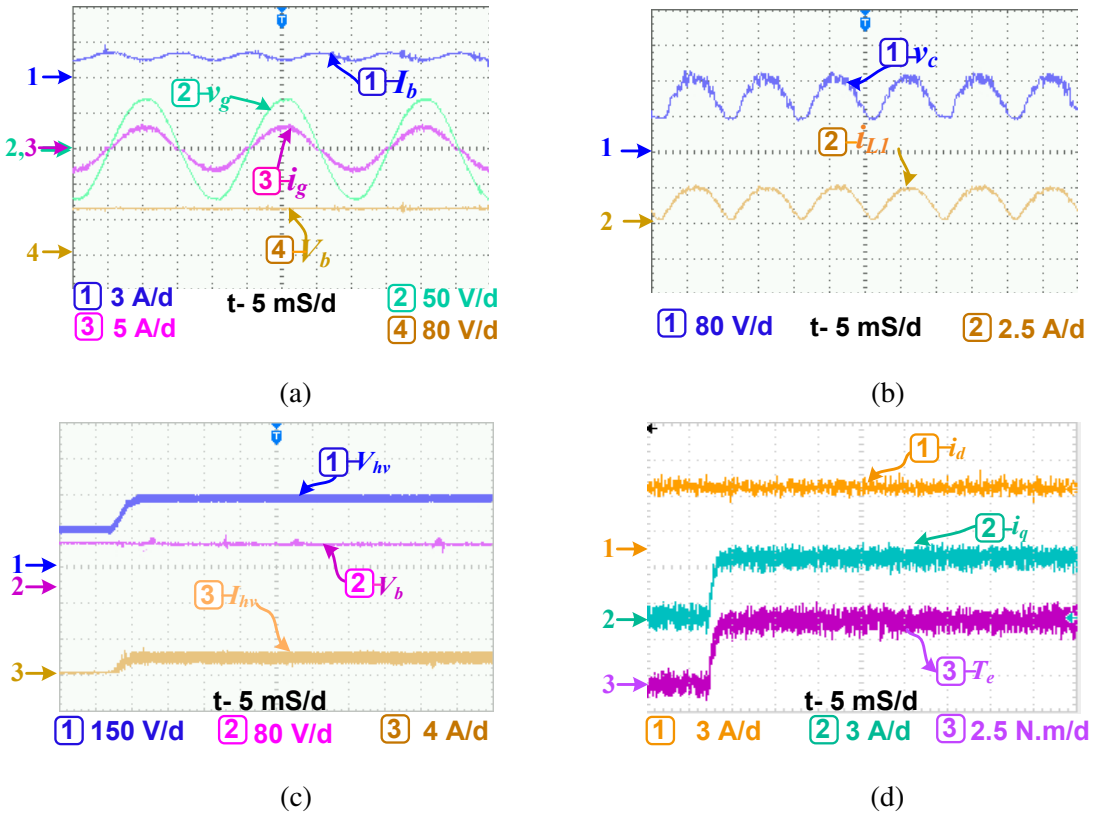


Fig. 5.8: Experimental waveforms captured; (a) grid voltage $v_g$, grid current $i_g$, battery voltage $V_b$ and battery current $I_b$ during charging, (b) waveforms of coupling capacitor voltage $v_c$ and inductor current $i_{L1}$ during charging, (c) DC-link voltage ($V_{hv}$), battery voltage ($V_b$), and battery current ($I_b$) during transition from plug-in charging to propulsion mode, (d) dynamics of field oriented controlled ASIM, direct-axis current ($i_d$), quadrature-axis current ($i_q$), and electromagnetic torque ($T_e$).

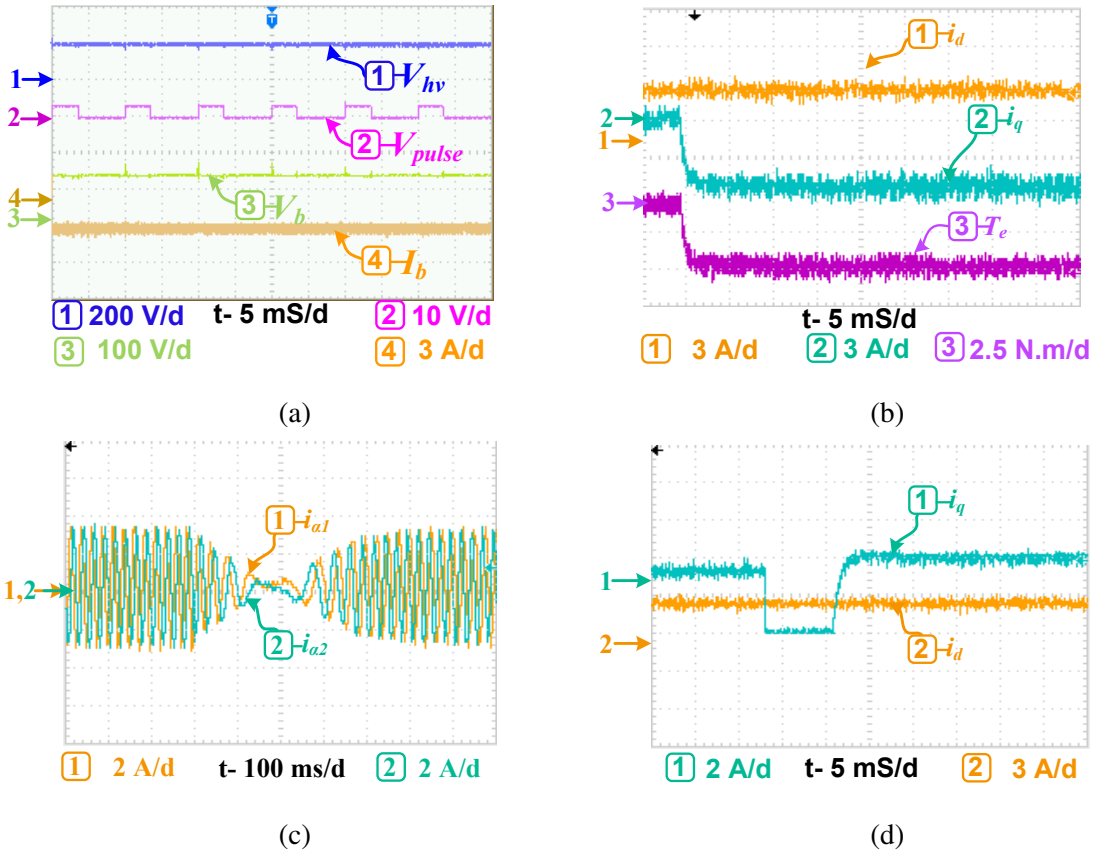


Fig. 5.9: Experimental waveforms during regenerative braking operation; (a) DC-link voltage ($V_{hv}$), switching pulse ($V_{pulse}$), battery voltage ($V_b$), and battery current ($I_b$) battery voltage (b) dynamics of field oriented controlled ASIM, direct-axis current ($i_d$), quadrature-axis current ($i_q$), and electromagnetic torque ($T_e$), (c) ASIM currents during speed reversal in stationary reference frame $i_{\alpha 1}$ and $i_{\alpha 2}$, (d) currents in synchronous reference frame $i_d$ and $i_q$.

# CHAPTER 6

# CONCLUSION AND FUTURE SCOPE

## 6.1 Conclusion

This thesis presents an analysis of asymmetrical six-phase induction machine for renewable and sustainable energy applications. It examines the applicability of ASIM drive in conjunction with different types of wind energy conversion systems and power electronic interface for plug-in electric vehicles. The following main issues have been discussed.

- A detailed mathematical model of asymmetrical six-phase induction machine, and six-phase voltage source converter are developed for simulation purposes. The mutual leakage coupling between two three-phase sets and cross saturation coupling are also considered in the dynamic model. Systematic analysis of four different space vector PWM techniques in-terms of torque pulsation and harmonic contents are performed for ASIM drive. On the basis of the outcome, the best suitable SVPWM is considered during the variable speed operation of ASIM drive. Indirect rotor field oriented control for ASIM is developed by utilizing the dynamic model of ASIM and six-phase VSC. The deductions are outlined as follows.

    i. The generalized analytical model is developed in arbitrary reference frame, hence is versatile, and can be easily employed to develop any type of control based on the requirement.

    ii. In space vector modulation schemes, conventional SVPWM generates more harmonics, however DC-link utilization is maximum. Vector classification reduces the harmonics, but still has slightly increased amplitude of pulsating torque. VSD and CMVI SVPWM are very satisfactory in terms of harmonics and torque pulsation, nevertheless, CMVI SVPWM requires lesser computational time.

    iii. IRFOC developed for the six-phase drive is very effective in terms of speed control, and unbalanced currents and asymmetries associated with the switching harmonics are eliminated by employing the sufficient number of PI controllers.

iv. Protuberance during load change is reduced by feed-forwarding input load torque as an equivalent q-axis current, this does not require any additional PI controller.

- The variable speed ASIM drive is operated as a grid-connected generator for WECS. Back to back voltage source converts are connected between the grid and generator. Dynamic modeling of wind turbine, grid, and grid side converter are developed and integrated with the ASIM drive model. Generator side converters are operated for maximum power point tracking and grid side converters for unity power factor control. Applicability of asymmetrical six-phase induction generator is also investigated in self-excited and grid-connected fixed speed operating modes. The following conclusions can be underlined.

  i. In a variable speed WECS, ASIG with indirect field-oriented control is well capable of extracting maximum power from the wind during all wind speeds.

  ii. Power generated from the ASIG is supplied to the grid with unity power factor, by implementing grid vector-oriented control.

  iii. In self-excited mode, ASIG can be operated without any difficulty even when capacitor banks are connected to only one three-phase winding set.

  iv. During grid-connected fixed speed operation, ASIG is capable for supplying two different loads (local resistive load and utility grid) at the same time.

  v. Overall, in three different modes of operation, a power enhancement of 150-165% is observed when operated as six-phase machine in the same machine frame as compared to three-phase counterpart.

- A power electronic interface involving ASIM as propulsion drive, and CuK based converter as onboard charger is developed for plug-in electric vehicles. CuK based bidirectional DC/DC converter is modeled and integrated with the dynamic model of ASIM drive. The results are summarized as follows.

  i. The DC/DC converter is capable of performing the buck/boost function during all modes of vehicle operation.

ii. With this charger, wide range of battery voltages can be selected. Furthermore, battery can be charged with universal supply voltage range (100-260 V), and efficient control of regenerative braking energy can be obtained.

iii. The proposed charger utilizes the least number of components compared to other existing converters.

iv. Six-phase machine used in propulsion drive improves the system efficiency and reliability.

- All the simulation results are validated using the laboratory prototype developed. dSPACE-DS1104, an FPGA based controller is utilized for real-time implementation. Single hardware setup is transformed into different configurations based on the requirement.

## 6.2 Future Scope

The research work presented in this thesis focuses on developing a simple, but effective field-oriented control for six-phase induction machine. The applicability of this drive is assessed for variable speed wind energy conversion system and plug-in electric vehicles. Future expansion of the works presented in this thesis includes:

- Implementation of the mentioned control techniques with a dedicated DSP or FPGA.
- The further reduction in the number of sensors utilized in IRFOC will reduce the overall cost of the drive.
- The IRFOC control strategy can be further improvised by optimizing the post-fault currents externally. Reliability of the system will be increased due to ASIMs post-fault disturbance-free operation.
- Advantages offered by the six-phase drive can be explored to other interesting areas such as standalone generators in ship, more electric aircraft, and various industrial applications.
- Proposed PEI for plug-in electric vehicle can be further modified to utilize two different sources in the charging process as shown in Fig. 6.1. Battery charging through six-phase machine winding with single-phase grid has been discussed in [90]. With the

incorporation of these modifications, a secondary source like solar PV cells can be connected across switch $S_1$ to charge the battery even during propulsion. Switch $S_1$ is operated to perform maximum power point tracking (MPPT). The inductor in input side of the converter reduces the current ripple, thus improving the operating life of battery.

- Other than vehicular applications, the proposed integrated converter can be utilized even for grid interfacing of photo-voltaic systems.

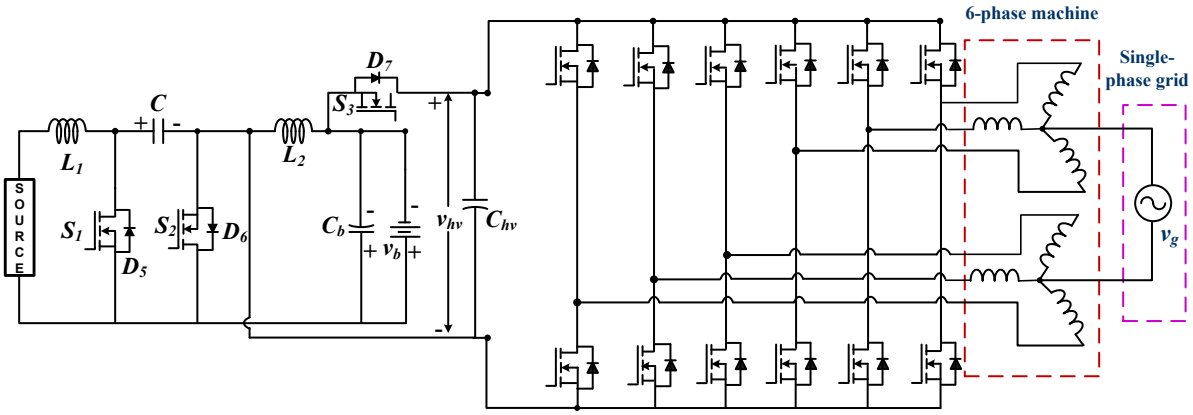


Fig. 6.1: PEV operated with grid and PV source for battery charging.

# BIBLIOGRAPHY


[1] *Wind in power: 2015 European statistics*, Feb. 2016, [Online] Available: http://windeurope.org.

[2] D. Das, S. Aditya, and D. Kothari, "Dynamics of diesel and wind turbine generators on an isolated power system," *International Journal of Electrical Power & Energy Systems*, vol. 21, no. 3, pp. 183–189, 1999.

[3] B. Singh and S. Singh, "Voltage stability assessment of grid-connected offshore wind farms," *Wind Energy: An International Journal for Progress and Applications in Wind Power Conversion Technology*, vol. 12, no. 2, pp. 157–169, 2009.

[4] S. Chapman, *Electric machinery fundamentals*. Tata McGraw-Hill Education, 2005.

[5] M. Cheng and Y. Zhu, "The state of the art of wind energy conversion systems and technologies: A review," *Energy Conversion and Management*, vol. 88, pp. 332–347, 2014.

[6] Y. Fan, K. Chau, and M. Cheng, "A new three-phase doubly salient permanent magnet machine for wind power generation," *IEEE Transactions on Industry Applications*, vol. 42, no. 1, pp. 53–60, 2006.

[7] F. Barrero and M. J. Duran, "Recent advances in the design, modeling, and control of multiphase machinespart i," *IEEE Transactions on Industrial Electronics*, vol. 63, no. 1, pp. 449–458, Jan 2016.

[8] L. K. Panwar, K. S. Reddy, R. Kumar, B. Panigrahi, and S. Vyas, "Strategic energy management (sem) in a micro grid with modern grid interactive electric vehicle," *Energy conversion and management*, vol. 106, pp. 41–52, 2015.

[9] A. F. Burke, "Batteries and ultracapacitors for electric, hybrid, and fuel cell vehicles," *Proceedings of the IEEE*, vol. 95, no. 4, pp. 806–820, 2007.

[10] C. C. Chan and K. T. Chau, "An overview of power electronics in electric vehicles," *IEEE Transactions on Industrial Electronics*, vol. 44, no. 1, pp. 3–13, Feb 1997.

[11] E. E. Ward and H. Hrer, "Preliminary investigation of an invertor-fed 5-phase induction motor," *Electrical Engineers, Proceedings of the Institution of*, vol. 116, no. 6, pp. 980–984, June 1969.

[12] B. K. Bose, *Power electronics and variable frequency drives: technology and applications*. Wiley Online Library, 1997.

[13] E. Levi, "Multiphase electric machines for variable-speed applications," *IEEE Transactions on Industrial Electronics*, vol. 55, no. 5, pp. 1893–1909, May 2008.

[14] G. K. Singh, "Multi-phase induction machine drive research survey," *Electric Power Systems Research*, vol. 61, no. 2, pp. 139–147, 2002.

[15] S. Padmanaban, G. Grandi, F. Blaabjerg, P. W. Wheeler, and J. O. Ojo, "Analysis and implementation of power management and control strategy for six-phase multilevel ac drive system in fault condition," *Engineering Science and Technology, an International Journal*, vol. 19, no. 1, pp. 31–39, 2016.

[16] A. Tani, M. Mengoni, L. Zarri, G. Serra, and D. Casadei, "Control of multiphase induction motors with an odd number of phases under open-circuit phase faults," *IEEE Transactions on Power Electronics*, vol. 27, no. 2, pp. 565–577, Feb 2012.

[17] X. Wang, Z. Wang, Z. Xu, M. Cheng, W. Wang, and Y. Hu, "Comprehensive diagnosis and tolerance strategies for electrical faults and sensor faults in dual three-phase pmsm drives," *IEEE Transactions on Power Electronics*, pp. 1–1, 2018.

[18] G. K. Singh, "Modeling and experimental analysis of a self-excited six-phase induction generator for stand-alone renewable energy generation," *Renewable energy*, vol. 33, no. 7, pp. 1605–1621, 2008.

[19] G. K. Singh, A. S. Kumar, and R. P. Saini, "Performance analysis of a simple shunt and series compensated six-phase self-excited induction generator for stand-alone renewable energy generation," *Energy Conversion and Management*, vol. 52, no. 3, pp. 1688–1699, 2011.

[20] O. Ojo and I. E. Davidson, "Pwm-vsi inverter-assisted stand-alone dual stator winding induction generator," *IEEE Transactions on Industry Applications*, vol. 36, no. 6, pp. 1604–1611, Nov 2000.

[21] D. Wang, W. Ma, F. Xiao, B. Zhang, D. Liu, and A. Hu, "A novel stand-alone dual stator-winding induction generator with static excitation regulation," *IEEE Transactions on Energy Conversion*, vol. 20, no. 4, pp. 826–835, Dec 2005.

[22] F. Bu, W. Huang, Y. Hu, and K. Shi, "An excitation-capacitor-optimized dual stator-winding induction generator with the static excitation controller for wind power application," *IEEE Transactions on Energy Conversion*, vol. 26, no. 1, pp. 122–131, March 2011.

[23] D. Wang, W. Ma, F. Xiao, B. Zhang, D. Liu, and A. Hu, "A novel stand-alone dual stator-winding induction generator with static excitation regulation," *IEEE Transactions on Energy Conversion*, vol. 20, no. 4, pp. 826–835, Dec 2005.

[24] Z. Zhang, Y. Yan, S. Yang, and Z. Bo, "Development of a new permanent-magnet bldc generator using 12-phase half-wave rectifier," *IEEE Transactions on Industrial Electronics*, vol. 56, no. 6, pp. 2023–2029, June 2009.

[25] B. Andresen and J. Birk, "A high power density converter system for the gamesa g10x 4, 5 mw wind turbine," in *2007 European Conference on Power Electronics and Applications*, 2007.

[26] G. K. Singh, A. S. Kumar, and R. P. Saini, "Steady-state modeling and analysis of six-phase self-excited induction generator for renewable energy generation," *Electric Power Components and Systems*, vol. 38, no. 2, pp. 137–151, 2009.

[27] G. Singh, A. S. Kumar, and R. Saini, "Selection of capacitance for self-excited six-phase induction generator for stand-alone renewable energy generation," *Energy*, vol. 35, no. 8, pp. 3273 – 3283, 2010.

[28] E. Fuchs and L. Rosenberg, "Analysis of an alternator with two displaced stator windings," *IEEE Transactions on Power Apparatus and Systems*, no. 6, pp. 1776–1786, 1974.

[29] Z. Wu, O. Ojo, and J. Sastry, "High-performance control of a dual stator winding dc power induction generator," *IEEE Transactions on Industry Applications*, vol. 43, no. 2, pp. 582–592, March 2007.

[30] Y. Li, Y. Hu, W. Huang, L. Liu, and Y. Zhang, "The capacity optimization for the static excitation controller of the dual-stator-winding induction generator operating in a wide

speed range," *IEEE Transactions on Industrial Electronics*, vol. 56, no. 2, pp. 530–541, Feb 2009.

[31] M. Moradian and J. Soltani, "An isolated three-phase induction generator system with dual stator winding sets under unbalanced load condition," *IEEE Transactions on Energy Conversion*, vol. 31, no. 2, pp. 531–539, June 2016.

[32] A. Cavagnino, A. Tenconi, and S. Vaschetto, "Experimental characterization of a belt-driven multiphase induction machine for 48-v automotive applications: Losses and temperatures assessments," *IEEE Transactions on Industry Applications*, vol. 52, no. 2, pp. 1321–1330, March 2016.

[33] D. Levy, "Analysis of a double-stator induction machine used for a variable-speed/constant-frequency small-scale hydro/wind electric power generator," *Electric Power Systems Research*, vol. 11, no. 3, pp. 205–223, 1986.

[34] B. Singh, S. Jain, and S. Dwivedi, "Direct torque control induction motor drive with improved flux response," *Advances in Power Electronics*, vol. 2012, 2012.

[35] P. Vas, *Sensorless vector and direct torque control*. Oxford Univ. Press, 1998.

[36] M. Abdullah, A. Yatim, C. Tan, and R. Saidur, "A review of maximum power point tracking algorithms for wind energy systems," *Renewable and sustainable energy reviews*, vol. 16, no. 5, pp. 3220–3227, 2012.

[37] M. J. Durn, S. Kouro, B. Wu, E. Levi, F. Barrero, and S. Alepuz, "Six-phase pmsg wind energy conversion system based on medium-voltage multilevel converter," in *Proceedings of the 2011 14th European Conference on Power Electronics and Applications*, Aug 2011, pp. 1–10.

[38] H. S. Che, W. P. Hew, N. A. Rahim, E. Levi, M. Jones, and M. J. Duran, "A six-phase wind energy induction generator system with series-connected dc-links," in *2012 3rd IEEE International Symposium on Power Electronics for Distributed Generation Systems (PEDG)*, June 2012, pp. 26–33.

[39] H. S. Che, E. Levi, M. Jones, M. J. Duran, W. P. Hew, and N. A. Rahim, "Operation of a six-phase induction machine using series-connected machine-side converters," *IEEE Transactions on Industrial Electronics*, vol. 61, no. 1, pp. 164–176, Jan 2014.

[40] I. Gonzalez, M. J. Duran, H. S. Che, E. Levi, and J. Aguado, "Fault-tolerant efficient control of six-phase induction generators in wind energy conversion systems with series-parallel machine-side converters," in *7th IET International Conference on Power Electronics, Ma es and Drives (PEMD 2014)*, April 2014, pp. 1–6.

[41] M. J. Duran, I. G. Prieto, M. Bermudez, F. Barrero, H. Guzman, and M. R. Arahal, "Optimal fault-tolerant control of six-phase induction motor drives with parallel converters," *IEEE Transactions on Industrial Electronics*, vol. 63, no. 1, pp. 629–640, Jan 2016.

[42] M. J. Duran and F. Barrero, "Recent advances in the design, modeling, and control of multiphase machinespart ii," *IEEE Transactions on Industrial Electronics*, vol. 63, no. 1, pp. 459–468, Jan 2016.

[43] M. Duran, F. Barrero, S. Toral, M. Arahal, R. Gregor, and R. Marfil, "Multi-phase generators viability for offshore wind farms with hvdc transmission," in *International Conference on Renewable Energies and Power Quality*, 2008.

[44] H. S. Che, W. P. Hew, N. A. Rahim, E. Levi, M. Jones, and M. J. Duran, "Current control of a six-phase induction generator for wind energy plants," in *2012 15th International Power Electronics and Motion Control Conference (EPE/PEMC)*, Sept 2012, pp. LS5b.2–1–LS5b.2–7.

[45] G. K. Singh, K. Nam, and S. K. Lim, "A simple indirect field-oriented control scheme for multiphase induction machine," *IEEE Transactions on Industrial Electronics*, vol. 52, no. 4, pp. 1177–1184, Aug 2005.

[46] C. Y. Oh, D. H. Kim, D. G. Woo, W. Y. Sung, Y. S. Kim, and B. K. Lee, "A high-efficient nonisolated single-stage on-board battery charger for electric vehicles," *IEEE Transactions on Power Electronics*, vol. 28, no. 12, pp. 5746–5757, Dec 2013.

[47] A. K. Singh and M. K. Pathak, "Single-stage zeta-sepic-based multifunctional integrated converter for plug-in electric vehicles," *IET Electrical Systems in Transportation*, 2017.

[48] M. M. Morcos, N. G. Dillman, and C. R. Mersman, "Battery chargers for electric vehicles," *IEEE Power Engineering Review*, vol. 20, no. 11, pp. 8–11, 18, Nov 2000.

[49] A. K. Singh and M. K. Pathak, "Single-phase bidirectional ac/dc converter for plug-in electric vehicles with reduced conduction losses," *IET Power Electronics*, vol. 11, no. 1, pp. 140–148, 2017.

[50] M. G. Egan, D. L. O'Sullivan, J. G. Hayes, M. J. Willers, and C. P. Henze, "Power-factor-corrected single-stage inductive charger for electric vehicle batteries," *IEEE Transactions on Industrial Electronics*, vol. 54, no. 2, pp. 1217–1226, April 2007.

[51] J. M. Slicker, "Pulse width modulation inverter with battery charger," Jan. 1 1985, uS Patent 4,491,768.

[52] S. Kinoshita, "Electric system of electric vehicle," May 13 1997, uS Patent 5,629,603.

[53] L. D. Sousa, B. Silvestre, and B. Bouchez, "A combined multiphase electric drive and fast battery charger for electric vehicles," in *2010 IEEE Vehicle Power and Propulsion Conference*, Sept 2010, pp. 1–6.

[54] I. Subotic, E. Levi, and N. Bodo, "A fast on-board integrated battery charger for evs using an asymmetrical six-phase machine," in *2014 IEEE Vehicle Power and Propulsion Conference (VPPC)*, Oct 2014, pp. 1–6.

[55] I. Subotic, N. Bodo, and E. Levi, "An ev drive-train with integrated fast charging capability," *IEEE Transactions on Power Electronics*, vol. 31, no. 2, pp. 1461–1471, Feb 2016.

[56] I. Subotic, N. Bodo, E. Levi, and M. Jones, "Onboard integrated battery charger for evs using an asymmetrical nine-phase machine," *IEEE Transactions on Industrial Electronics*, vol. 62, no. 5, pp. 3285–3295, May 2015.

[57] E. Levi, M. Jones, S. N. Vukosavic, and H. A. Toliyat, "A novel concept of a multiphase, multimotor vector controlled drive system supplied from a single voltage source inverter," *IEEE Transactions on Power Electronics*, vol. 19, no. 2, pp. 320–335, March 2004.

[58] S. Dusmez and A. Khaligh, "A compact and integrated multifunctional power electronic interface for plug-in electric vehicles," *IEEE Transactions on Power Electronics*, vol. 28, no. 12, pp. 5690–5701, Dec 2013.

[59] ——, "A charge-nonlinear-carrier-controlled reduced-part single-stage integrated power electronics interface for automotive applications," *IEEE Transactions on Vehicular Technology*, vol. 63, no. 3, pp. 1091–1103, March 2014.

[60] Y. J. Lee, A. Khaligh, and A. Emadi, "Advanced integrated bidirectional ac/dc and dc/dc converter for plug-in hybrid electric vehicles," *IEEE Transactions on Vehicular Technology*, vol. 58, no. 8, pp. 3970–3980, Oct 2009.

[61] P. Y. Kong, J. A. Aziz, M. R. Sahid, and L. W. Yao, "A bridgeless pfc converter for on-board battery charger," in *2014 IEEE Conference on Energy Conversion (CENCON)*, Oct 2014, pp. 383–388.

[62] C. Shi, H. Wang, S. Dusmez, and A. Khaligh, "A sic-based high-efficiency isolated on-board pev charger with ultrawide dc-link voltage range," *IEEE Transactions on Industry Applications*, vol. 53, no. 1, pp. 501–511, Jan 2017.

[63] P. N. Enjeti, P. D. Ziogas, J. F. Lindsay, and M. H. Rashid, "A new pwm speed control system for high-performance ac motor drives," *IEEE Transactions on Industrial Electronics*, vol. 37, no. 2, pp. 143–151, Apr 1990.

[64] A. Iqbal, E. Levi, M. Jones, and S. Vukosavic, "Generalised sinusoidal pwm with harmonic injection for multi-phase vsis," in *Power Electronics Specialists Conference, 2006. PESC '06. 37th IEEE*, June 2006, pp. 1–7.

[65] M. J. Duran, J. A. Riveros, F. Barrero, H. Guzman, and J. Prieto, "Reduction of common-mode voltage in five-phase induction motor drives using predictive control techniques," *IEEE Transactions on Industry Applications*, vol. 48, no. 6, pp. 2059–2067, Nov 2012.

[66] S. Payami, R. K. Behera, A. Iqbal, and R. Al-Ammari, "Common-mode voltage and vibration mitigation of a five-phase three-level npc inverter-fed induction motor drive system," *IEEE Journal of Emerging and Selected Topics in Power Electronics*, vol. 3, no. 2, pp. 349–361, June 2015.

[67] K. A. Chinmaya and M. U. Bhasker, "Analysis of different space vector pulse width modulation techniques for five-phase inverters," in *2014 Annual IEEE India Conference (INDICON)*, Dec 2014, pp. 1–6.

[68] O. Dordevic, M. Jones, and E. Levi, "A comparison of carrier-based and space vector pwm techniques for three-level five-phase voltage source inverters," *IEEE Transactions on Industrial Informatics*, vol. 9, no. 2, pp. 609–619, May 2013.

[69] K. Gopakumar, V. T. Ranganthan, and S. R. Bhat, "Split-phase induction motor operation from pwm voltage source inverter," *IEEE Transactions on Industry Applications*, vol. 29, no. 5, pp. 927–932, Sep 1993.

[70] Y. Zhao and T. A. Lipo, "Space vector pwm control of dual three-phase induction machine using vector space decomposition," *IEEE Transactions on Industry Applications*, vol. 31, no. 5, pp. 1100–1109, Sep 1995.

[71] A. R. Bakhshai, G. Joos, and H. Jin, "Space vector pwm control of a split-phase induction machine using the vector classification technique," in *Applied Power Electronics Conference and Exposition, 1998. APEC '98. Conference Proceedings 1998., Thirteenth Annual*, vol. 2, Feb 1998, pp. 802–808 vol.2.

[72] E. A. R. E. Ariff, O. Dordevic, and M. Jones, "A space vector pwm technique for a three-level symmetrical six-phase drive," *IEEE Transactions on Industrial Electronics*, vol. 64, no. 11, pp. 8396–8405, Nov 2017.

[73] P. Sanjeevikumar, G. Grandi, J. O. Ojo, and F. Blaabjerg, "Direct vector controlled six-phase asymmetrical induction motor with power balanced space vector pwm multilevel operation," *International Journal of Power and Energy Conversion*, vol. 7, no. 1, pp. 57–83, 2016.

[74] J. S. Hu, K. Y. Chen, T. Y. Shen, and C. H. Tang, "Analytical solutions of multi-level space-vector pwm for multiphase voltage source inverters," *IEEE Transactions on Power Electronics*, vol. 26, no. 5, pp. 1489–1502, May 2011.

[75] M. Mounir, G. Qiang, and X. Cai, "Space vector modulation for six-phase open-end winding pmsm motor drives with common mode voltage suppression," in *IECON 2017 - 43rd Annual Conference of the IEEE Industrial Electronics Society*, Oct 2017, pp. 3865–3871.

[76] J. Zheng, F. Rong, X. Liu, and S. Huang, "Common-mode voltage supression of dual y shift 30; six-phase electric machine," in *2017 IEEE International Magnetics Conference (INTERMAG)*, April 2017, pp. 1–1.

[77] . Lpez, J. lvarez, J. Malvar, A. G. Yepes, A. Vidal, F. Baneira, D. Prez-Estvez, F. D. Freijedo, and J. Doval-Gandoy, "Space-vector pwm with common-mode voltage elimination for multiphase drives," *IEEE Transactions on Power Electronics*, vol. 31, no. 12, pp. 8151–8161, Dec 2016.

[78] R. H. Nelson and P. C. Krause, "Induction machine analysis for arbitrary displacement between multiple winding sets," *IEEE Transactions on Power Apparatus and Systems*, vol. PAS-93, no. 3, pp. 841–848, May 1974.

[79] T. Lipo, "A d-q model for six phase induction machines," in *Proc. ICEM80*, 1980, pp. 860–867.

[80] Y. Zhao and T. A. Lipo, "Space vector pwm control of dual three-phase induction machine using vector space decomposition," *IEEE Transactions on Industry Applications*, vol. 31, no. 5, pp. 1100–1109, Sep 1995.

[81] V. Pant, G. K. Singh, and S. N. Singh, "Modeling of a multi-phase induction machine under fault condition," in *Proceedings of the IEEE 1999 International Conference on Power Electronics and Drive Systems. PEDS'99 (Cat. No.99TH8475)*, vol. 1, July 1999, pp. 92–97 vol.1.

[82] G. K. Singh, V. Pant, and Y. Singh, "Voltage source inverter driven multi-phase induction machine," *Computers & Electrical Engineering*, vol. 29, no. 8, pp. 813–834, 2003.

[83] J.-S. Kim and S.-K. Sul, "A novel voltage modulation technique of the space vector pwm," *IEEJ Transactions on Industry Applications*, vol. 116, no. 8, pp. 820–825, 1996.

[84] F. Blaschke, "The principle of field orientation as applied to the new transvector closed-loop system for rotating-field machines," *Siemens review*, vol. 34, no. 3, pp. 217–220, 1972.

[85] B. Wu, Y. Lang, N. Zargari, and S. Kouro, *Power conversion and control of wind energy systems*. John Wiley & Sons, 2011.

[86] R. Lanzafame and M. Messina, "Fluid dynamics wind turbine design: Critical analysis, optimization and application of bem theory," *Renewable energy*, vol. 32, no. 14, pp. 2291–2305, 2007.

[87] G. Abad, J. Lopez, M. Rodriguez, L. Marroyo, and G. Iwanski, *Doubly fed induction machine: modeling and control for wind energy generation*. John Wiley & Sons, 2011, vol. 85.

[88] K. Gopalakrishnan, S. Das, and G. Narayanan, "Analytical expression for rms dc link capacitor current in a three-level inverter," in *CENTENARY CONFERENCE*. Indian Institute of Science, December 2011, pp. 1–6.

[89] N. H. Malik and A. A. Mazi, "Capacitance requirements for isolated self excited induction generators," *IEEE Transactions on Energy Conversion*, vol. EC-2, no. 1, pp. 62–69, March 1987.

[90] I. Subotic, N. Bodo, and E. Levi, "Single-phase on-board integrated battery chargers for evs based on multiphase machines," *IEEE Transactions on Power Electronics*, vol. 31, no. 9, pp. 6511–6523, 2016.

# APPENDIX

## SYSTEM PARAMETERS

Table 1: DC/DC Converter Parameters

| **DC/DC Converter** | |
|---|---|
| Grid voltage ($V_g$) | *220 V* |
| DC-link voltage ($V_{hv}$) | *400 V* |
| Line frequency ($f_L$) | *50Hz* |
| Nominal battery voltage ($V_b$) | *300 V* |
| $L_1$/$L_2$ | *2 mH* |
| $C_{hv}$/$C_M$/$C_b$ | *550/10/2200$\mu F$* |

Table 2: Wind Turbine Parameters

| **Turbine** | |
|---|---|
| Rated power [$P_t$] | 2700 W |
| Radius of the turbine [R] | 1.4 m |
| Rated wind speed [$v_w$] | 12 m/s |
| Air density [$\rho$] | 1.225 kg/m$^2$ |

Table 3: Asymmetrical Six-phase Induction Machine Parameters

| **ASIG/ ASIM** | | |
|---|---|---|
| Parameter of the machine | Six-phase, six-pole (value per-phase) | Three-phase, six-pole (value per-phase) |
| Number of poles [P] | 6 | 6 |
| Stator resistance [$r_s$] | 4.12 Ω | 8.25 Ω |
| Rotor resistance [$r_r$] | 8.79 Ω | 8.79 Ω |
| Stator leakage inductance [$L_{ls}$] | 21.6 mH | 43.3 mH |
| Rotor leakage inductance [$L_{lr}$] | 43.3 mH | 43.3 mH |
| Mutual inductance [$L_m$] | 234.6 mH | 469.2 mH |
| Controller parameters | | |
| d-q current controllers | Kp=14 | Ki=8000 |
| Speed controller | Kp=0.5 | Ki=2.6 |
| Flux controller | Kp=60 | Ki=140 |
| DC-link voltage controller | Kp=1.0 | Ki=5.5 |